2013

Reaction of green leaf volatiles as a source of secondary organic aerosols in fog droplets

Amie Kathryn Hansel
Louisiana State University and Agricultural and Mechanical College

REACTION OF GREEN LEAF VOLATILES AS A SOURCE OF SECONDARY ORGANIC AEROSOLS IN FOG DROPLETS

A Thesis

Submitted to the Graduate Faculty of the
Louisiana State University and
Agriculture and Mechanical College
in partial fulfillment of the
requirements for the degree of
Master of Science in Chemical Engineering

in

Cain Department of Chemical Engineering

by
Amie K. Hansel
B.S., Biological Sciences, Louisiana State University, 2007
December 2013

ACKNOWLEDGMENTS

I would like to thank my advisor, Dr. K.T. Valsaraj, for his unquestionable and continual support, encouragement, and patience. Under the guidance of Dr. Valsaraj, I have learned invaluable approaches to research and learning that has expanded my abilities and made me a better researcher and engineer. I look forward to utilizing these lessons in future endeavors and appreciate the opportunity to have learned them from Dr. Valsaraj.

I would also like to thank Dr. Mike Benton and Dr. Franciso Hung for serving on my committee and providing critical insight on my thesis. Special thanks must be extended to Dr. Benton, whose encouragement lead to my application to the graduate program.

This work was funded by the National Science Foundation under Award Number AGS-1106559. Collaborative assistance was provided by Dr. Cort Anastasio and Dr. Nicole Richards-Henderson at the University of California, Davis. I appreciate their impeccable work with the project and insightful attributions to my work.

I would like to express my appreciation to Dr. Franz Ehrenhauser for the instrumental assistance with planning, method development, and critical thinking, especially in the beginning of my work. My grateful thanks are extended to my lab mate and friend, Ms. Aubrey Heath for assisting me with laboratory equipment while offering endless advice and encouragement. I am grateful to my fellow graduate students, Paria Avij and Harsha Vempati, and I sincerely thank Pratibha Sharma for her friendship and inspiration throughout my time in graduate school. Additionally, I would like to thank my undergraduate student worker, Andrew Pham, for his exceptional devotion to the lab, as well as Ms. Connie David, the research associate in LSU's Department of Chemistry Mass Spectrometry Facility, for her assistance with the use of the

HPLC-ESI/MS, and Dr. Pat Bollich for allowing us to collect fog field samples safely on the property of the LSU College of Agriculture Central Research Station.

I ultimately would like to thank the faculty of the Cain Department of Chemical Engineering for providing the teachings and coursework required to excel in the field of chemical engineering as well as the staff and machine shop for providing assistance in office relations and equipment issues.

I would also like to express my deepest gratitude for the irreplaceable love and support from my family and friends for never questioning my ability to complete the graduate program while insisting that I exceed my personal expectations and meet theirs.

TABLE OF CONTENTS

ABSTRACT

Green leaf volatiles (GLVs) are a group of biogenic volatile organic compounds (BVOCs) released into the atmosphere by vegetation when plants undergo stress or mechanical damage. BVOCs produce secondary organic aerosol (SOA) in the gas phase; however, their oxidation as a source of SOA in the liquid phase has not been investigated. Once released into the atmosphere, water-soluble GLVs partition into atmospheric water phases such as fog, mist, dew or rain, where they are oxidized by hydroxyl radicals (˙OH). Photochemical oxidation yields products that are higher in molecular weight, more polar, more oxygenated, and lower in vapor pressure. When the water droplets evaporate, the oxidation products are left behind as secondary organic aerosol. Methyl jasmonate (MeJa) and methyl salicylate, (MeSa), two GLVs typical of many plants, were reacted with hydroxyl radicals in the aqueous phase. The formed products were identified via high performance liquid chromatography paired with electrospray ionization mass spectrometry (HPLC-ESI/MS) and matched to potential reaction pathways for the oxidation of MeJa and MeSa with ˙OH. The oxidation products exhibit a higher molecular mass than the parent GLV compound due to dimerization and the addition of oxygen and hydroxyl groups. For MeJa, $C_{13}H_{20}O_4$, $C_{13}H_{20}O_5$, $C_{13}H_{22}O_5$, $C_{13}H_{22}O_6$ were found as oxidation products, whereas for MeSa, $C_8H_8O_4$, $C_8H_8O_5$, $C_{16}H_{14}O_6$ were found. The estimated vapor pressures of these products are significantly (up to 5 orders of magnitude) less than those of the associated parent compounds and therefore, remain in the atmosphere as SOA after evaporation of the water droplet. The contribution of the identified oxidation products to SOA formation is estimated based on measured HPLC-ESI/MS response and compared to actual SOA mass yield measurements. Additionally, physico-chemical properties of the GLVs were measured, which give insight into GLV activity in the aqueous phase.

CHAPTER 1
INTRODUCTION AND LITERATURE REVIEW

Introduction

The United States Environmental Protection Agency (US EPA) defines volatile organic compounds (VOCs) as organic compounds that vaporize at room temperature and are known to cause irritation, headaches, and other physical ailments [1]. VOCs play an important role in the atmospheric carbon mass balance, a mass balance that researchers have been budgeting for years [2-10]. The total global VOC flux is estimated to be around 1300 teragrams of carbon per year ($Tg{\cdot}C{\cdot}yr^{-1}$, 1 Tg = 10^{12} g) [2, 5]. The majority of atmospheric VOCs are biogenic volatile organic compounds (BVOCs), VOCs emitted by vegetation and the ocean [2, 10]. BVOCs are responsible for an estimated 1150 $Tg{\cdot}C{\cdot}yr^{-1}$, or 88%, of the total global VOC flux [2, 5]. BVOCs can be grouped into four categories: isoprenes, monoterpenes, other reactive VOC (ORVOC), and other VOC (OVOC) [3, 5]. Isoprenes account for 503 $Tg{\cdot}C{\cdot}yr^{-1}$, or 44%, and monoterpenes account for 127 $Tg{\cdot}C{\cdot}yr^{-1}$, or 11%, of the annual BVOC flux [5]. These two groups are together termed isoprenoids and have been the focus of much research due to the fact that their estimated emission rates are greater than those of the other BVOCs [3, 5, 6, 11-13]. The remaining 45% of BVOCs are an estimated 260 $Tg{\cdot}C{\cdot}yr^{-1}$ of other reactive and 260 $Tg{\cdot}C{\cdot}yr^{-1}$ of other non-reactive VOCs [5].

Green leaf volatiles (GLVs) are oxygenated hydrocarbons considered part of the ORVOC category. They are typically synthesized by plants from linolenic and linoleic acids [14, 15]. GLVs are emitted into the atmosphere when plants undergo stress or mechanical damage such as local temperature change or grass cutting [6, 12, 13, 15, 16]. Although emission rates of GLVs are lower in comparison to emission rates of the more commonly studied isoprenoids, the large

quantity of plant species that has been linked to GLV emissions increases the significance of GLVs [12, 13]. Arey et al. evaluated the emission of oxygenated hydrocarbons, including the GLVs, 3-hexen-1-ol (HxO) and 3-hexenylacetate (HxAc), and linked them to a majority of the observed agricultural and natural plant species in California's Central Valley – 22 of the 30 studied plant species were linked to HxO and 24 were linked to HxAc [12]. The high prevalence of the numerous plant species emitting GLVs increased the significance of the reported emissions. Additionally, the mean emission rate of HxAc surpassed that of the measured monoterpene emission rate for 10 of the 30 plant species studied [12]. Furthermore, HxO emission was directly linked to mechanical stress to the plants such as grass cutting, harvesting, and animal grazing that further increases the emission rates of GLVs [12, 15]. Considering atmospheric concentrations, isoprenes and monoterpenes range from parts per trillion (ppt) to parts per billion (ppb), when the atmospheric concentration of ORVOCs range from 1-3 ppb [3].

Atmospheric GLVs partition into the aqueous phase of atmospheric waters such as fog, mist, dew, or rain. The partitioning of organic molecules between the aqueous and gas phase is governed by Henry's law and determined by the vapor pressure and the water solubility of each compound. GLVs are modestly water soluble (~0.05 M) and have relatively low vapor pressures (<0.002 atm) [17]. GLVs have fairly high Henry's law constants (K_H), ranging from 3-3500 $M \cdot atm^{-1}$, indicating affinity for the aqueous phase [17]. See Table 1.1 for the physico-chemical properties and Figure 1.1 for the chemical structure of the GLVs used in this work: methyl jasmonate (MeJa), methyl salicylate (MeSa), *cis*-3-hexenyl acetate (HxAc), 2-methyl-3-butenol (MBO), *cis*-3-hexen-1-ol (HxO).

Table 1.1. Physico-chemical properties of GLVs.

GLV	Molecular Formula	CAS Number	Molecular Weight M_A (g/mol)	Boiling Point T_{bp} (°C)	Density ρ_A (25°C) (g/mL)	Henry's Law Constant K_H (M/atm) [17]	Estimated Vapor Pressure (SIMPOL) (atm) [18]
MeJA	$C_{13}H_{20}O_3$	39924-52-2	224.3	110	1.03	3538 ± 151	1.16×10^{-6}
MeSA	$C_8H_8O_3$	119-36-8	152.15	222	1.174	37.9 ± 1.7	2.96×10^{-6}
MBO	$C_5H_{10}O$	115-18-4	86.13	98-99	0.824	62.3 ± 3.5	2.63×10^{-3}
HxO	$C_6H_{12}O$	928-96-1	100.16	156-157	0.848	159 ± 15	9.88×10^{-4}
HxAc	$C_8H_{14}O_2$	3681-71-8	142.19	75-76	0.897	3.6 ± 0.22	1.40×10^{-3}

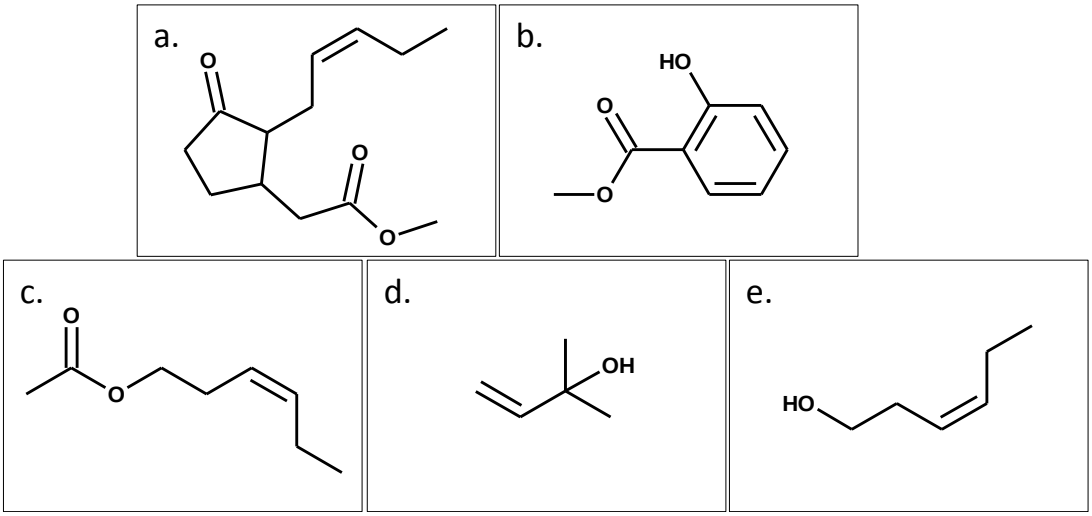

Figure 1.1. Chemical structures of green leaf volatiles: a. MeJa, b. MeSa, c. HxAc, d. MBO, e. HxO.

Fog Water

Atmospheric waters are particularly interesting in that they provide the air-water interface that is required for the uptake of atmospheric GLVs into the aqueous phase. Once absorbed, the compounds participate in aqueous phase reactions with other dissolved compounds or water molecules [19-21]. Fog droplets have been linked to aqueous phase SOA formation from organic compounds such as aldehydes and alcohols by confirming the propensity of these organics to partition from the gas phase to the aqueous phase of a fog particle and confirming that they

undergo aqueous-phase oxidation reactions with oxidants readily present in fog water, forming products with lower vapor pressures, thus contributing to SOA [19].

The liquid water content (LWC) of fog water previously collected in Baton Rouge, LA, USA, was approximately 84 mg-aq·m^{-3}-air [22], which is described as the measure of the mass of water in fog in a volume of dry air. Fog droplet sizes range from 1-10 microns, providing an estimated surface area of 8×10^{-4}·m^2·m^{-3}, and a surface tension of 72 mN·m^{-1} [20, 23]. The surface of fog droplets is interesting due to the role the surface plays in the droplet size and growth, the uptake of gases and oxidants, and the reactions that occur at the air-water interface.

Surface tension is a result of pressure on a molecular level [23]. Less water molecules are present at the surface than in the bulk resulting in less net pressure at the surface. As a result, fewer water molecules act upon the surface, thus leaving more energy in the surface molecules. Work is required to bring a bulk molecule to the surface, which creates surface tension. Typically, water has a high surface tension. The surface tension of fog water is less than the surface tension of pure water, which suggests the tendency of organic molecules to partition at the surface [24]. Surface active compounds have been identified in fog water, supporting a decrease in surface tension [22]. Molecular dynamics simulations have indicated that two of the GLVs in this study, MeSa and MBO, have a tendency to remain at the air-water interface rather than in the bulk water, suggesting that reactions are more likely to occur at the air-water interface rather than the bulk phase [25, 26], while supporting that these molecules should decrease the surface tension of water by remaining at the surface.

Fog water has also been linked to enhanced reaction rates by comparing the air-water interface of fog droplets to thin films of water, in which observed product formation rates surpassed those in bulk water reactions [27]. Enhanced reaction rates may also be connected to

fog water due to the presence of oxidants. Aqueous phase oxidation occurs via sunlight-induced anthropogenic oxidants found in atmospheric waters: hydroxyl radicals, ozone, nitrate radicals, and chlorine [10, 20, 28]. Hydroxyl radicals (˙OH) are the main oxidant in the lower atmosphere [29] and is the oxidant investigated in this work. The photolysis of hydrogen peroxide in atmospheric waters is a known source of ˙OH [21, 28, 30, 31]. Hydrogen peroxide is found naturally in atmospheric waters in concentrations ranging from 0.3-3 μM [21]. When exposed to UV light, photolysis of hydrogen peroxide produces hydroxyl radicals as shown below [32-34].

Initiation:

$$H_2O_2 + h\nu \rightarrow 2\ {}^{\cdot}OH \quad (1.1)$$

Propagation:

$$H_2O_2 + {}^{\cdot}OH \rightarrow H_2O + HO_2{}^{\cdot} \quad (1.2)$$

$$H_2O_2 + HO_2{}^{\cdot} \rightarrow {}^{\cdot}OH + H_2O + O_2 \quad (1.3)$$

Termination:

$$HO_2{}^{\cdot} + HO_2{}^{\cdot} \rightarrow H_2O_2 + O_2 \quad (1.4)$$

$$H + H_2O_2 \rightarrow {}^{\cdot}OH + H_2O \quad (1.5)$$

Secondary Organic Aerosols

Atmospheric aerosols are small solids or liquid particles suspended in the atmosphere. Primary aerosols are released directly into the atmosphere, either naturally, through sea spray or volcanic activity, or anthropogenically, from transportation or industrial processes [4]. Secondary organic aerosols are formed in the atmosphere from volatile organic compounds [15, 35]. The increase in SOA in the atmosphere can be hazardous to human health and are also known to negatively affect visibility and the earth's climate and solar radiation effects [4, 35].

Atmospheric transformation of VOCs to SOA due to exposure to sunlight and atmospheric oxidants has been confirmed [7], and SOA has been shown to form in the atmosphere from gas phase oxidation of GLVs [15, 35]; however, the aqueous phase oxidation of GLVs to form secondary organic aerosol has not been investigated.

Research Objective

The goal of this work is to confirm the oxidation of GLVs and the formation of products contributing to SOA in fog waters. Initial experiments are performed in LCMS-grade water solutions of GLVs in the bulk phase, both with and without hydrogen peroxide as an oxidant source. Aqueous phase oxidation of GLVs occurs, forming oxidation products that contain more oxygen, leaving them with the following characteristics: higher molecular weight, increased polarity, and lower vapor pressure [36]. These characteristics increase the likeliness that GLV oxidation products will remain in the atmosphere as liquid or solid particles after evaporation of the water droplet, thus forming SOA. Figure 1.2 is a schematic representation of this process showing the HLC-controlled partition of gas phase GLVs into fog water, where they encounter oxidants such as ˙OH and UV light which induces photo-oxidation reactions, forming low volatility oxidation products which remain in the atmosphere as SOA.

The presented work involves reactor design and method development, bulk phase investigation of GLV photo-oxidation, bulk phase reactions of two GLVs in the presence of the oxidant ˙OH, mechanistic development and product identification of two GLVs, and fog water collection.

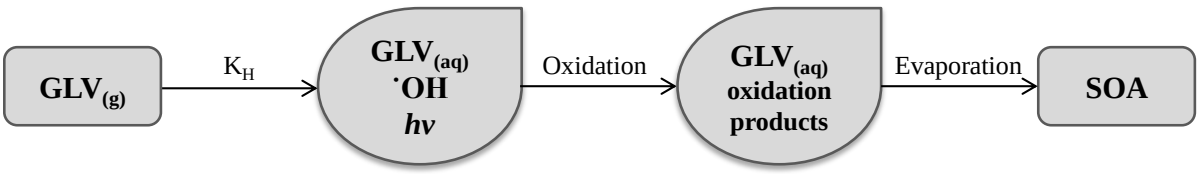

Figure 1.2 A schematic representation of GLV transformation into SOA.

CHAPTER 2
MATERIALS AND METHODS

Fog Water Collection

Authentic fog water was collected during the Fall and Winter of 2012/2013 in Baton Rouge, Louisiana, using a large stainless steel Caltech Active Strand Cloudwater Collector (ss-CASCC) [37] as shown in Figure 2.1. The ss-CASCC was held 6 feet in the air supported by an aluminum tripod hunting stand (Millennium T-100, Hunting Solutions Inc., Pearl, MS, USA) and was placed in an open field provided by the LSU College of Agriculture Central Research Station. The fog sampling site provided a good representation of weather-induced fog events in Baton Rouge, LA, and was chosen based on proximity to LSU, availability of open land, and guaranteed safety of equipment and personnel. Approximately 3 L of fog water was collected from October 2012 through February 2013 (see Table A1 in the Appendix). Fog water from each event was combined in aliquots in PFA bottles (ranging in sizes 30 mL, 60 mL, 100 mL, 250 mL, and 500 mL), flash frozen in liquid nitrogen, and stored in a freezer at -20°C. After fog season, a portion of the samples were shipped to the co-contributing group at UCD as part of the collaborative research. Some fog samples have been used in surface tension measurements (presented later in this work), and authentic fog water is to be used in future research: characterizing the formation of photo-oxidants in fog water ($^{\cdot}OH$, $^{1}O_2^{*}$, $^{3}C^{*}$), quantifying the kinetics of photo-oxidation of GLVs in fog water, identifying GLV oxidation products in fog water, and measuring SOA mass yield in authentic fog water.

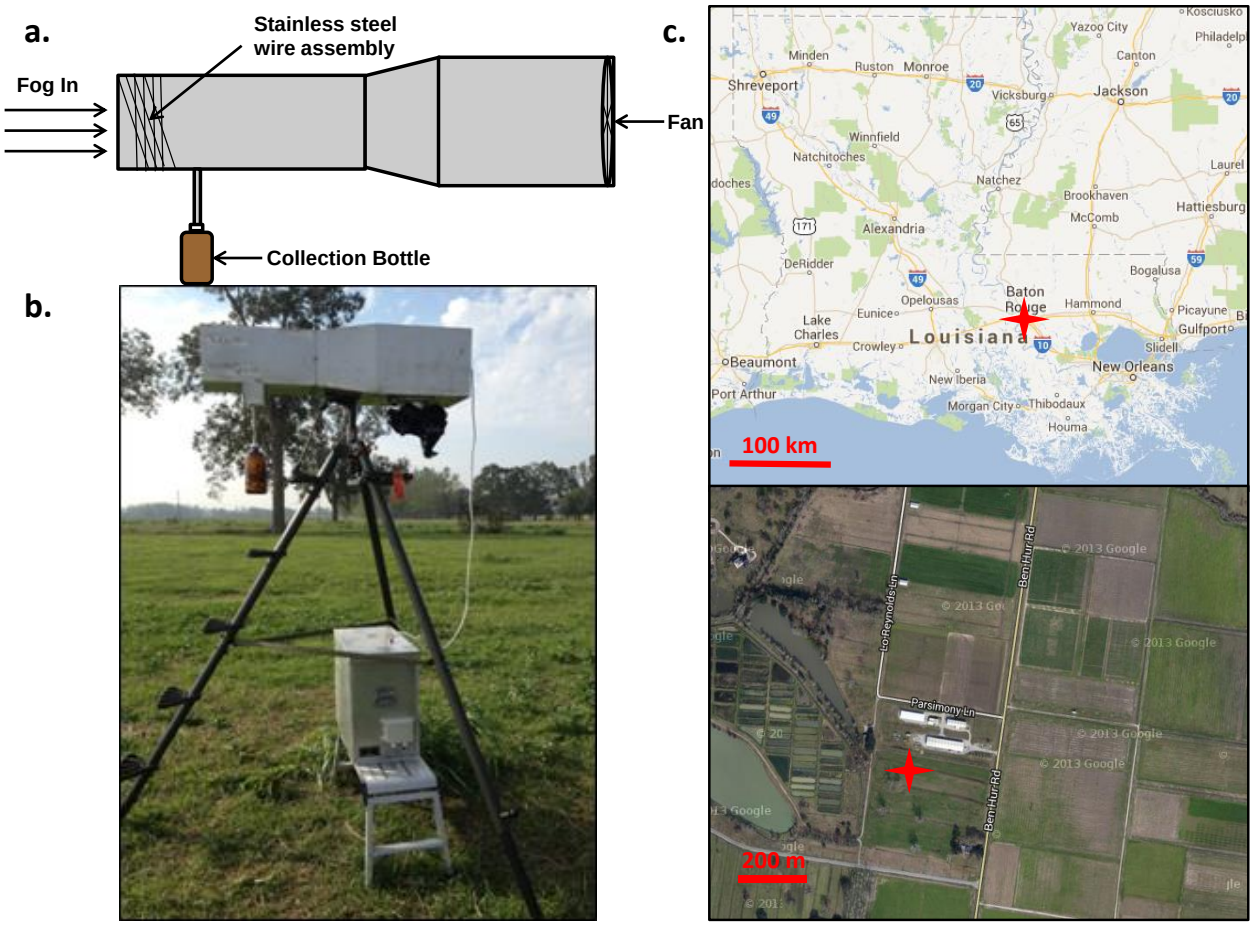

Figure 2.1. Fog collector schematic (a), photograph in field (b), and site location (c) (marked by the red cross) [38]

GLV Solution Preparation

Individual aqueous GLV solutions were prepared using commercially-available liquid green leaf volatiles and LCMS-grade water (Burdick and Jackson LC-MS grade, Honeywell, Muskegan, MI, USA). The GLVs were purchased from Sigma-Aldrich (Milwaukee, WI, USA) and used as received without further purification: methyl jasmonate (MeJa) (95%), methyl salicylate (MeSa) (≥99%), *cis*-3-hexenyl acetate (HxAc) (natural), 2-methyl-3-butenol (MBO) (≥98%), *cis*-3-hexen-1-ol (HxO) (>98%).

GLV Identification

GLV concentrations were determined via HPLC analysis using an Agilent 1100 HPLC-UV/DAD system, an Ultra II^{TM} Aqueous C18 column (Restek Corp., Bellefonte, PA, USA), and an exploratory-style water/acetonitrile gradient method, which is explained in detail in the Appendix section A2.

GLV Product Identification

HPLC-ESI/MS was used to identify the products using an Agilent 1200 HPLC-UV/DAD system consisting of the following components: degasser (G1379B), autosampler (G1367C), binary pump (G1312B), thermostated column compartment (G1316B), and diode array detector (G1315C). The ESI/MS instrument was an Agilent ESI-TOF 6210 (electrospray ionization time-of-flight mass spectrometer) (G1969A). The same HPLC gradient method (solvents each with 0.1% formic acid) and C18 column was used for HPLC analysis. 10 μL of sample was injected onto the column held at 25°C with a 0.2 $mL \cdot min^{-1}$ solvent flow rate, while the UV/DAD measured UV absorbance from 190 to 200 nm every 2 s with a 4 nm slit width. The nitrogen drying gas was kept at 325°C with a 5 $L \cdot min^{-1}$ delivery flow rate and 20 psig nebulizer pressure. Samples were analyzed in positive ion mode with a 175 V fragmentor voltage and a 4200 V capillary voltage. A total ion chromatogram (TIC) for ions with a mass-to-charge ratio (*m/z*) of 110 to 3000 was recorded over each 95-minute run. Extracted ion chromatograms (EICs) for specified *m/z* ranges based on the molecular weight of the compounds of interest were created. The ion *m/z* ranges extracted for the analysis of MeSa oxidation products were 152-155, 168-172, 185-189, and 302-305. MeJa analysis required EICs for the *m/z* ranges 225-228, 241-245, 257-260, 259-262, and 275-278. Both UV absorbance chromatograms and ion chromatograms were used to quantify parent GLV compounds and identify their oxidation products.

CHAPTER 3
PHYSICO-CHEMICAL PROPERTIES EXPERIMENTS

Octanol-Water Partition Coefficient Experiments

Octanol-water partition coefficient (K_{OW}) values were determined via experiments based on the Organisation for Economic Co-operation and Development (OECD) guideline #107 shaker-flask method. [39]. Individual solutions were made using GLVs, LCMS-grade water, and 1-octanol (analytical grade; Sigma-Aldrich, Milwaukee, WI, USA; see A3 for chemical structure) used without further purification. The experimental procedure is explained in detail in the Appendix section A4. K_{OW} values are reported in logarithmic units and are calculated as the ratio of GLV concentration in the 1-octanol phase versus the water phase, as shown in Equation 3.1.

$$K_{OW} = \frac{[GLV]_{octanol}}{[GLV]_{water}} \tag{3.1}$$

Square brackets denote molar concentrations. Octanol refers to water-saturated 1-octanol phase, and water refers to 1-octanol-saturated water phase. Measured K_{OW} values are displayed in Table 3.1 along with estimated values based on a group contribution method found in literature. K_{OW} can typically be viewed as a measure of the hydrophobicity of a compound, providing the tendency of a compound to partition between the aqueous phase and the octanol phase [23]. These experimental values served as the parameters to confirm accurate molecular-mechanical modeling simulations for Dr. Francisco Hung (at LSU), who was analyzing the interaction of GLVs at the air-water interface with molecular modeling. Simulations for MeSa and MBO using these K_{OW} values have been reported [25, 26].

Table 3.1. Measured and estimated log K_{OW} values.

GLV	Measured log K_{OW}	Group Method Estimated log K_{OW} [40]
MeJa	2.55 ± 0.027	2.58
MeSa	2.36 ± 0.028 [25]	1.60
MBO	0.69 ± 0.013 [26]	1.22
HxO	1.47 ± 0.007	1.81
HxAc	2.48 ± 0.017	2.42

Surface Tension Experiments

Solutions of each GLV in varying concentrations (aqueous solubility being a limiting factor) were prepared for surface tension measurement in a Kruess K14 Tensiometer (Kruess GmbH, Hamburg, Germany). 45 mL of each solution was placed in a 7 cm Petri dish held at 25°C, and sample concentrations were determined via HPLC analysis. Table 3.2 displays the HPLC-determined GLV concentration in each solution, the measured surface tension, and the calculated surface concentration. Figure 3.1 shows the measured surface tension of each GLV at each bulk aqueous concentration. From surface tension and aqueous concentration, a surface concentration can be calculated based on Gibbs adsorption equation shown in Equation 3.2 [23].

$$\Gamma_{GLV(W)} = -\frac{d\sigma}{d\mu_{GLV}} = -\frac{1}{RT}\frac{d\sigma}{d\ ln(C_w)} \tag{3.2}$$

$\Gamma_{GLV(W)}$ is the surface concentration of GLV in water (mol·m^{-2}) . σ is the measured surface tension (mN·m^{-1}). μ_{GLV} is the chemical potential of the GLV, and $\mu_{GLV} = RTln(C_w)$ for dilute aqueous solutions. R is the universal gas constant (8.314 J·mol^{-1}·K^{-1} in this case), and T is the temperature (298 K). C_w is the unitless concentration of GLV in water, calculated using Equation 3.3 [23].

$$C_w = C_b \times MW \times \rho_w^{-1} \tag{3.3}$$

C_b is the measured bulk GLV concentration. MW is the molecular weight of each GLV. ρ_w is the density of water. To attain surface concentration values, a plot of σ versus $ln(C_w)$ provides a line from which the slope corresponds to the surface concentration values of GLV at each bulk concentration (see Appendix section A5).

The surface concentration of each GLV can help determine how likely the GLV is to participate in oxidation reactions at the air-water interface of fog droplets. Surface tension decreases as bulk GLV concentration increases. Generally surface concentration increases as bulk concentration increases.

Additional surface tension measurements were evaluated for authentic fog water and the following reaction samples: MeJa (2mM) before reaction, MeJa with H_2O_2 (2mM) after 8-hour illumination, MeSa (1mM) before reaction, and MeSa (1mM) with H_2O_2 (10mM) after 8-hour illumination. Fog water exhibited a lower surface tension (69.1 ± 0.105 $mN{\cdot}m^{-1}$) than LCMS-grade water (70.5 ± 0.215 $mN{\cdot}m^{-1}$) due to the presence of organics, inorganics, and other contaminants in fog water. Both MeSa and MeJa exhibited an increase in surface tension when comparing initial samples to reaction samples. The surface tension of MeJa before reaction measured to be 51.7 ± 0.063 $mN{\cdot}m^{-1}$ and after reaction was 52.3 ± 0.081 $mN{\cdot}m^{-1}$. MeSa measured 69.5 ± 0.049 $mN{\cdot}m^{-1}$ before reaction and 71.2 ± 0.035 $mN{\cdot}m^{-1}$ after reaction. This increase in surface tension is due to the formation of more polar products, which increases aqueous solubility, thus increasing the tendency of the compounds to leave the air/water interface and enter into the bulk phase. These values are in agreement with the GLV surface tension results, which show higher surface tension values for smaller GLV concentrations.

Table 3.2. Measured GLV bulk concentration, surface tension, and calculated surface concentration values.

GLV	Measured Concentration (mM)	Surface Tension ($mN \cdot m^{-1}$)	Surface Concentration $\times 10^7$ ($mol \cdot m^{-2}$)
HxAc	0.0	70.2 ± 0.26	0.0
	0.6	66.8 ± 0.16	1.48
	1.5	62.3 ± 0.24	21.5
	1.9	58.7 ± 0.39	69.4
MBO	0.0	70.8 ± 0.30	0.0
	1.0	70.6 ± 0.19	0.0607
	3.0	69.7 ± 0.11	3.37
	5.2	69.5 ± 0.11	1.23
	8.8	67.7 ± 0.10	14.2
HxO	0.0	71.5 ± 0.13	0.0
	1.0	69.5 ± 0.14	0.855
	3.0	65.2 ± 0.60	15.2
	5.0	63.5 ± 0.18	14.0
	6.0	61.5 ± 0.14	48.2
	11.6	59.1 ± 0.19	14.4
MeJa	0.0	71.3 ± 0.22	0.0
	0.9	57.7 ± 0.07	6.41
	1.7	53.6 ± 0.12	23.8
	2.6	50.4 ± 0.09	33.2
MeSa	0.0	71.0 ± 0.24	0.0
	1.0	70.8 ± 0.14	0.0852
	2.1	70.1 ± 0.14	4.06
	3.1	68.9 ± 0.18	13.3
	5.3	65.2 ± 0.42	28.6

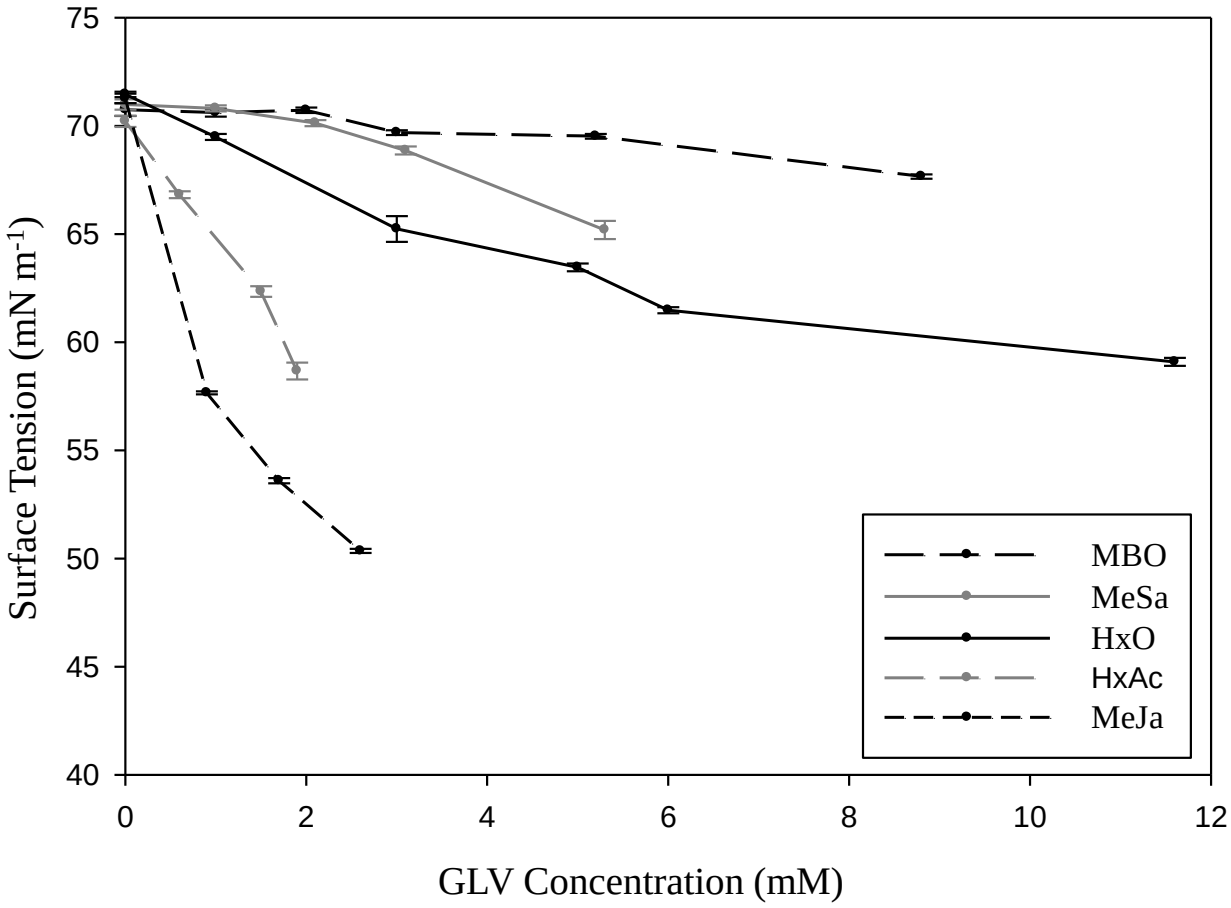

Figure 3.1. Measured GLV surface tension versus measured bulk aqueous-phase concentration.

CHAPTER 4
OXIDATION EXPERIMENTS

Reactor and Experimental Design

25 mL of each GLV solution was held in a 4.5 cm-diameter Petri Dish placed inside a polytetrafluoroethylene (PTFE) modular reactor constructed for oxidation experiments shown in Figure 4.1. Each PTFE block is square with a 6.35 cm square opening. A 7.62 cm-diameter UV-transparent quartz glass disc (Technical Glass Products, Gonzales, LA, USA) was used to seal the vessel and ensure a batch reaction. Screws at each corner ensure the tight fit and seal of the reactor. A 500-Watt ozone-free short-arc Xenon lamp (Osram Sylvania, Danvers, MA) providing polychromatic light from 220-2200 nm was used with adequate filters. The lamp was housed in an LH 151N/1 lamphousing and used an LPS 1220 lamp power supply (serial number 94180047, Spectral Energy Corp., Chester, NY, USA). An aluminum heat exchanger served as the base of the reactor and kept the reaction samples at a constant temperature of 25°C using a Polystat® temperature controller (Cole Parmer Vernon Hills, IL, USA) and magnetic stirrer (Cole Parmer, Vernon Hills, IL, USA). The heat exchanger was covered with PFA foil to ensure interness. Each sample was exposed to UV light for 8 hours. A fluorinated ethylene propylene (FEP) sampling tube was inserted into the solution to allow withdrawal of 400 µL of sample using a syringe every hour. 200 µL was used for HPLC-ESI/MS analysis, and 200 µL was used to measure pH using a PHR-146B Micro combination pH electrode (Lazar Research Laboratories, Inc., Los Angeles, CA, USA) and a pH meter (Oakton Acorn Series pH 6, Oakton Instruments, Vernon Hills, IL USA).

UV Filters

The American Society for Testing Materials (ASTM) terrestrial reference spectra for photovoltaic performance evaluation was used as reference in determining appropriate air mass

filters for photo-oxidation experiments [41] (shown in Appendix section A6). AM1.5 air mass filters (Solar Light Company, Glenside, PA) provided UV wavelengths representing light reaching Earth's surface at sea level when the sun is at a zenith angle of 48.2°. To represent the UV light that reaches the earth's surface at sea level with the sun directly overhead, an AM1.0 filter (Sciencetech, Inc., London, ON, Canada) combined with a 295 nm long pass filter (LPF) (Edmund Optics Inc., Barrington, NJ) was used. The LPF was used to ensure no light below the UVB range (< 280 nm) was allowed to pass. The AM1.0 filter set allows a higher intensity of light and a slightly lower range of wavelength of light through. Figure 4.2 displays the wavelengths of light provided by each filter combination used along with the quartz glass disc – the quartz glass disc is UV-transparent, designed to allow full transmission of light. Filter transmission data was measured using a Jasco V-570 UV-vis spectrophotometer scanning wavelengths from 190 – 700 nm (Jasco Corp., Easton, MD, USA).

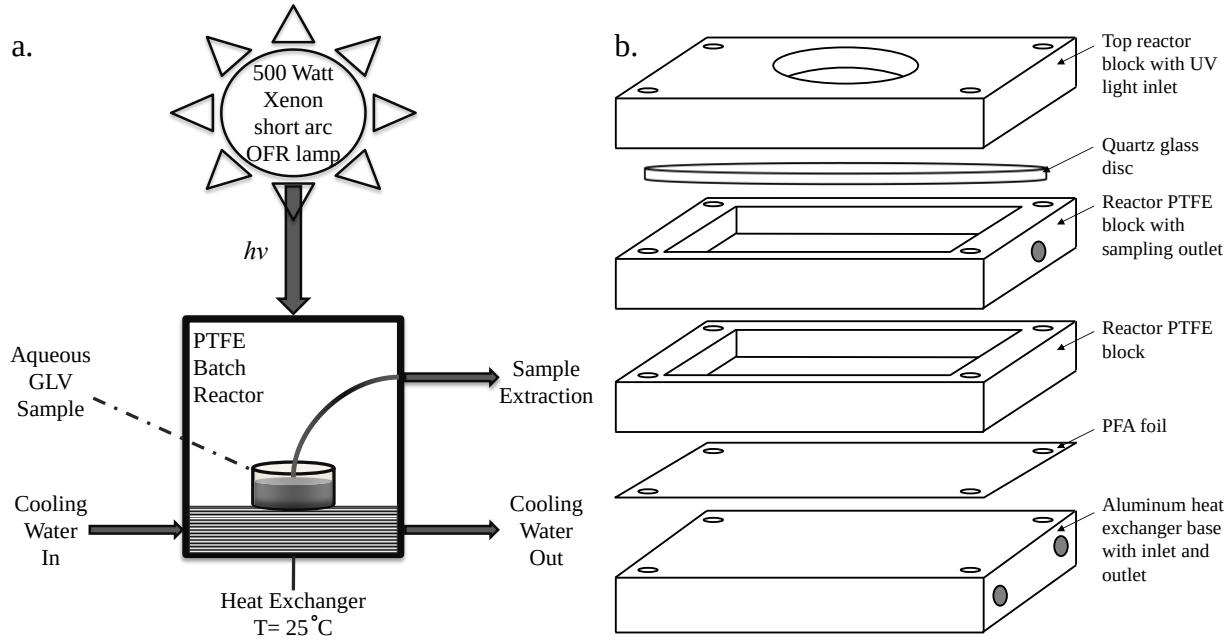

Figure 4.1. a. Photoreactor schematic b. PTFE reactor schematic

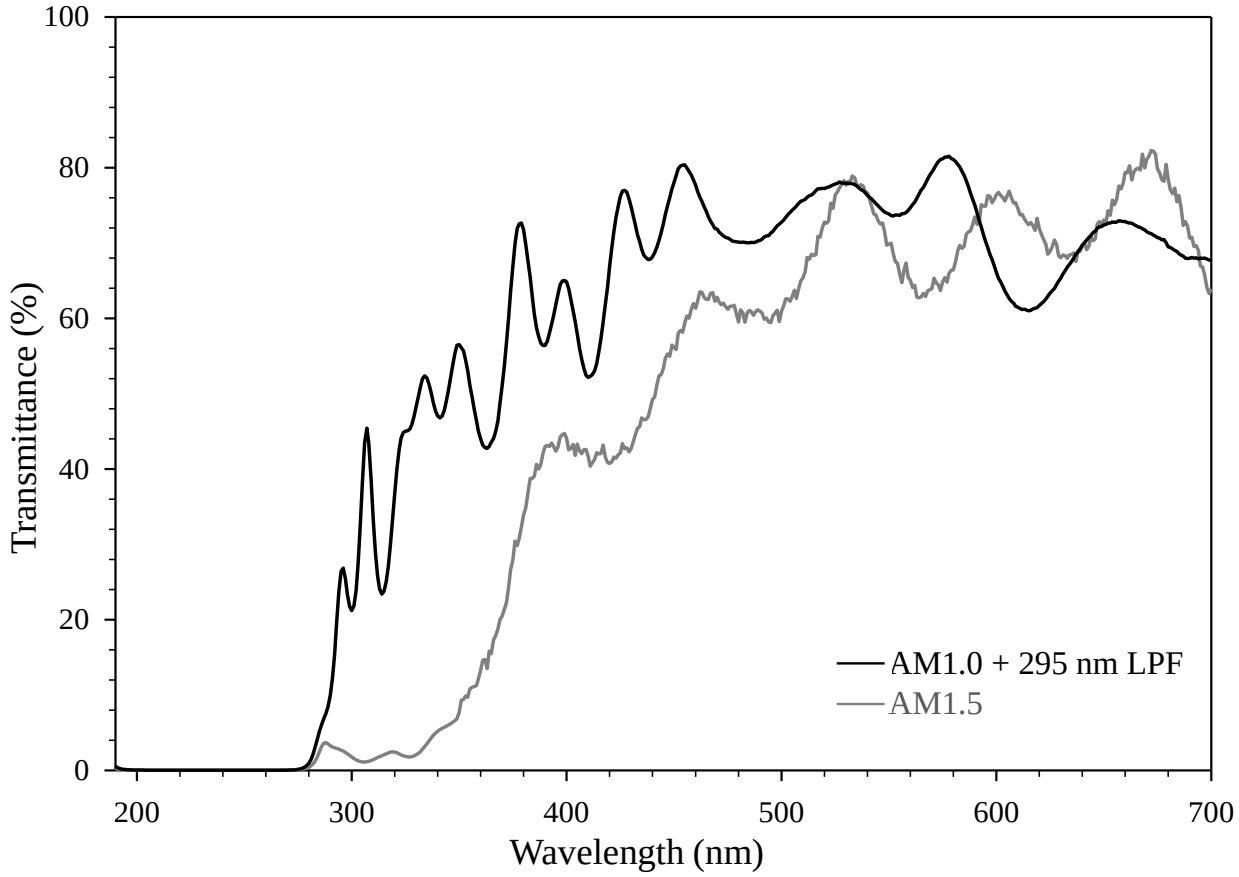

Figure 4.2. Transmission spectra for filter combinations: AM1.5 and AM1.0 + 295 nm long pass filter (both with quartz glass).

·OH Experiments

1% (w/w) hydrogen peroxide (H_2O_2) solution was prepared using LCMS-grade water and 30% (w/w) hydrogen peroxide (EMD Chemicals, Inc., Gibbstown, NJ, USA). The 1% H_2O_2 solution concentration was confirmed using an iodometric titration with 10% potassium iodide (Mallinckrodt Chemical Works, St. Louis, MO, USA), potassium iodate (Mallinckrodt Chemical Works, New York, USA), sodium thiosulfate solution (EMD Chemicals, Inc., Gibbstown, NJ, USA), a starch solution (Acros Organics, NJ, USA) as an indicator, and an acid mixture consisting of ammonium molybdate (Acros Organics, NJ, USA), DI water, and sulfuric acid (BDH, Radnor, PA, USA). To observe GLV reactions in the presence of an oxidant, 1% (w/w)

hydrogen peroxide solution was introduced to each sample as a source of hydroxyl radicals. Dark reactions were performed with each GLV and 1% H_2O_2 solution using the same reactor and experimental design. In the dark experiments, the lamp remained on; however, Petri dishes were covered with aluminum foil to prevent UV exposure.

Rate Determination

The measured rate of GLV loss is the change in green leaf volatile concentrations with respect to time, which is equal to the sum of the rates of reaction due to the oxidant, as well as direct photolysis and other pathways, shown in Equation 4.1.

$$-\frac{d[GLV]}{dt} = k_{\cdot OH+GLV}[\cdot OH][GLV] + j_{GLV}[GLV] + other[GLV] \quad (4.1)$$

Square brackets denote molar concentrations. $k_{\cdot OH+GLV}$ is the apparent second-order rate constant for the reaction of GLV with oxidant ˙OH. j_{GLV} is the rate constant for direct photolysis of the GLV. Given that ˙OH is in steady state over the course of the experiments [31, 34, 42], the GLV loss is considered pseudo-first order, and the rate constants may be combined as shown in Equation 4.2. Integrating and rearranging will yield Equation 4.3, which allows determination of a pseudo-first order degradation rate constant of each GLV by fitting a linear trend of known GLV concentrations and reaction times based on the method of least squares. $[GLV]_t$ refers to the GLV concentration at time, t, and $[GLV]_0$ represents initial GLV concentration.

$$k'_{GLV} = k_{\cdot OH+GLV}[\cdot OH] + j_{GLV} + other \quad (4.2)$$

$$\ln\frac{[GLV]_t}{[GLV]_0} = -k'_{GLV} \times t \quad (4.3)$$

SOA Yield

Richards-Henderson et al. reported an aqueous phase SOA mass yield value for oxidation of each GLV with ˙OH by measuring the mass yield (Y_{SOA}) as the mass of SOA formed per mass of GLV reacted [17]. As displayed in Equation 4.4, the SOA formed is defined as the mass of illuminated sample subtracted by the mass of the dark sample [17].

$$Y_{SOA} = \frac{SOA\ formed}{GLV\ reacted} = \frac{mass\ SOA\ illuminated - mass\ SOA\ dark}{mass\ GLV\ reacted} \times 100\% \quad (4.4)$$

Quantifying the yield of identified oxidation products leading to SOA formation involves a similar calculation. Once the products are identified and confirmed in the GLV oxidation mechanism, a product yield can be estimated using Equation 4.5.

$$Y_{product} = \frac{\sum illuminated\ \ peak\ area - \sum dark\ peak\ area}{GLV\ area_{t=0} - GLV\ area_{t=8}} \times 100\% \quad (4.5)$$

For each product, the peak area is integrated in the EIC using the MassHunter® software. The sum of all product peak areas is calculated for the dark and for the illuminated ˙OH-oxidation experiments, and then the difference of the sums from the illuminated and dark experiments is taken using analysis of the final sample (8 hour reaction time). The amount of GLV reacted is established by taking the difference in parent GLV compound peak area between the initial and the final samples. As shown in Equation 4.5, these peak area differences are divided by each other and multiplied by 100 to form a percent product yield, thus determining the percentage of GLV reacted to form products which can be predicted in the oxidation mechanism and identified via HPLC-ESI/MS analysis. This product yield estimation establishes a connection between the identified products and the measured SOA mass yield [17].

GLV Contribution to SOA

In order to determine the significance of aqueous phase SOA formation from GLVs, the following equations are considered. Defined in Equation 4.6 $[GLV]_{gas}$ is the gas phase GLV concentration estimated to be between 1-3 ppb [3]. K_H is the Henry's law constant value for each GLV (ranging from 3-3500 M·atm^{-1}) [17]. $[GLV]_{aq}$ is the aqueous phase GLV concentration which can be calculated based on each GLV HLC value and the estimated GLV gas phase concentration. According to Equation 4.7, $[SOA]_{aq}$ is the concentration of aqueous phase SOA, calculated using the steady state concentration of ·OH ($[^{\cdot}OH]_{ss}$), the second order rate constants ($k_{GLV+^{\cdot}OH}$) – which were determined by UCD – and the SOA mass yield (Y_{aq}), which is reported by Richards-Henderson et al [17]. Finally, as in Equation 4.8, the rate of SOA formation, R_{SOA}, can be estimated based on the aqueous phase SOA concentration and the liquid water content of fog water, estimated to be around 84 mg-aq·m^{-3}-air in Baton Rouge, LA, USA, fog water [22] .

$$[GLV]_{aq} = K_H \times [GLV]_{gas} \quad (4.6)$$

$$[SOA]_{aq} = k_{GLV+^{\cdot}OH} \times [^{\cdot}OH]_{ss} \times [GLV]_{aq} \times Y_{aq} \quad (4.7)$$

$$R_{SOA} = \frac{[SOA]aq}{LWC} \quad (4.8)$$

CHAPTER 5
RESULTS AND DISCUSSION

GLV Photo-oxidation

Of the five GLVs examined, MeSa is the only GLV shown to decrease in concentration when exposed to UV light alone without the presence of an oxidant (Figure 5.1). The absorption spectra of the GLVs are displayed in Figure 5.2. Due to its phenolic aromaticity, MeSa is the only GLV to absorb light within the range of UV light provided by the AM1.5-filtered light (~280 – 330 nm). Although MeSa degrades more than other GLVs, it is not a significant decrease in concentration. Photo-degradation was not observed, and no products were detected. No photo-oxidation occurs during GLV exposure to UV light without the presence of an oxidant.

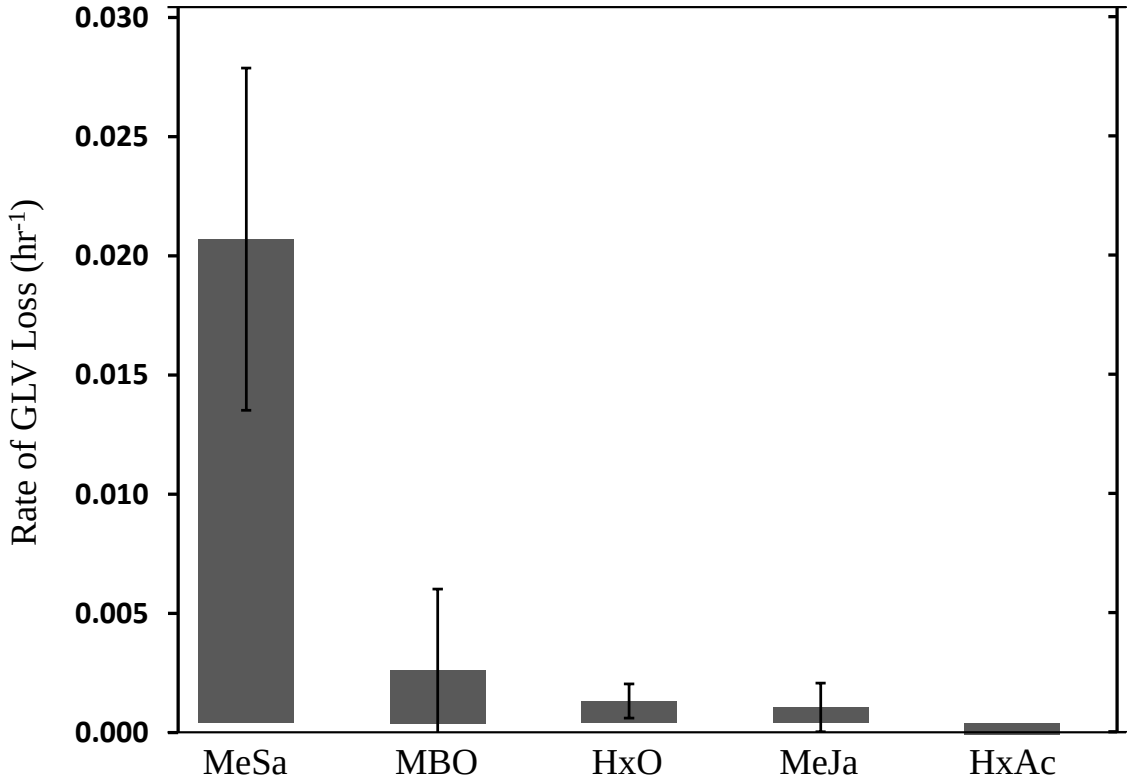

Figure 5.1. The rate of degradation for each GLV shows that MeSa is the only GLV to show slight GLV loss over an 8-hour exposure to AM1.5-filtered UV light.

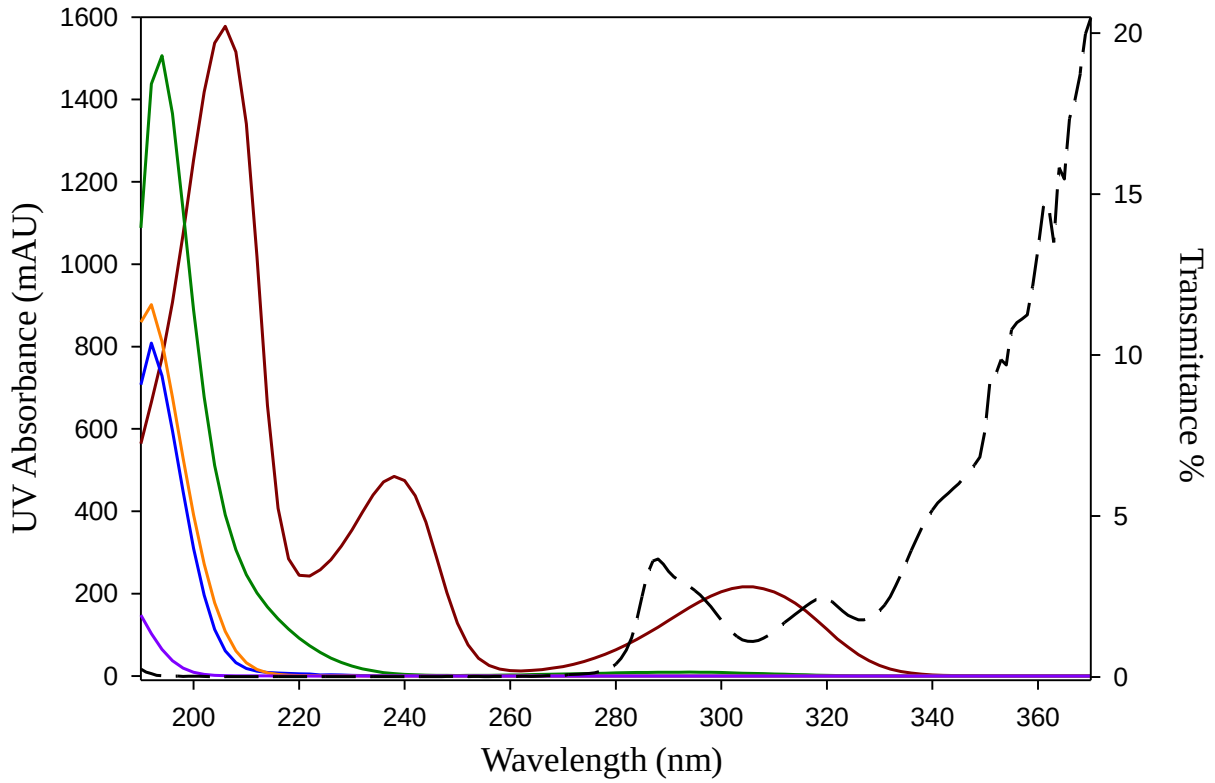

Figure 5.2. UV absorption spectra of the 5 GLVs overlaid with the AM1.5 percent transmittance (dotted black line). MeSa (red), MeJa (green), HxO (orange), HxAc (blue), MBO (purple). MeSa is the only GLV whose UV absorbance overlaps with the wavelength of light transmitted by the AM1.5 filter set.

GLV Oxidation with ˙OH

Product Formation and Identification

Figures 5.3 and 5.6 show the suspected reaction pathways and products formed during the reaction of MeJa and MeSa with ˙OH. For simplicity, we focus here on typical potential reaction pathways that lead to products that are consistent with the HPLC-ESI/MS results discussed below. We emphasize that this scheme is intended to be illustrative in its treatment of the chemistry and not comprehensive, as such other products than those shown in Figures 5.3 and 5.6 may contribute to the observed peaks in the mass spectra.

In Figure 5.3, the oxidation of MeJa (1) proceeds through the addition of ˙OH to the double bond [43-45] forming two β-hydroxyalkyl radical isomers (2 and 3), which in the

presence of $HO_2^{\cdot}$ and O_2 can lead to the formation of hydroperoxides (7 and 8) and β-hydroxyperoxy radicals (5 and 6), respectively. Both the hydroperoxides and hydroxyperoxy radicals can decompose or tautomerize leading to products (11-14 and 17-18). Alternative pathways for the formation of products is the reaction of β-hydroxyalkyl radicals (2 and 3) with $^{\cdot}OH$ forming diols (4), which can decompose (11 and 12) and tautomerize to form ketones (17 and 18), as well as isomerization of the β-hydroxyalkyl radicals (9 and 10), which then may decompose to diols (15 and 16) and ketones (17 and 18). Radical reactions may continue to occur in the aqueous phase as long as radicals are present in the system.

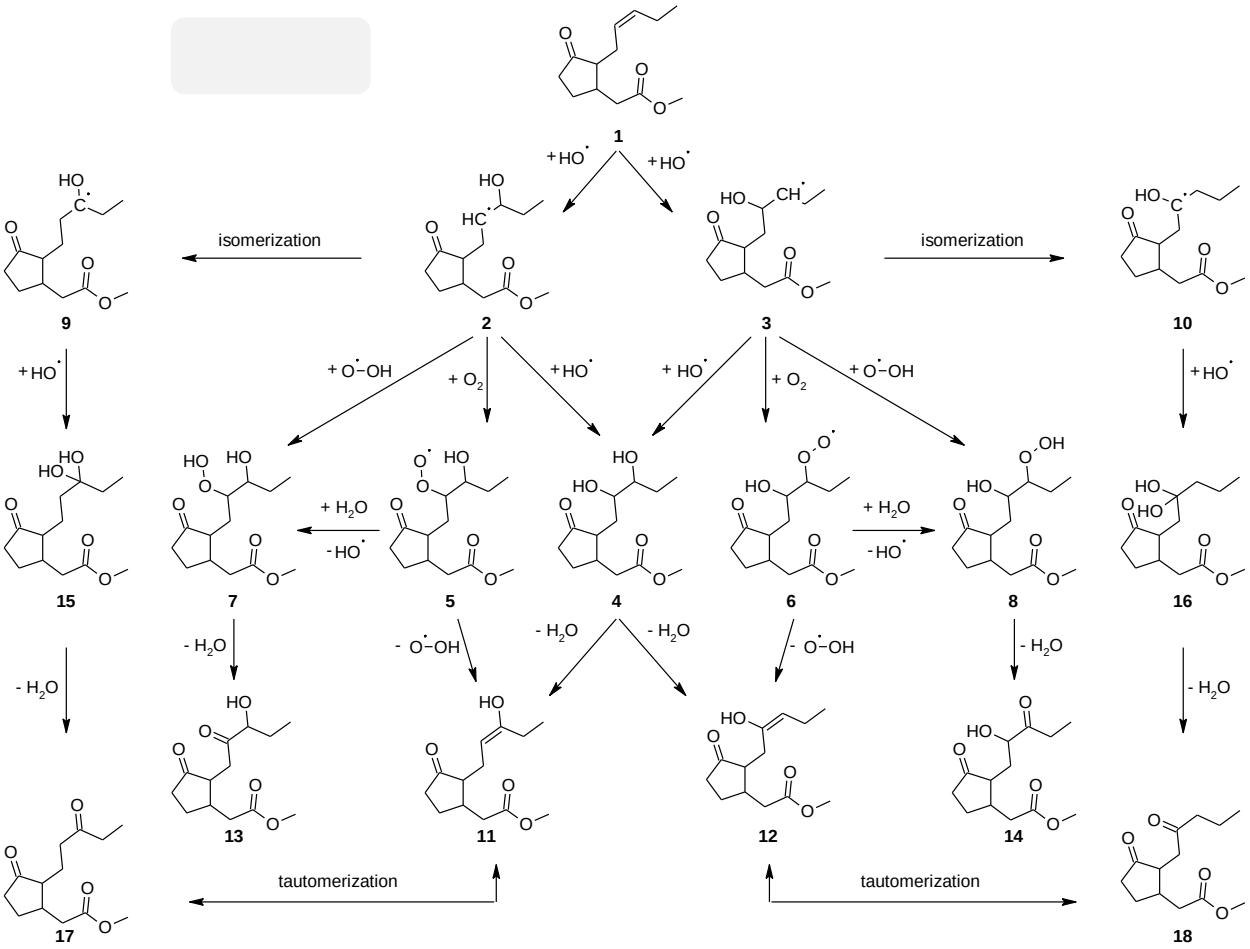

Figure 5.3. Potential methyl jasmonate oxidation reaction mechanism when exposed to UV light and hydroxyl radicals in an aqueous environment.

Figure 5.4 shows the TIC HPLC-ESI-MS chromatograms of an equimolar (2mM) solution of MeJa and H_2O_2 before (top) and after reaction with ˙OH (bottom). Before reaction, MeJa is the largest peak observed with a decay rate of 0.02 ± 0.001 hr^{-1}. After reaction, a number of additional peaks are observed at retention times ranging from 18-24 minutes due to formed products. Based on the observed EIC mass spectra (see Appendix section A7), suspected products were tentatively assigned to individual peaks (Figure 5.5) and are summarized in Table 5.1. (Mass spectral data of each peak in the TIC is available in Appendix section A9.) The mass spectral analysis revealed several peaks with retention times corresponding to a molecular formula as a result of the ˙OH radical addition occurring on either side of the double bond producing structural isomers (2, 3, 9, and 10 from Figure 5.3). From the observed mass spectra, we propose four product structures which are formed during ˙OH oxidation of MeJa and are in agreement with products formed in Figure 5.3 (4, 7-8, and 11-18). These identified products account for an estimated 13.7% of the oxidized parent MeJa, and approximately 20.3% of the measured 67.6 ± 10% SOA mass yielded from MeJa oxidation [17].

Table 5.1. MeJa product summary.

Compound	Chemical Formula	Molecular Weight	Compound Number	[M+H]+	EIC Scan
MeJa	$C_{13}H_{20}O_3$	224.3	1	225.15	225-228
MeJa + O	$C_{13}H_{20}O_4$	240.3	11, 12, 17, 18	241.14	241-245
MeJa + OH + O	$C_{13}H_{20}O_5$	256.3	13, 14	257.14	257-260
MeJa + 2 OH	$C_{13}H_{22}O_5$	258.3	4, 15, 16	259.15	259-262
MeJa + 2 OH + O	$C_{13}H_{22}O_6$	274.3	7, 8	275.15	275-278

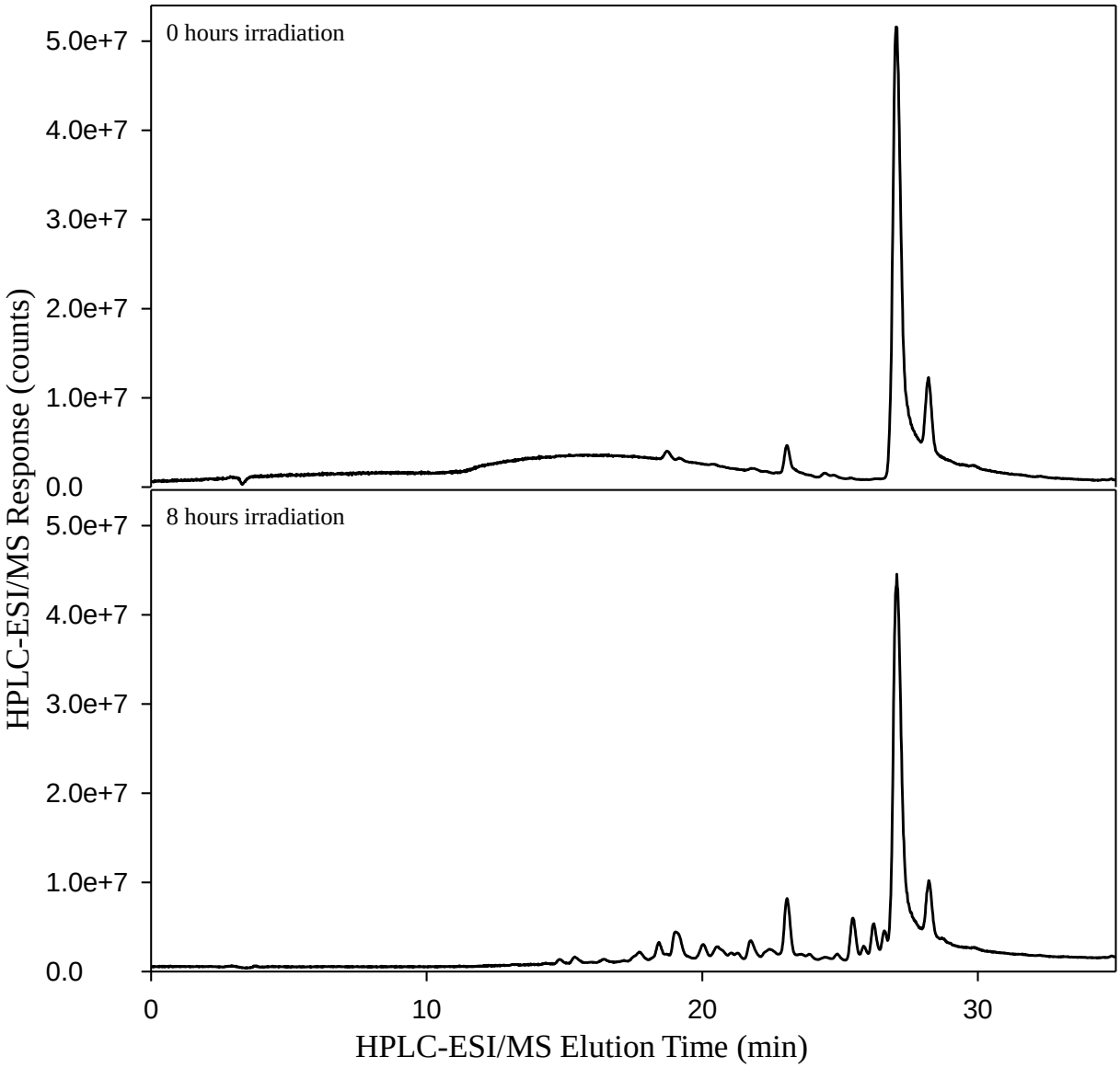

Figure 5.4. Total ion chromatograph (HPLC-ESI/MS) of 2mM MeJa with 2 mM H_2O_2 exposed to AM1.0 and 295 nm long pass filtered UV light: 0 hours irradiation (top), 8 hours irradiation (bottom).

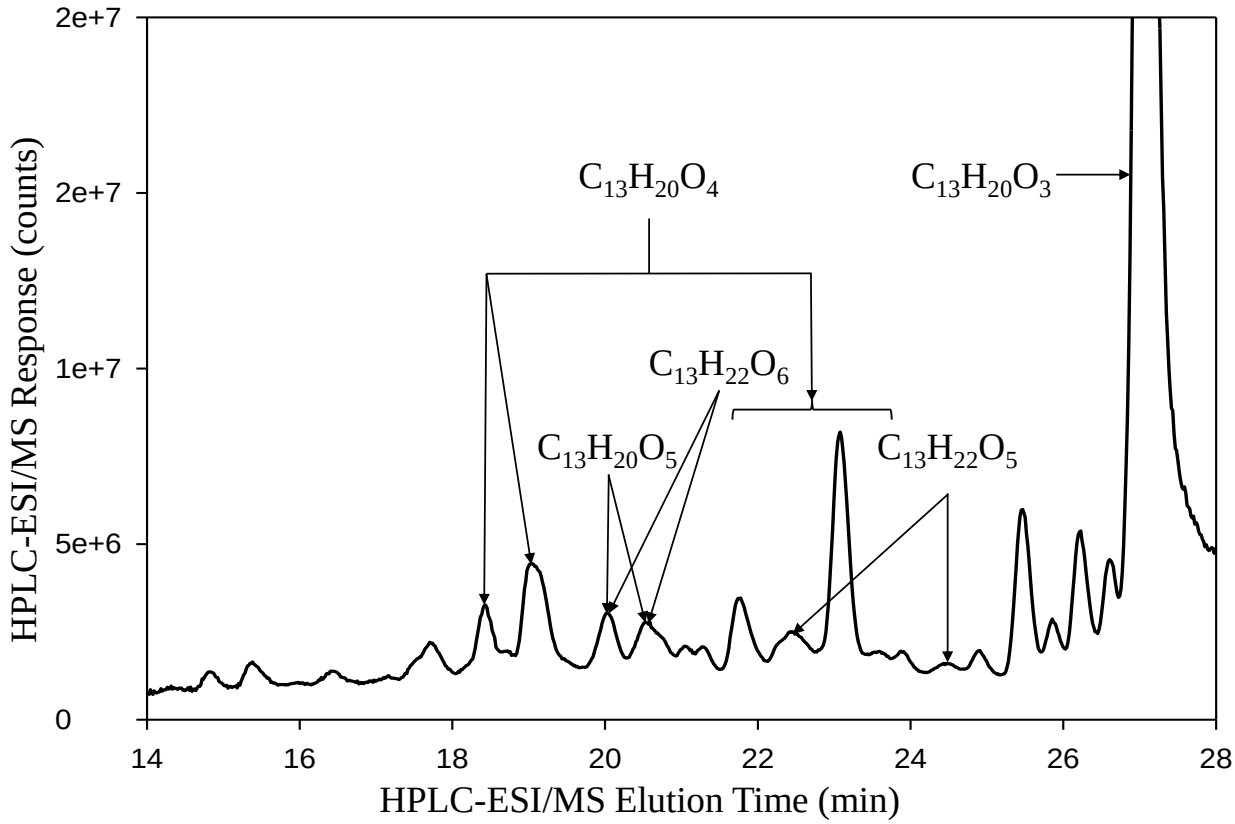

Figure 5.5. HPLC-ESI/MS TIC of 2mM MeJa with 2 mM H2O2 exposed to UV light (filtered with AM1.0 and 295 nm long pass filter) for 8 hours with identified products labeled.

Figure 5.6 shows the proposed mechanism for the reaction of methyl salicylate with hydroxyl radicals. Although the formation of the phenoxyl radical (5) directly from MeSa (1) and ˙OH via hydrogen abstraction is thermodynamically favored, the reaction mainly proceeds by OH radical addition to the ring [46] leading to the formation of dihydroxycyclohexadienyl radicals preferentially at the *ortho*- (2) and *para*- (3) positions – the *meta*- and *ipso*- positions are minor and are not included in the scheme [30, 47-49]. In the presence of oxygen, the dihydroxycyclohexadienyl radicals (2 and 3) can be converted to the corresponding peroxyl radicals (6 and 7). The peroxyl radicals can then decompose by the elimination of $HO_2^{\cdot}$ to form dihydroxybenzenes (8 and 9), which can react with hydroxyl radicals and molecular oxygen and

lose an $HO_2^{\cdot}$, leading to the formation of compound 10. Additional reaction pathways to consider are the dihydroxycyclhexadienyl radicals (2 and 3) undergoing a spontaneous loss of a water molecule to yield H-adduct radicals (4), which can form a phenoxyl radical (5). The H-adduct radicals can recombine or react with the phenoxyl radical, leading to the formation of dimers 11-13, respectively [34, 50].

Figure 5.7 shows the TIC HPLC-ESI-MS chromatograms of MeSa before (top) and after reaction with ˙OH (middle), as well as the UV chromatogram of the final sample (bottom). In the case of methyl salicylate, both methods of compound detection are required since MeSa is only detectable in the UV absorbance chromatograms and not visible in the TIC. Some reaction products are detectable by UV absorbance, but they are all visible in the MS chromatograms. At time t=0, MeSa is observed (in UV). With 20 mM H_2O_2, MeSa decays at a rate of 0.11 ± 0.016 hr^{-1}. After reaction, additional product peaks are observed at retention times ranging from 22-27 minutes. Figure 5.8 shows the product peak assignments based on EIC mass spectra (in Appendix section A8) and summarized in Table 5.2. (Mass spectral data of each peak in the TIC is available in the Appendix section A9.) The product peak assignments reveal two peaks with the same molecular formula as a result of the ˙OH radical addition occurring on different phenolic carbons producing structural isomers (8 and 9), as displayed in Figure 5.6. According to Figure 5.8, the MeSA dimer ($C_{16}H_{14}O_6$) co-elutes with the dihydroxybenzene compound ($C_8H_8O_4$). Figure 5.9 confirms the presence of the dimer, as well as the other two identified product compounds, in the mass spectra of the final sample without its presence in the initial sample. Additionally, the dark experiments revealed no evidence of product formation. We propose three product structures from the observed mass spectra which are formed during ˙OH oxidation of MeSa and are in agreement with products formed in Figure 5.6. Estimation of

product yield involved one extra step more than the MeJa product yield due to the lack of response that MeSa exhibited in the MS analysis. Methyl cinnamate ($C_{10}H_{10}O_2$) is a compound similar to methyl salicylate and was used as an external standard to adjust the product yield calculation to allow MeSa to be evaluated using HPLC UV absorbance, while the product compounds were evaluated using the HPLC-ESI/MS response. Equation 5.1 was used to estimate the product yield of MeSa to be 24.2%, which is 31.6% of the reported 76.5 ± 16% SOA mass yield [17].

$$Y_{product} = \frac{\sum_{MS} illuminated\ product\ peak\ area - \sum_{MS} dark\ product\ peak\ area}{(MeSa\ area_{t=0} - MeSa\ area_{t=8})_{UV} \times \left(\frac{MS}{UV}\right)_{MeCin}} \times 100\% \qquad (5.1)$$

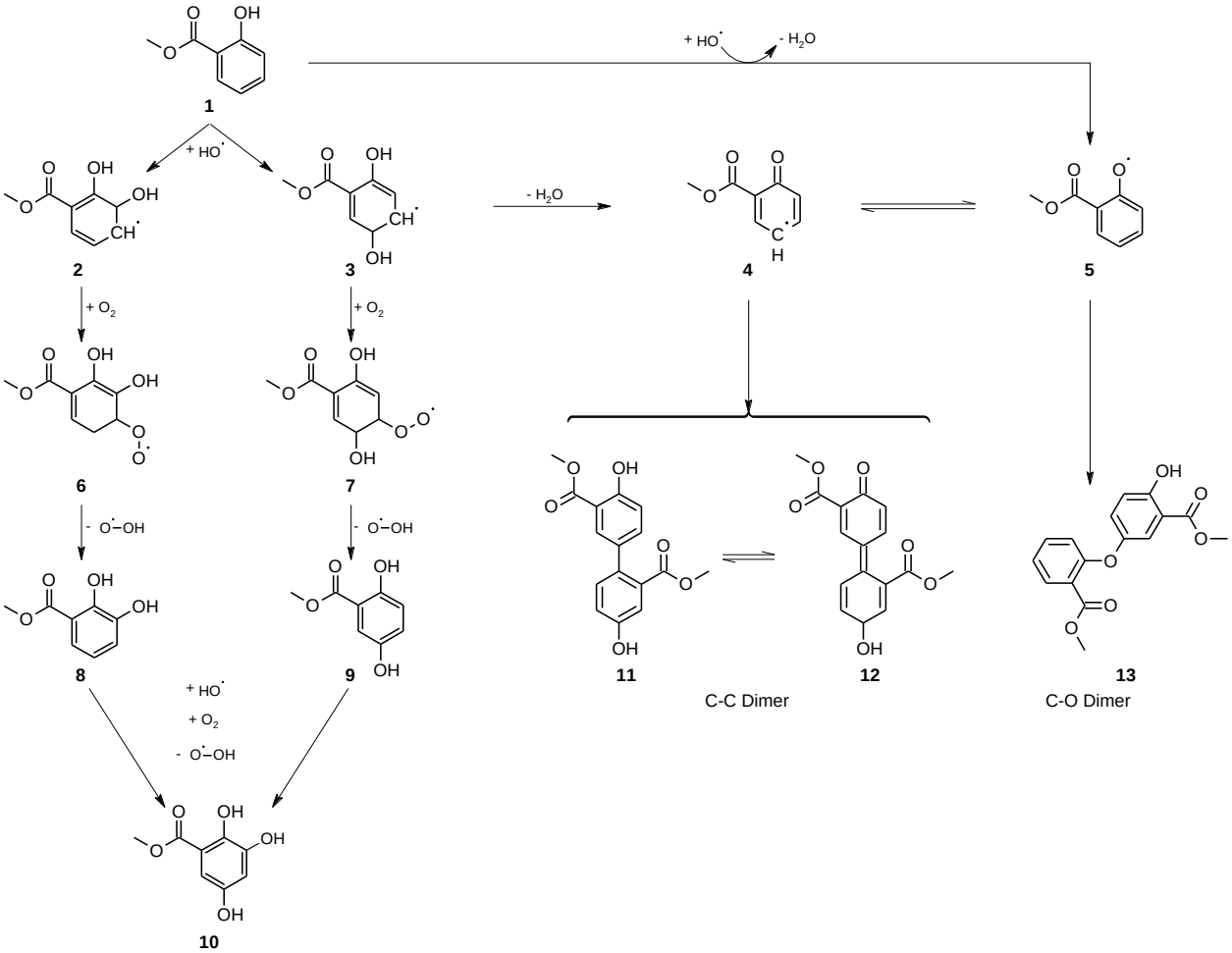

Figure 5.6. Potential methyl salicylate oxidation reaction mechanism when exposed to UV light and hydroxyl radicals in an aqueous environment.

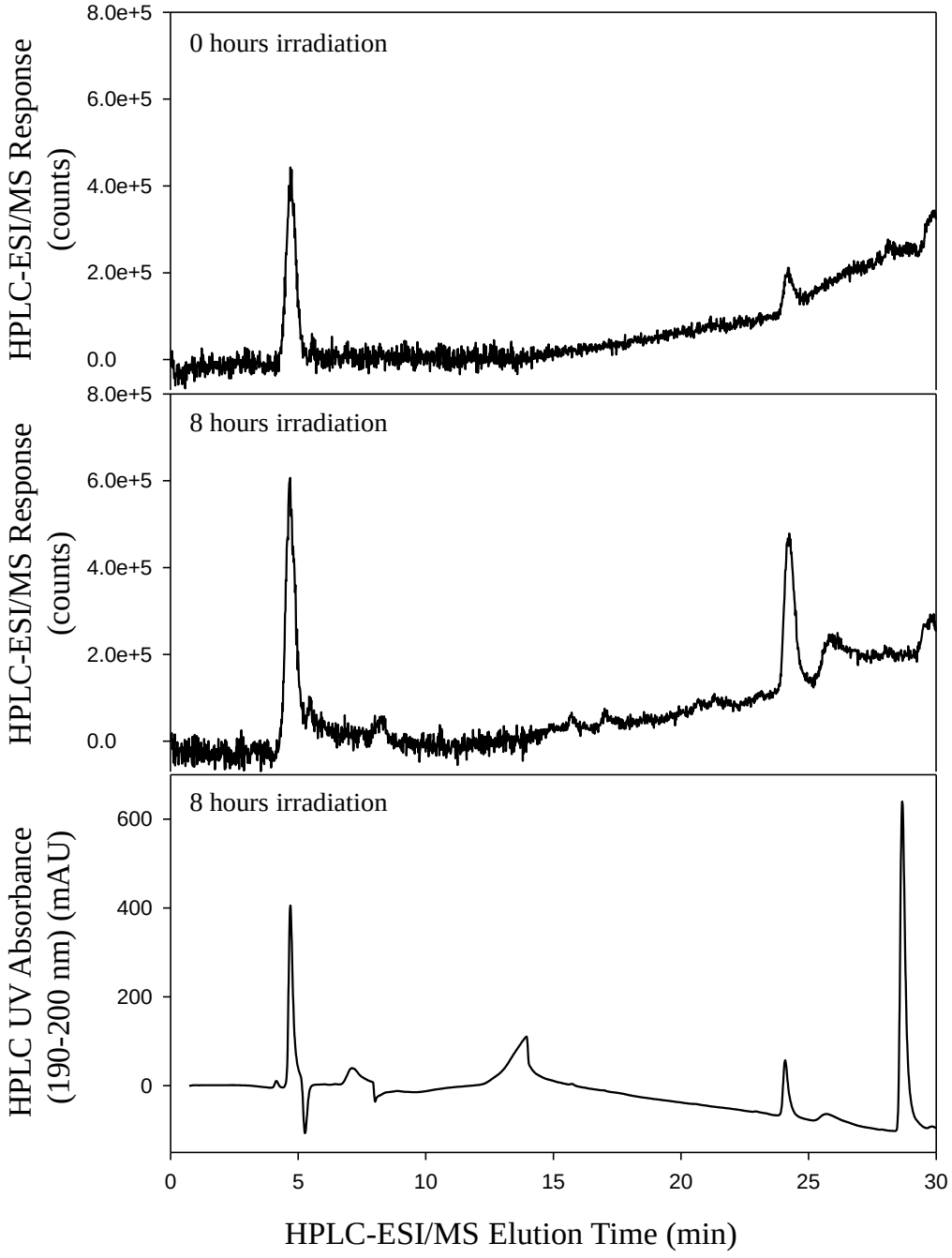

Figure 5.7. HPLC-ESI/MS TIC of 2mM MeSa with 20 mM H2O2 irradiated for 0 hours (top) and 8 hours (middle) and UV chromatogram irradiated for 8 hours (bottom).

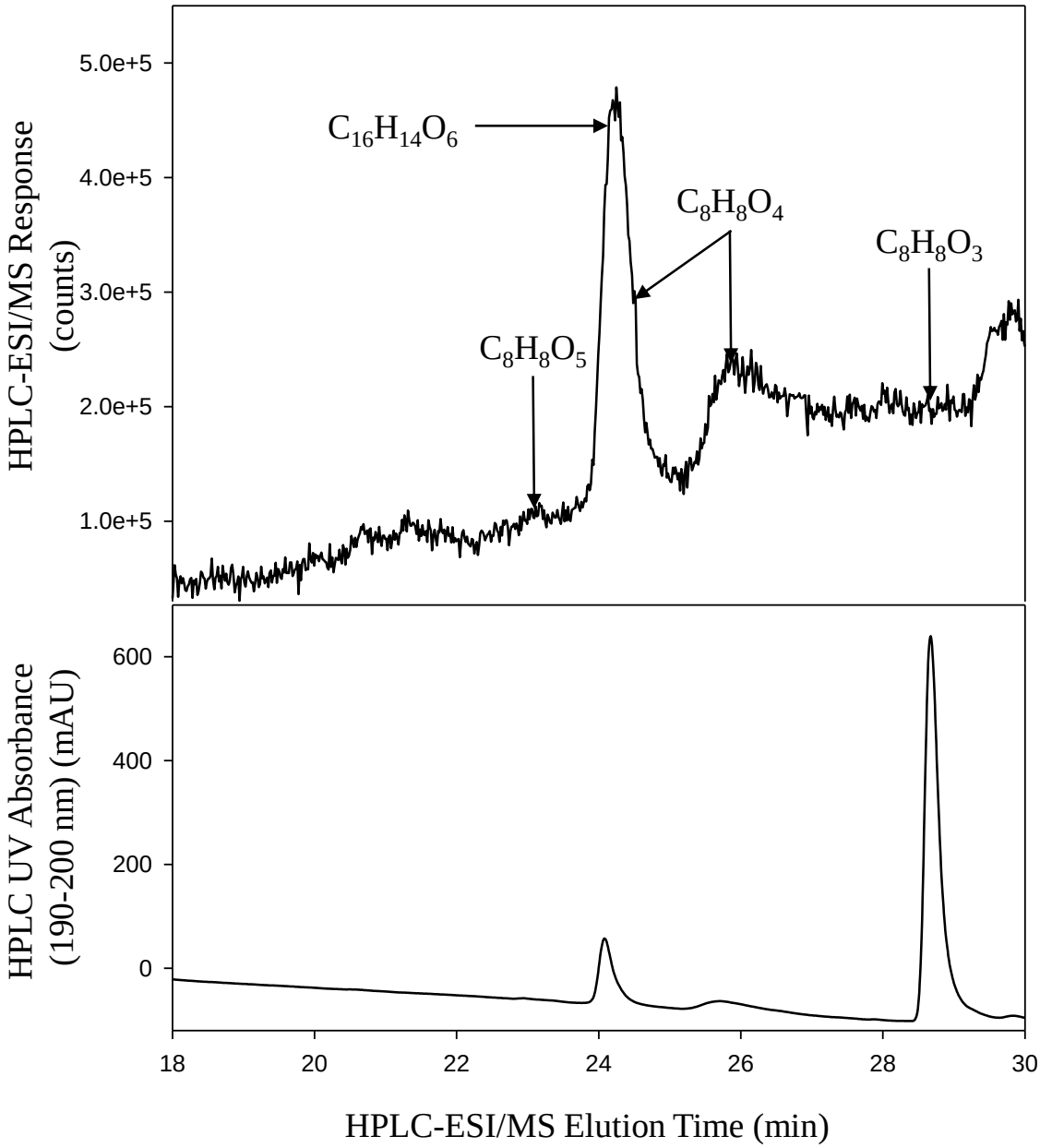

Figure 5.8. HPLC-ESI/MS TIC (top) and UV chromatogram (bottom) of 2mM MeSa with 20 mM H2O2 irradiated for 8 hours with identified products labeled.

Table 5.2. MeSa product summary.

Compound	Chemical Formula	Molecular Weight	Compound Number	$[M+H]^+$	EIC Scan
MeSa	$C_8H_8O_3$	152.15	1	153.05	152-155
MeSa + O	$C_8H_8O_4$	168.15	8, 9	169.05	168-172
MeSa + 2 O	$C_8H_8O_5$	184.15	10	185.04	185-189
MeSa + MeSa	$C_{16}H_{14}O_6$	302.28	11, 12, 13	303.09	302-305

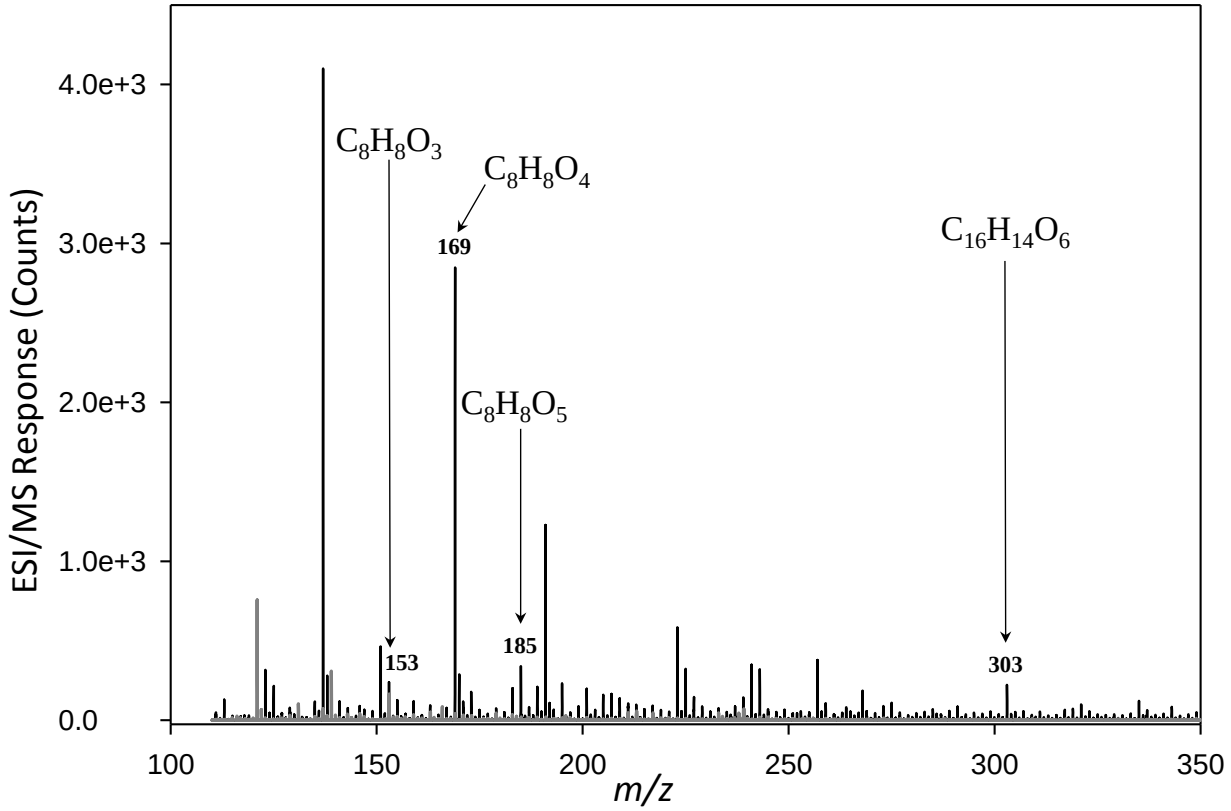

Figure 5.9. Mass spectra (without chromatographic separation) of 2mM MeSa with 20 mM H2O2 irradiated for 0 hours (grey) and 8 hours (black) with identified products labeled.

Henry's Law Constants and Vapor Pressure Estimations for Products

To determine if products from the oxidation of MeJa and MeSa will remain in the aqueous phase and contribute to SOA mass, we estimated the Henry's law constants (HLC) and vapor pressures of the identified products from Figures 5.3 and 5.6. Previous studies have shown that Henry's law constants and vapor pressure estimates can vary several orders of magnitude depending on the methodology used, especially for multi-functional organic molecules in which the effects of hydrogen-bonding cannot be fully accounted for; therefore, several methods were chosen and the results are listed in Table 5.3.

Table 5.3. Estimated Vapor Pressures and Henry's Law Constants of MeJa, MeSa, and their oxidation products from Figures 5.3 and 5.6.

Compound	Class	Mech. Num.	Vapor Pressure Estimates (atm)			Henry's Law Contants ($M \cdot atm^{-1}$)		
			SIMPOL [18]	Sparc [51]	MPBPVP [52]	Sparc [53]	Bond Estimation [52]	Group Estimation [52]
MeJa	$C_{13}H_{20}O_3$	1	1.2×10^{-6}	1.2×10^{-6}	4.4×10^{-7}	4.4×10^{3}	2.3×10^{3}	7.2×10^{4}
MeJa + O	$C_{13}H_{20}O_4$	11	7.6×10^{-9}	2.3×10^{-9}	3.6×10^{-10}	1.3×10^{7}	7.8×10^{6}	N/A
		12	7.6×10^{-9}	6.1×10^{-8}	3.6×10^{-10}	3.2×10^{4}	7.8×10^{6}	N/A
		17	1.7×10^{-7}	8.1×10^{-8}	7.6×10^{-8}	2.4×10^{6}	5.2×10^{6}	2.9×10^{8}
		18	1.7×10^{-7}	1.1×10^{-7}	7.6×10^{-8}	1.8×10^{6}	5.3×10^{6}	2.9×10^{8}
MeJa + OH + O	$C_{13}H_{20}O_5$	13	1.1×10^{-9}	2.3×10^{-9}	2.0×10^{-10}	2.4×10^{8}	3.3×10^{7}	N/A
		14	1.1×10^{-9}	3.1×10^{-9}	2.0×10^{-10}	4.7×10^{8}	3.3×10^{7}	N/A
MeJa + 2 OH	$C_{13}H_{22}O_5$	4	6.4×10^{-11}	7.0×10^{-10}	4.3×10^{-11}	6.7×10^{9}	1.5×10^{9}	5.3×10^{13}
		15	6.4×10^{-11}	1.7×10^{-10}	7.9×10^{-11}	2.7×10^{10}	1.5×10^{9}	N/A
		16	6.4×10^{-11}	1.4×10^{-10}	7.9×10^{-11}	2.0×10^{10}	1.5×10^{9}	N/A
MeJa + 2 OH + O	$C_{13}H_{22}O_6$	7	3.5×10^{-11}	6.7×10^{-11}	4.3×10^{-11}	3.5×10^{11}	5.9×10^{11}	N/A
		8	3.5×10^{-11}	2.8×10^{-11}	4.3×10^{-11}	3.3×10^{11}	5.9×10^{11}	N/A
MeSa	$C_8H_8O_3$	1	3.0×10^{-6}	2.1×10^{-5}	4.3×10^{-5}	9.3×10^{2}	2.2×10^{2}	4.5×10^{5}
MeSa + O	$C_8H_8O_4$	8	2.3×10^{-8}	1.8×10^{-7}	6.6×10^{-8}	2.1×10^{5}	2.1×10^{6}	3.7×10^{9}
		9	2.3×10^{-8}	1.1×10^{-9}	6.6×10^{-8}	1.6×10^{10}	2.1×10^{6}	3.7×10^{9}
MeSa+ 2 O	$C_8H_8O_5$	10	1.7×10^{-10}	2.3×10^{-13}	2.3×10^{-9}	3.4×10^{10}	2.0×10^{10}	3.0×10^{13}
MeSa + MeSa	$C_{16}H_{14}O_6$	11	1.3×10^{-13}	3.9×10^{-15}	2.0×10^{-12}	6.3×10^{9}	4.3×10^{9}	1.4×10^{13}
		12	5.1×10^{-13}	4.2×10^{-16}	6.7×10^{-12}	3.6×10^{12}	1.1×10^{12}	N/A
		13	1.6×10^{-12}	5.6×10^{-16}	1.9×10^{-10}	4.3×10^{10}	1.6×10^{6}	2.5×10^{9}

All the identified products for both MeJa and MeSa oxidation have large HLCs ($>10^3$) suggesting that these compounds will stay in the aqueous phase and not volatize to the gas phase. Additionally, the identified products have significantly (up to 5 orders of magnitude) lower vapor pressures than their parent compound. This lower vapor pressure is expected because the identified products are higher in molecular weight as well as possess polar functional groups, such as the carbonyl or hydroxyl group, that interact favorably with water. The low volatility of these products suggests that after the aqueous-phase water evaporates, these products will remain in the particle phase and contribute to SOA mass.

CHAPTER 6
CONCLUSION

Green leaf volatiles are a potential source of secondary organic aerosol in the aqueous phase. GLVs do not photo-oxidize in the presence of UV light alone; an oxidant is required. Methyl jasmonate and methyl salicylate both oxidize in the presence of an oxidant, the hydroxyl radical, when aqueous solutions are exposed to UV light. These reactions are summarized in oxidation mechanisms presenting potential pathways for oxidation in aqueous environments in the presence of hydroxyl radicals and oxygen. The GLV oxidation products currently identified using HPLC-ESI/MS are consistent with the presented oxidation mechanisms. The identified oxidation products are higher in molecular weight than the parent GLV while simultaneously exhibiting a decrease in vapor pressure, which is a key factor to their potential to form SOA. These results are not only qualitative in that they identify aqueous phase oxidation products of GLVs, but they also quantify a percentage of identifiable products, thus substantiating the SOA mass yield products and connecting the mass yield to the identified yield. The identified products represent a significant amount (20.3% and 31.6%) of the SOA formed via aqueous phase GLV oxidation and helps close the GLV-contributed part of the mass balance of the atmospheric VOC cycle.

CHAPTER 7
FUTURE WORK

To continue the investigation of aqueous phase transformation of GLVs into SOA, oxidation reaction mechanisms must be developed for the reaction of MBO, HxO and HxAc in aqueous environments in the presence of ˙OH and oxygen. Using the established reactor and experimental design, bulk phase experiments should be performed and compound identification via HPLC-ESI/MS analysis should verify the suggested mechanisms. To extend experiments to include real samples, these bulk phase reactions should be examined in authentic fog water (currently stored frozen at LSU).

Finally, the current bulk phase reactor should be modified to house thin film experiments. The current lamp and filter combinations should remain the same, and the same PTFE block reactor should be used. To create a thin film of water, the Petri dish will be replaced with a 1'×1' glass slide (Technical Glass Products, Gonzales, LA, USA). Each glass slide is to be chemically treated to create a hydrophobic outer edge surround a hydrophilic inner square with straight edges and constant area. A solenoid pump with Amperite DFA series adjustable recycling timer (Cole Parmer, Vernon Hills, IL, USA) will provide a flow of solution at a constant flow rate over the slide. The reacting solution will exit the reactor and enter a sample reservoir from which a sample will be drawn at set intervals using a syringe and FEP sampling tube. To ensure a batch reaction, the sampling reservoir will serve as the reactor feed. The film thickness will be determined based on the flow rate and slide surface area. The aluminum heat exchanger will maintain the temperature inside the reactor at a constant 25°C, and the sampling reservoir should rest in a 25°C water bath. Samples should be drawn at set time intervals, and HPLC-ESI/MS analysis should be performed to measure GLV degradation and confirm product development. The investigation of GLVs as a source of SOA in thin film water phases will extend our

knowledge of GLV surface activity and complete the investigation of GLV reactions in fog droplets.

GLV oxidation reactions on a thin film will reveal further insight into oxidation reactions at the air/water interface. Kinetics may be enhanced and different products may be detected. Smaller reaction volumes will lead to higher concentrations of products; therefore, different products may be observed that were not visible in the bulk due to concentrations below the detection limit. Enhanced reactions at the surface may occur due to the availability of reactants and oxidants at the surface that may not exist in the bulk due to a partial solvation phenomenon at the interface which may inhibit the compounds to reach the bulk, leaving them present only at the interface. The more surface active GLVs will exhibit enhanced surface reactions.

REFERENCES

1. Agency, U.S.E.P. *Improving Air Quality in Your Community Glossary*. 2011; Available from: http://ofmpub.epa.gov/sor_internet/registry/termreg/searchandretrieve/glossariesandkeywordlists/search.do?details=&glossaryName=Improving%20Air%20Quality#formTop.

2. Goldstein, A.H. and I.E. Galbally, *Known and unexplored organic constituents in the earth's atmosphere.* Environmental Science & Technology, 2007. **41**(5): p. 1514-1521.

3. Kesselmeier, J. and M. Staudt, *Biogenic Volatile Organic Compounds (VOC): An Overview on Emission, Physiology and Ecology.* Journal of Atmospheric Chemistry, 1999. **33**(1): p. 23-88.

4. Chin, M., R. Kahn, and S. Schwartz, *Atmospheric Aerosol Properties and Climate Impacts.*, in *U.S. Climate Change Science Program and the Subcommittee on Global Change Research.*, N.A.a.S. Administration, Editor 2009.

5. Guenther, A., et al., *A global model of natural volatile organic compound emissions.* J. Geophys. Res., 1995. **100**(D5): p. 8873-8892.

6. König, G., et al., *Relative contribution of oxygenated hydrocarbons to the total biogenic VOC emissions of selected mid-European agricultural and natural plant species.* Atmospheric Environment, 1995. **29**(8): p. 861-874.

7. Atkinson, R. and J. Arey, *Atmospheric Degradation of Volatile Organic Compounds.* Chemical Reviews, 2003. **103**: p. 4605-4638.

8. Bamberger, I., et al., *BVOC fluxes above mountain grassland.* Biogeosciences, 2010. **7**(5): p. 1413-1424.

9. Peñuelas, J. and M. Staudt, *BVOCs and global change.* Trends in plant science, 2010. **15**(3): p. 133-144.

10. Atkinson, R. and J. Arey, *Gas-phase tropospheric chemistry of biogenic volatile organic compounds: a review.* Atmospheric Environment, 2003. **37, Supplement 2**(0): p. 197-219.

11. Goldan, P.D., et al., *The observation of a C5 alcohol emission in a North American pine forest.* Geophys. Res. Lett., 1993. **20**(11): p. 1039-1042.

12. Arey, J., et al., *The emission of (Z)-3-hexen-1-ol, (Z)-3-hexenylacetate and other oxygenated hydrocarbons from agricultural plant species.* Atmospheric Environment. Part A. General Topics, 1991. **25**(5–6): p. 1063-1075.

13. Winer, A.M., et al., *Emission rates of organics from vegetation in California's Central Valley.* Atmospheric Environment. Part A. General Topics, 1992. **26**(14): p. 2647-2659.

14. Matsui, K., *Green leaf volatiles: hydroperoxide lyase pathway of oxylipin metabolism.* Current Opinion in Plant Biology, 2006. **9**(3): p. 274-280.

15. Hamilton, J.F., et al., *Reactive oxidation products promote secondary organic aerosol formation from green leaf volatiles.* Atmos. Chem. Phys., 2009. **9**(11): p. 3815-3823.

16. Brilli, F., et al., *Qualitative and quantitative characterization of volatile organic compound emissions from cut grass.* Environmental Science & Technology, 2012.

17. Richards-Henderson, N.K., et al., *Aqueous Oxidation of Green Leaf Volatiles by Hydroxyl Radical as a Source of SOA: Part 1- Reaction Kinetics.* in preparation, 2013.

18. Pankow, J.F. and W.E. Asher, *SIMPOL.1: a simple group contribution method for predicting vapor pressures and enthalpies of vaporization of multifunctional organic compounds.* Atmos. Chem. Phys., 2008. **8**(10): p. 2773-2796.

19. Blando, J.D. and B.J. Turpin, *Secondary organic aerosol formation in cloud and fog droplets: a literature evaluation of plausibility.* Atmospheric Environment, 2000. **34**(10): p. 1623-1632.

20. Valsaraj, K.T., *A Review of the Aqueous Aerosol Surface Chemistry in the Atmospheric Context.* Open Journal of Physical Chemistry, 2012. **2**: p. 58-66.

21. Graedel, T.E. and C.J. Weschler, *Chemistry within aqueous atmospheric aerosols and raindrops.* Rev. Geophys., 1981. **19**(4): p. 505-539.

22. Raja, S., et al., *Fog chemistry in the Texas–Louisiana Gulf Coast corridor.* Atmospheric Environment, 2008. **42**(9): p. 2048-2061.

23. Valsaraj, K.T., *Elements of Environmental Engineering*. 3 ed2009, New York: Taylor and Francis Publishers.

24. Donaldson, D.J. and K.T. Valsaraj, *Adsorption and Reaction of Trace Gas-Phase Organic Compounds on Atmospheric Water Film Surfaces: A Critical Review.* Environmental Science & Technology, 2010. **44**(3): p. 865-873.

25. Liyana-Arachchi, T.P., et al., *Molecular Modeling of the Green Leaf Volatile Methyl Salicylate on Atmospheric Air/Water Interfaces.* The Journal of Physical Chemistry A, 2013. **117**(21): p. 4436-4443.

26. Liyana-Arachchi, T.P., et al., *Molecular simulations of green leaf volatiles and atmospheric oxidants on air/water interfaces.* Physical Chemistry Chemical Physics, 2013.

27. Chen, J., et al., *Uptake and UV-Photooxidation of Gas-Phase PAHs on the Surface of Atmospheric Water Films. 1. Naphthalene.* The Journal of Physical Chemistry A, 2006. **110**(29): p. 9161-9168.

28. Faust, B.C., *Photochemistry of Clouds, Fogs, and Aerosols.* Environmental Science & Technology, 1994. **28**(5): p. 216A-222A.

29. Prinn, R.G., et al., *Atmospheric trends and lifetime of CH3CCl3 and global OH concentrations. (trichloroethane; hydroxyl radical).* Science, 1995. **269**(5221).

30. Matsuura, T. and K. Omura, *Photochemical Hydroxylation of Aromatic Compounds.* Synthesis, 1974. **1974**(3): p. 173.

31. Faust, B.C. and J.M. Allen, *Aqueous-phase photochemical formation of hydroxyl radical in authentic cloudwaters and fogwaters.* Environmental Science & Technology, 1993. **27**(6): p. 1221-1224.

32. Dainton, F.S. and J. Rowbottom, *The primary radical yield in water. A comparison of the photolysis and radiolysis of solutions of hydrogen peroxide.* Transactions of the Faraday Society, 1953. **49**(0): p. 1160-1173.

33. Christensen, H., K. Sehested, and H. Corfitzen, *Reactions of hydroxyl radicals with hydrogen peroxide at ambient and elevated temperatures.* The Journal of Physical Chemistry, 1982. **86**(9): p. 1588-1590.

34. Heath, A.A., F.S. Ehrenhauser, and K.T. Valsaraj, *Effects of temperature, oxygen level, ionic strength, and pH on the reaction of benzene with hydroxyl radicals in aqueous atmospheric systems.* Journal of Environmental Chemical Engineering, 2013(0).

35. Mentel, T.F., et al., *Secondary aerosol formation from stress-induced biogenic emissions and possible climate feedbacks.* Atmos. Chem. Phys. Discuss., 2013. **13**(3): p. 7463-7502.

36. Seinfeld, J.H. and J.F. Pankow, *Organic Atmospheric Particulate Material.* Annual Review of Physical Chemistry, 2003. **54**(1): p. 121-140.

37. Herckes, P., et al., *Organic Matter in Central California Radiation Fogs.* Environmental Science & Technology, 2002. **36**(22): p. 4777-4782.

38. Google, *2310 Ben Hur Rd. Baton Rouge, LA 78020*, 2013. p. Street map. Satellite map.

39. OECD, *OECD Guideline for the Testing of Chemicals No. 107: Partition Coefficient (n-octanol/water): Shake Flask Method*, 1995, OECD Publishing. p. 4.

40. Marrero, J. and R. Gani, *Group-Contribution-Based Estimation of Octanol/Water Partition Coefficient and Aqueous Solubility.* Industrial & Engineering Chemistry Research, 2002. **41**(25): p. 6623-6633.

41. *ASTM G173-03 Reference Spectra*, in *Terrestrial Reference Spectra for Photovoltaic Performance Evaluation*, ASTM (American Society for Testing Materials) International.

42. Anastasio, C. and K.G. McGregor, *Chemistry of fog waters in California's Central Valley: 1. In situ photoformation of hydroxyl radical and singlet molecular oxygen.* Atmospheric Environment, 2001. **35**(6): p. 1079-1089.

43. Cordova-Gomez, M., C. Iuga, and J.R. Alvarez-Idaboy, *Mechanisms and rate constants in the atmospheric oxidation of saturated esters by hydroxyl radicals: A theoretical study.* Int. J. Quantum Chem., 2012. **112**: p. 3508-3515.

44. Calvert, J.G., et al., *Mechanisms of Atmospheric Oxidation of the Alkanes*2008: Oxford University Press, Inc. 992.

45. Calvert, J.G., et al., *The Mechanisms of Atmospheric Oxidation of the Alkenes*2000: Oxford University Press, Inc. 552.

46. Calvert, J.G., et al., *The Mechanism of Atmospheric Oxidation of Aromatic Hydrocarbons*2002, New York, New York: Oxford University Press, Inc. 556.

47. Normann, R.O.C. and G.K. Radda, *Aromatic Hydroxylation: the Electrophilic Character of the Hydroxyl Radical, and its Significance in Biological Hydroxylation.* Proceedings of the Chemical Society, 1962(April): p. 133-164.

48. Raghavan, N.V. and S. Steenken, *Electrophilic reaction of the hydroxyl radical with phenol. Determination of the distribution of isomeric dihydroxycyclohexadienyl radicals.* Journal of the American Chemical Society, 1980. **102**(10): p. 3495-3499.

49. Omura, K. and T. Matsuura, *Photo-induced Reactions - IX The Hydroxylation of Phenols by the Photodecomposition of Hydrogen Peroxide in Aqueous Media.* Tetrahedron 1967. **24**: p. 3475-3487.

50. Sun, Y.L., et al., *Insights into secondary organic aerosol formed via aqueous-phase reactions of phenolic compounds based on high resolution mass spectrometry.* Atmos. Chem. Phys., 2010. **10**(10): p. 4809-4822.

51. Hilal, S.H., L.A. Carreira., and S.W. Karickhoff, *Prediction of the Vapor Pressure, Boiling Point, Heat of Vaporization, and Diffusion Coefficient of Organic Compounds*, in *QSAR & Combinatorial Science* 2003. p. 565-574.

52. EPA, U., *EPI (Estimations Programs Interface™) Suite for Microsoft Windows v 4.10*, in *United States Environmental Protection Agency*: Washington, DC, USA.

53. Hilal, S.H., L.A. Carreira, and S.W. Karickhoff, *Prediction of the Solubility, Activity Coefficient, Gas/Liquid and Liquid/Liquid Distribution Coefficients of Organic Compounds*, in *QSAR & Combinatorial Science*2004. p. 709.

54. Newport. *Diagram of solar air masses*. [cited 2013; Available from: http://www.newport.com/Air-Mass-Filters/377999/1033/info.aspx.

APPENDIX

A1. Fog Water

Table A1. Fog water collected in the Fall and Winter of 2012/2013. Start and end times refer to the times the fog collector was turned on and off. pH was measured using a PHR-146B Micro combination pH electrode (Lazar Research Laboratories, Inc., Los Angeles, CA, USA) and a pH meter (Oakton Acorn Series pH 6, Oakton Instruments, Vernon Hills, IL USA).

Date	Start Time (a.m.)	End Time (a.m.)	pH	Mass Collected (g)
10/05/12	7:32	10:00	5.31	166.36
10/12/12	6:39	9:00	6.67	26.87
10/13/12	4:20	8:50	7.05	0.00
10/25/12	4:20	8:50	6.24	122.61
10/26/12	5:00	9:15	6.26	614.92
11/01/12	5:55	9:00	6.03	265.78
11/02/12	4:40	9:00	6.48	0.00
11/03/12	4:00	8:40	6.01	434.65
11/05/12	11:21 p.m.	5:00	6.02	0.00
11/28/12	1:32	8:00	5.58	31.31
12/01/12	5:40	9:30	5.68	19.16
12/08/12	12:40	9:07	5.06	554.14
02/05/13	4:00	9:30	5.37	392.33
02/06/13	7:47	9:30	4.08	131.15
02/08/13	3:01	9:30	5.2	200.34
		Total Collected (g)		2959.62

A2. HPLC-UV/DAD Analysis

GLV concentrations were determined via HPLC analysis similar to the MBO analysis explained in Liyana-Arachchi *et al*., 2013 [26]. Analysis was performed using an Agilent 1100 HPLC-UV/DAD system consisting of a degasser (G1322A), a quaternary pump (G1311A), an autosampler (G1313A), a column compartment (G1316A) and a diode array detector (G1315A). 4 µL of each sample was injected onto a 2.1-mm×150-mm Ultra II^{TM} Aqueous C18 column (Restek Corp., Bellefonte, PA, USA) with 3-µm particle size, held at 25°C. The following water/acetonitrile gradient method was held at a 0.2 mL·min^{-1} flow rate: 100% water for the first five minutes, ramping linearly to 100% acetonitrile within 30 minutes, a 30 minute isocratic hold

at 100% acetonitrile, a 10-minute ramp back to 100% water, and a 20-minute post time hold at 100% water. The UV absorbance of each GLV was recorded with a signal averaged from 190 to 200 nm taking a data point every 2 s using the diode array detector with a slit of 4 nm. The GLV concentrations were determined from the measured peak area via calibration curves obtained with standard GLV solutions.

A3. 1-octanol

1-octanol is an aldehyde commonly used in environmental engineering due to its chemical similarity to the lipid content in living cells [23]. 1-octanol has the chemical formula $C_8H_{18}O$ with a formula weight of 130.23 and a chemical structure shown in Figure A3.

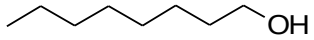

Figure A3. The chemical structure of 1-octanol.

A4. K_{OW} Experimental Design

Solutions containing 1-octanol-water phase ratios of 1:1, 2:1 and 1:2 were prepared in 40 mL vials by mixing 10 mL, 13.33 mL and 6.67 mL of a 0.01 M solution of GLV in 1-octanol with 10 mL, 13.33 mL and 6.67 mL of water-saturated 1-octanol, and 20 mL, 13.33 mL and 26.66 mL of 1-octanol-saturated water. Each 1-octanol-water phase ratio solution was tested in duplicate pairs. The vials were shaken in a 25°C shaking water bath to allow for ample contact and equilibration. The concentration of GLV in each phase was measured via HPLC daily until a constant K_{OW} was achieved – determined when the difference of the K_{OW} between the individual solutions was greater than the difference between the daily measurements.

A5. Surface Concentration

Surface concentrations were measured using a plot of σ versus $ln(C_w)$ where the slope corresponds to the surface concentration values of GLV at each bulk concentration.

$$m_{C_2} = \frac{\sigma_{C_2} - \sigma_{C_1}}{\ln(C_W)_{C_2} - \ln(C_W)_{C_1}} \quad \text{(A5.1)}$$

$$\Gamma_{C_2} = -\frac{m_{C_2}}{RT\rho_w} \quad \text{(A5.2)}$$

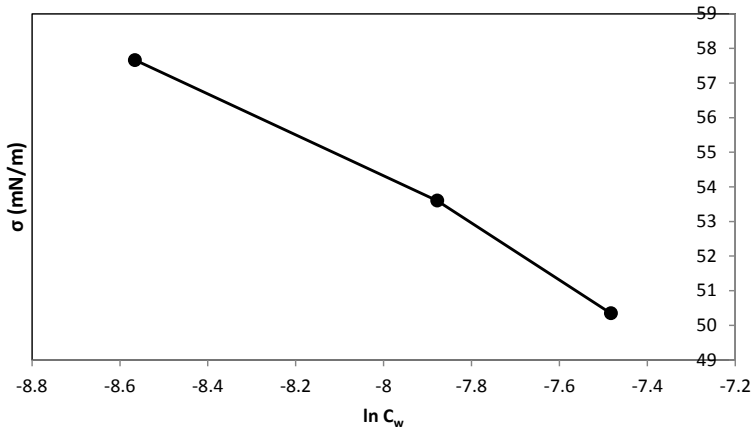

Figure A5.1. Plot of measured MeJa surface concentration versus the natural log of MeJa concentration in water.

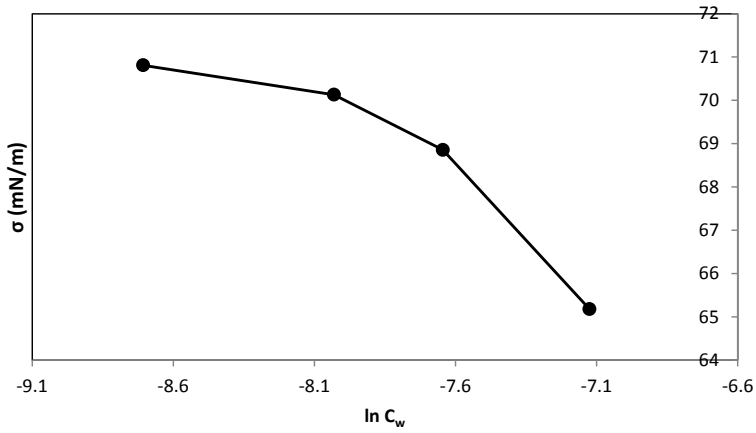

Figure A5.2. Plot of measured MeSa surface concentration versus the natural log of MeSa concentration in water.

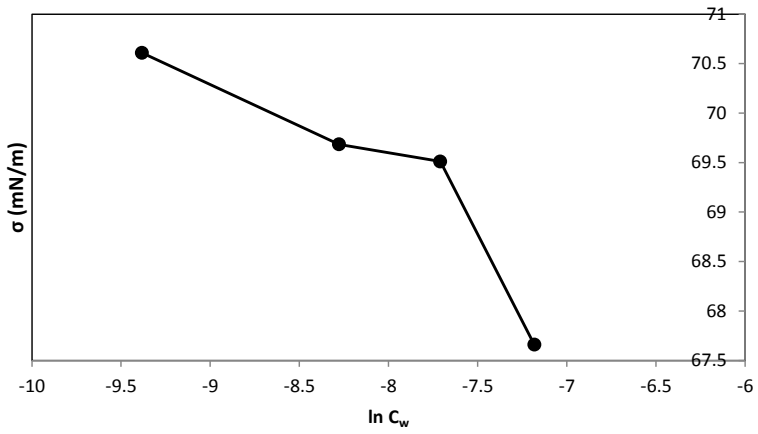

Figure A5.3. Plot of measured MBO surface concentration versus the natural log of MBO concentration in water.

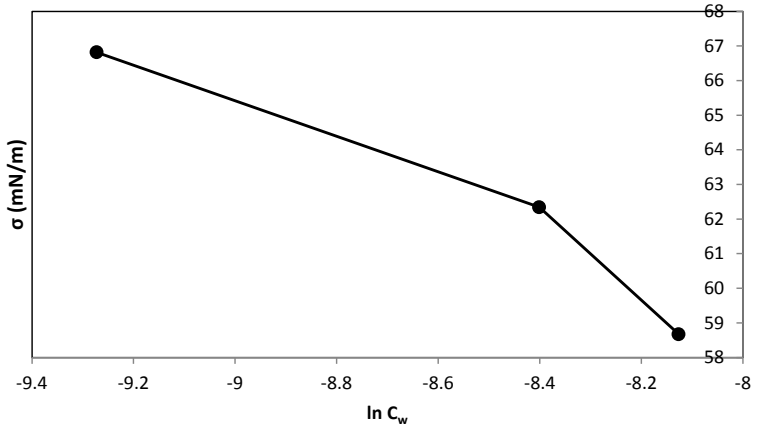

Figure A5.4. Plot of measured HxAc surface concentration versus the natural log of HxAc concentration in water.

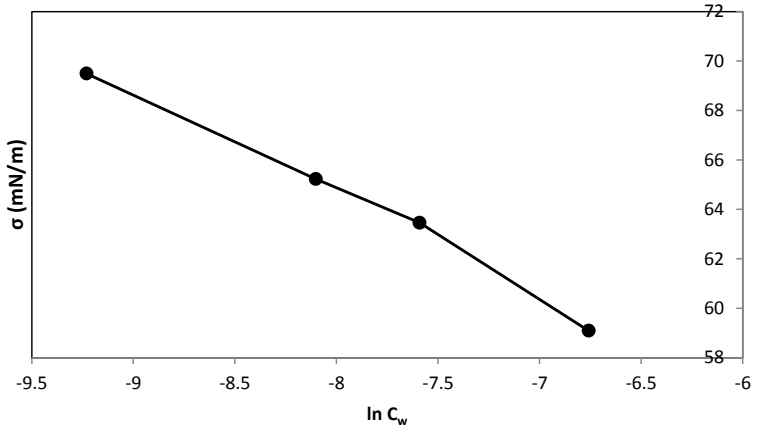

Figure A5.5. Plot of measured HxO surface concentration versus the natural log of HxO concentration in water.

A6. ASTM Guidelines

Table A6.1. ASTM G173-03 Reference Set Description [41]

Reference Set	Descrption
Extraterrestrial Radiation (ETR)	Extraterrestrial radiation at mean Earth-Sun distance – solar spectrum at top of atmosphere
Direct	Direct normal irradiance nearly parallel (0.5° divergent cone) radiation on surface with surface normal tracking (pointing to) the sun, excluding scattered sky and reflected ground radiation
Circumsolar	Spectral irradiance within ± 2.5 degree (5° diameter) field of view centered on the 0.5° diameter solar disk, but excluding the radiation from the disk
Global Tilt	Spectral radiation from solar disk plus sky diffuse and diffuse reflected from ground on south facing surface tilted 37° from horizontal

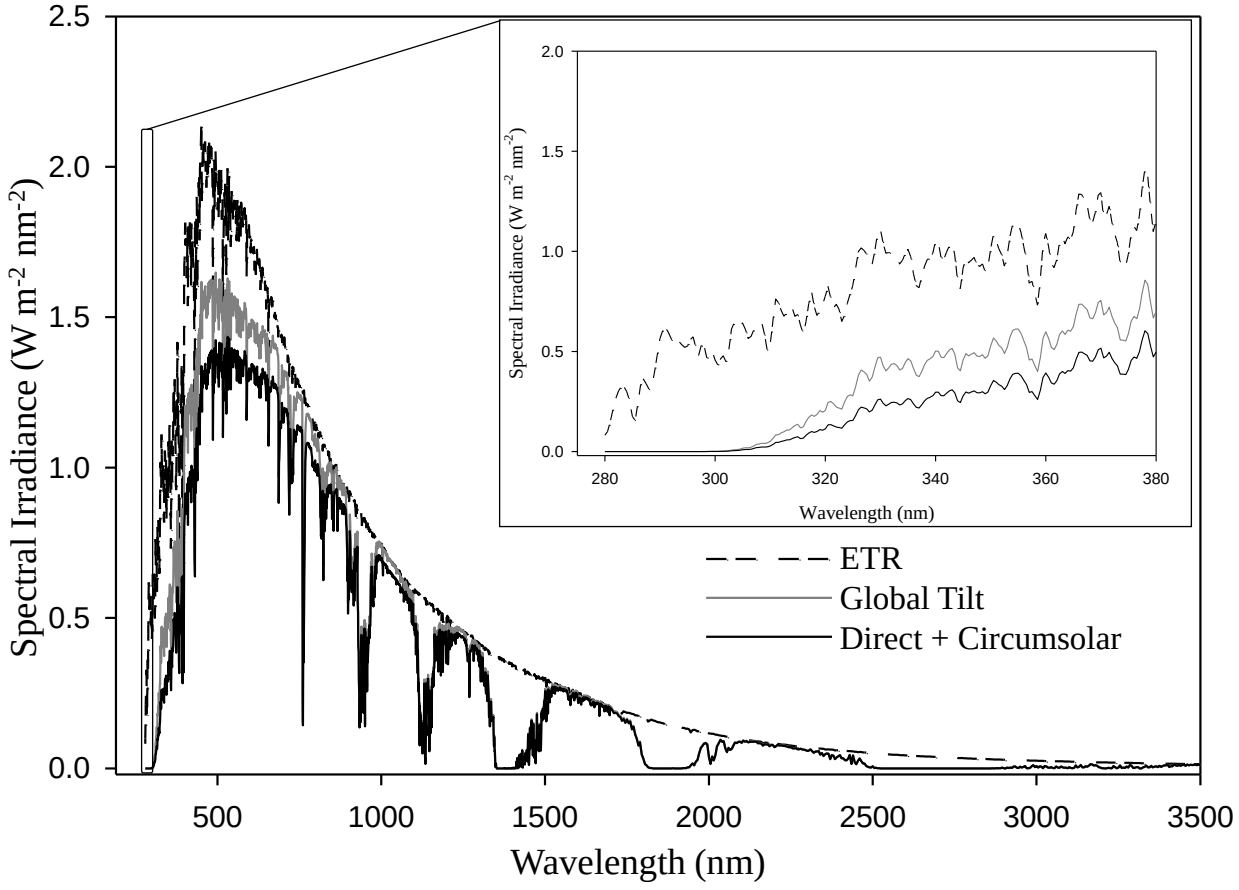

Figure A6.1. ASTM G173-03 Reference Spectra [41]

Table A6.2. Air mass filter types and associated functions. [54]

Air Mass Filter Type	Function
AM 0	Corrects the output of a xenon lamp to better match the solar spectrum found outside the earth's atmosphere.
AM 1 Direct	Simulates the solar spectrum at ground level when the sun is directly overhead
AM 1.5 Direct	Simulates the direct solar spectrum when the sun is at a zenith angle of 48.2° (ASTM E891).
AM 2 Direct	Approximates the solar spectrum when the sun is at a zenith angle of 60.1°
AM 1.5 Global	Matches the total (direct and diffuse) spectrum when the sun is at a zenith angle of 48.2° (ASTM E892)
AM 1.5 Global	Matches the total (direct and diffuse) spectrum when the sun is at a zenith angle of 48.2° (ASTM E892)

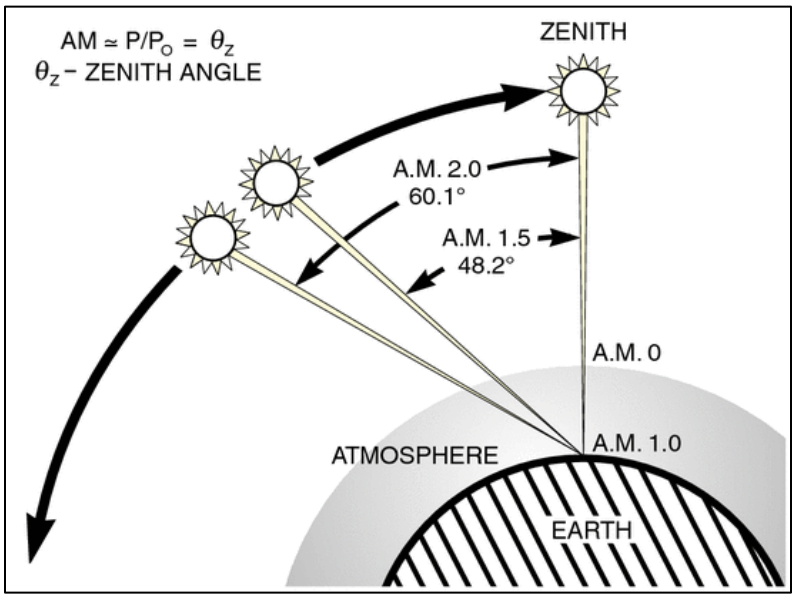

Figure A6.2. Sketch of air mass filter functions. [54]

A7. EIC Mass Spectral data for MeJa and products

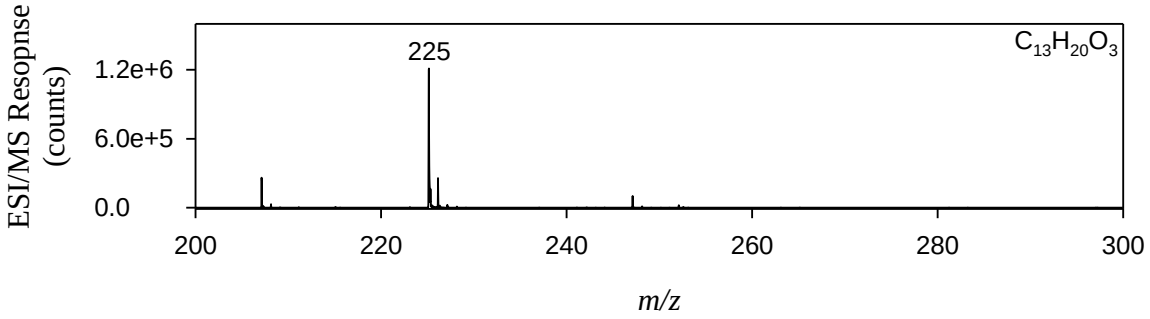

Figure A7.1. EIC mass spectra of MeJa peak.

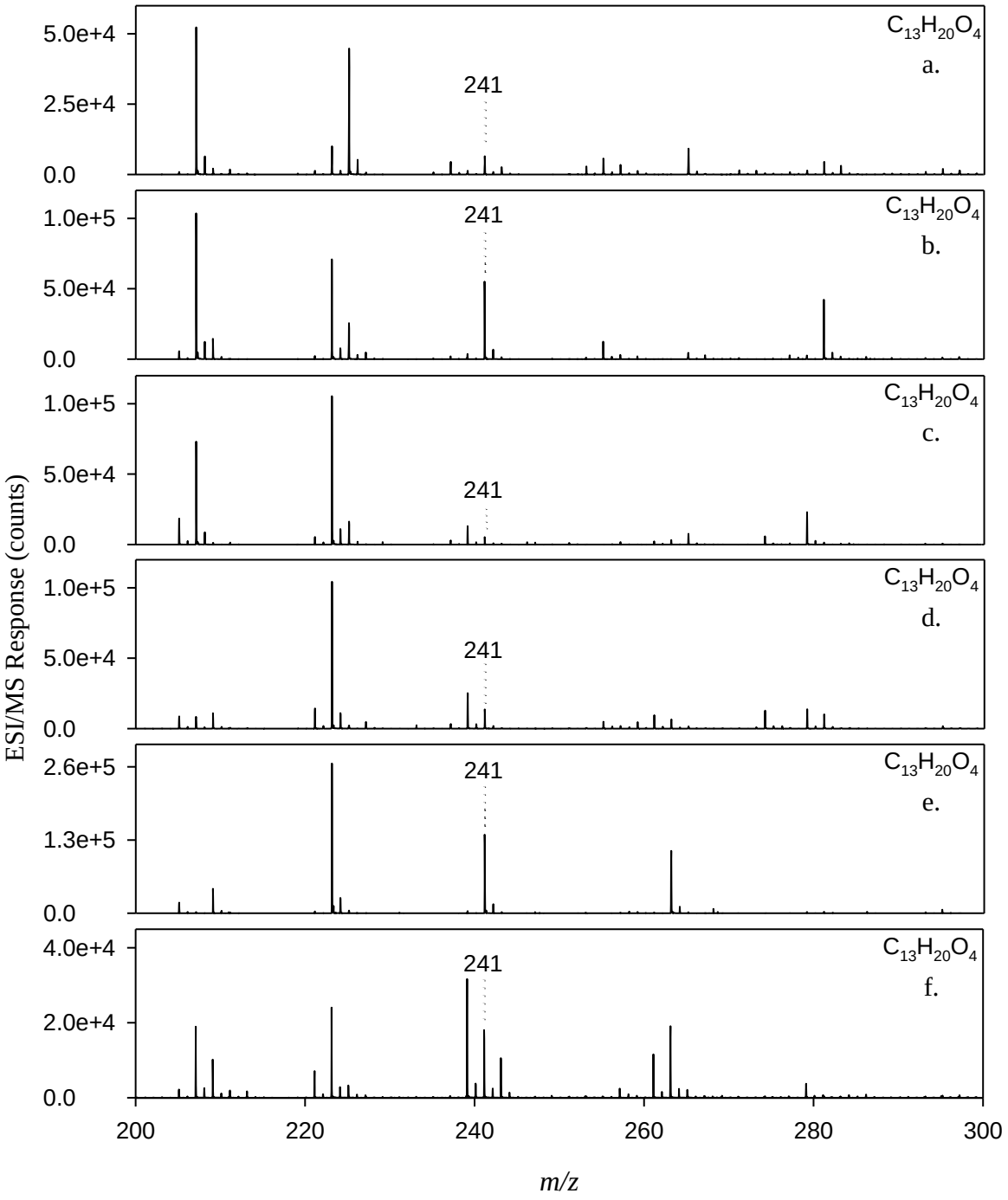

Figure A7.2. EIC mass spectra of assigned MeJa + O peaks in order of elution time. a. 18.4, b. 19.1, c. 21.7, d. 22.3, e. 22.7, f. 23.6.

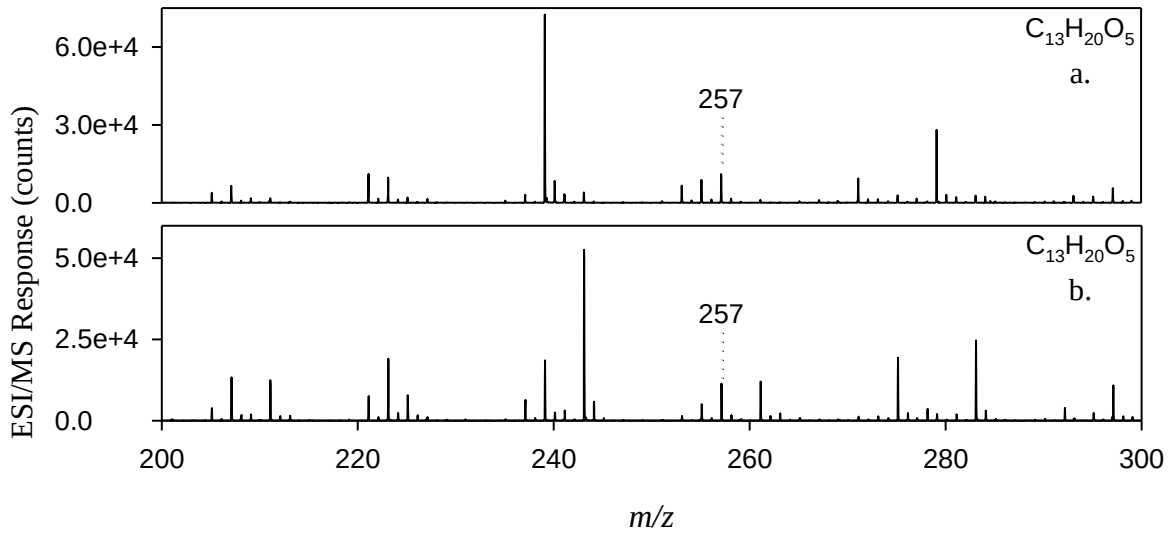

Figure A7.3. EIC mass spectra of assigned MeJa + OH + O peaks in order of elution time. a. 20.0, b. 20.5.

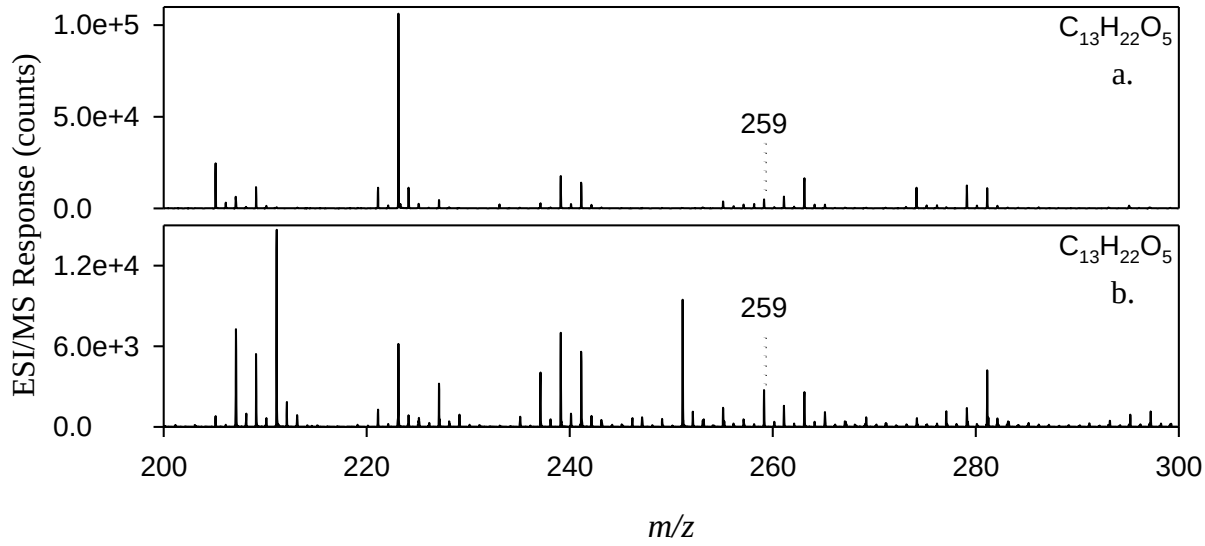

Figure A7.4. EIC mass spectra of assigned MeJa + 2 OH peaks in order of elution time. a. 22.4, b. 24.4.

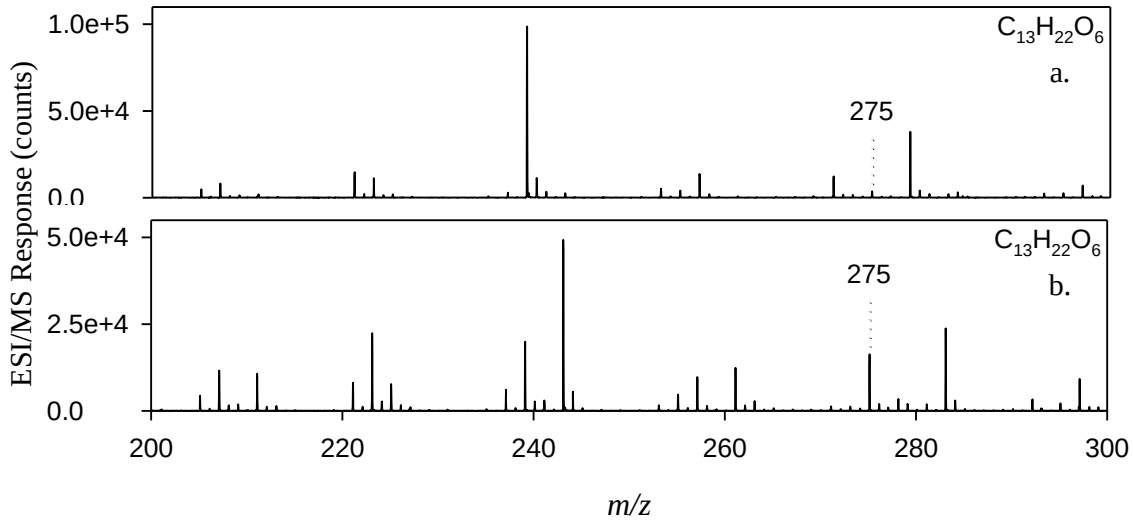

Figure A7.5. EIC mass spectra of assigned MeJa + 2 OH + O peaks in order of elution time. a. 20.0, b. 20.5.

A8. EIC Mass Spectral data for MeSa and products

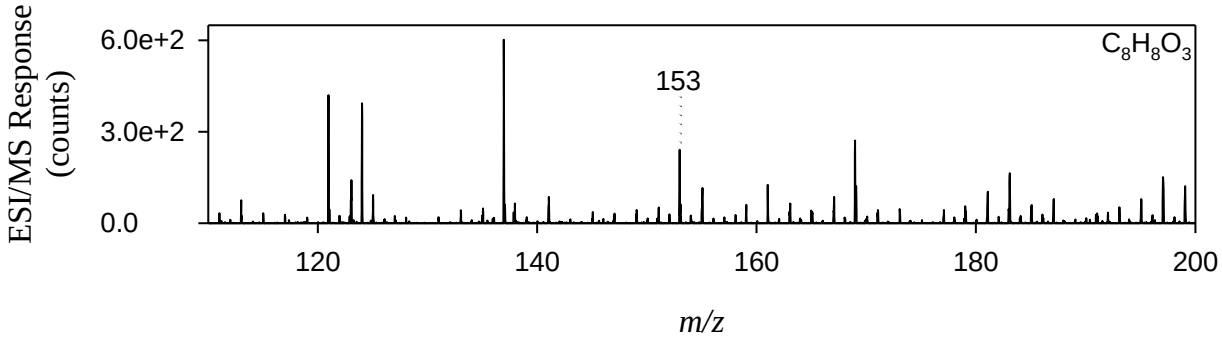

Figure A8.1. EIC mass spectra of MeSa peak.

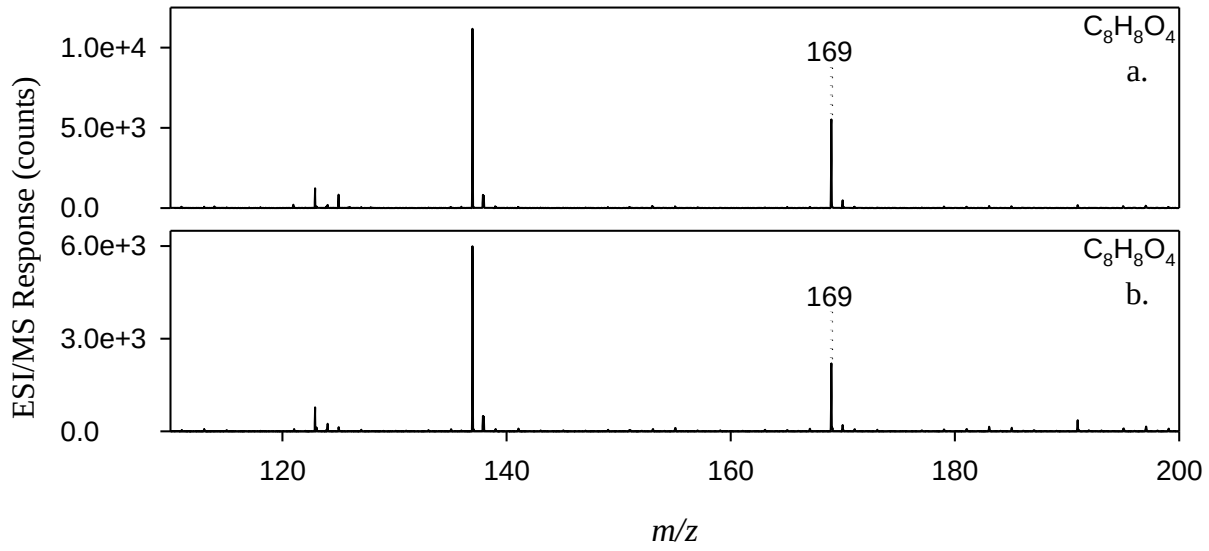

Figure A8.2. EIC mass spectra of assigned MeJa + O peaks in order of elution time. a. 24.2, b. 25.9.

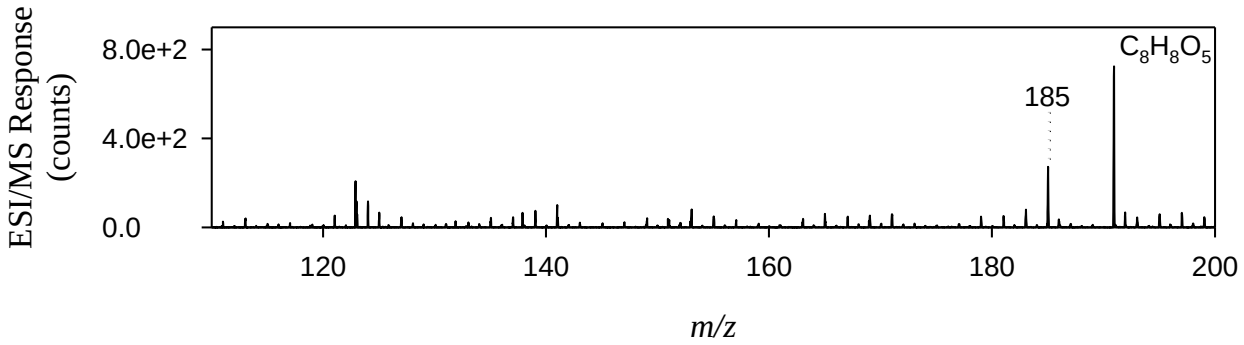

Figure A8.3. EIC mass spectra of assigned MeSa + O peak.

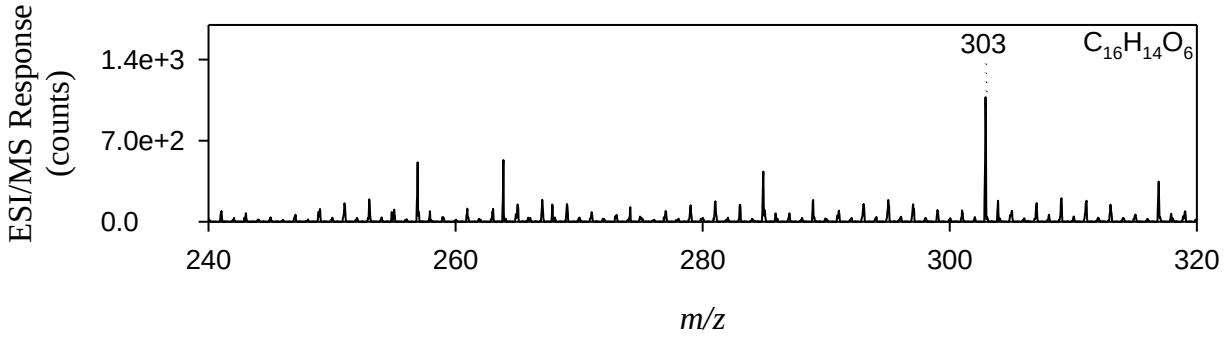

Figure A8.4. EIC mass spectra of assigned MeSa + MeSa peak.

A9. Mass spectral data of each peak in the TICs

The following figures are spectral data for each TIC peak. A figure of the TIC peak is represented with peaks labeled. Each peak label has a corresponding mass spectral figure to follow.

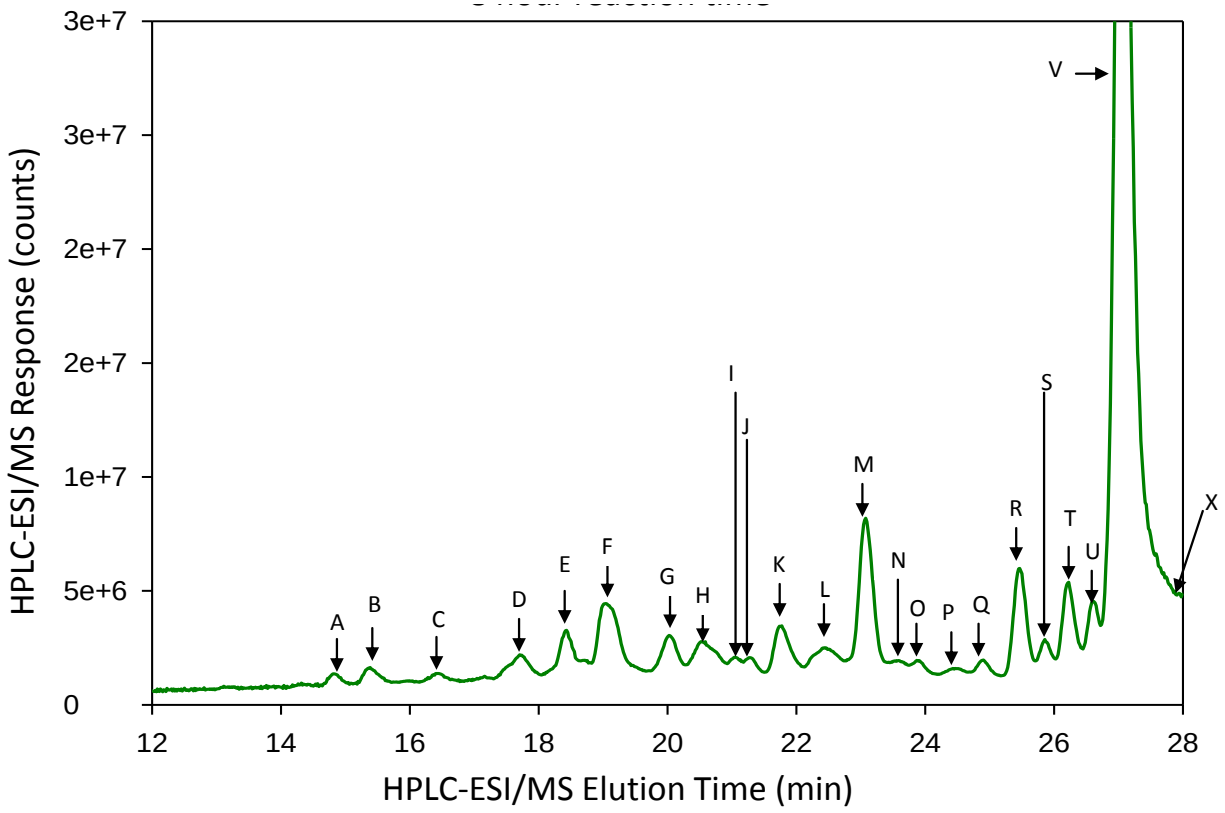

Figure A9.1. HPLC-ESI/MS TIC of 2mM MeJa with 2 mM H_2O_2 exposed to AM1.0 and 295 nm long pass filtered UV light for 8 hours irradiation with each peak labeled A-X.

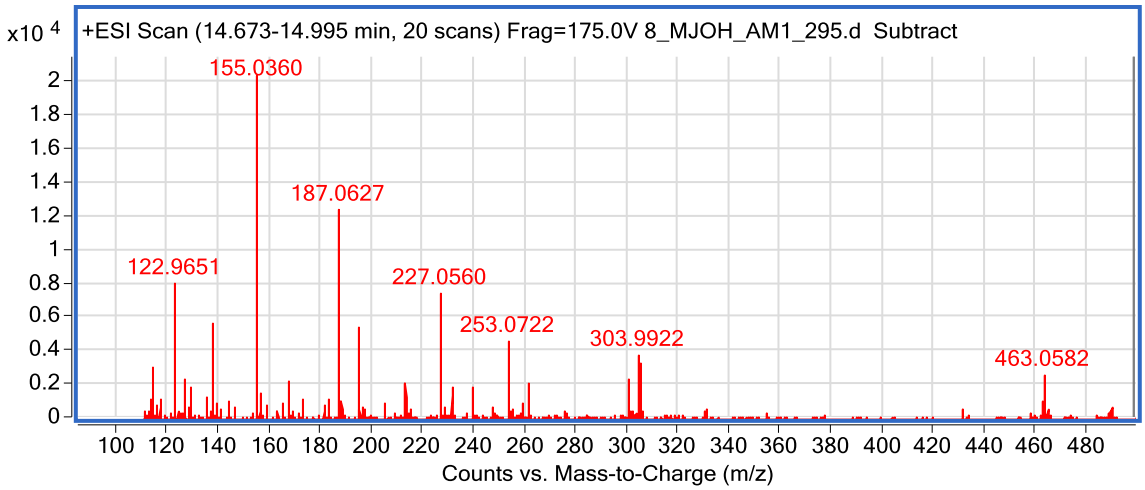

Figure A9.2. Peak A Mass Spectra

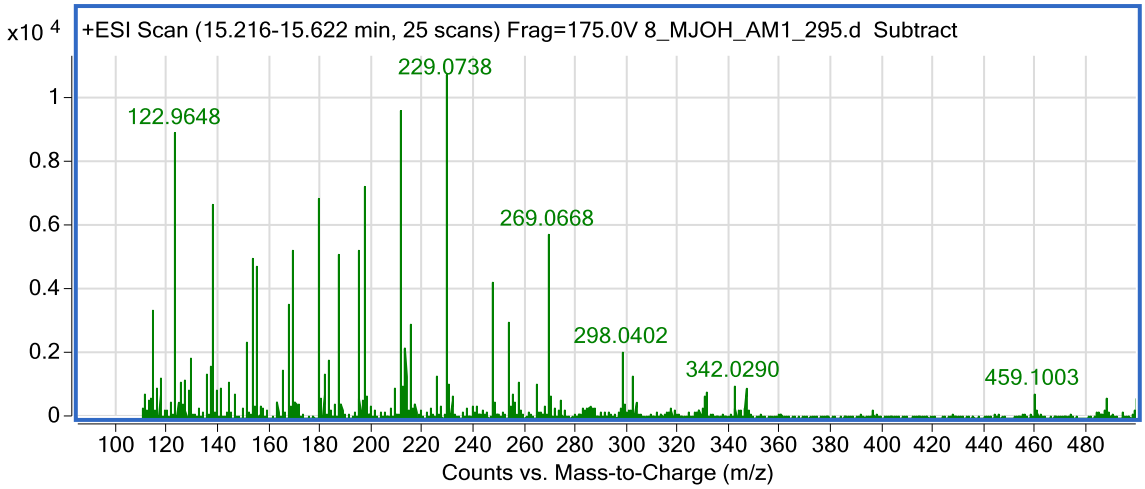

Figure A9.3. Peak B Mass Spectra

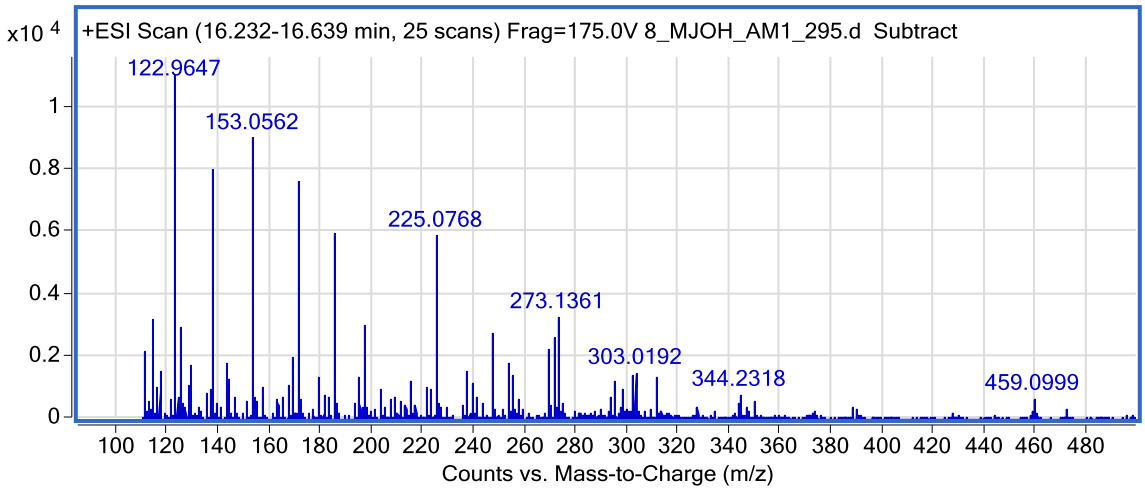

Figure A9.4. Peak C Mass Spectra

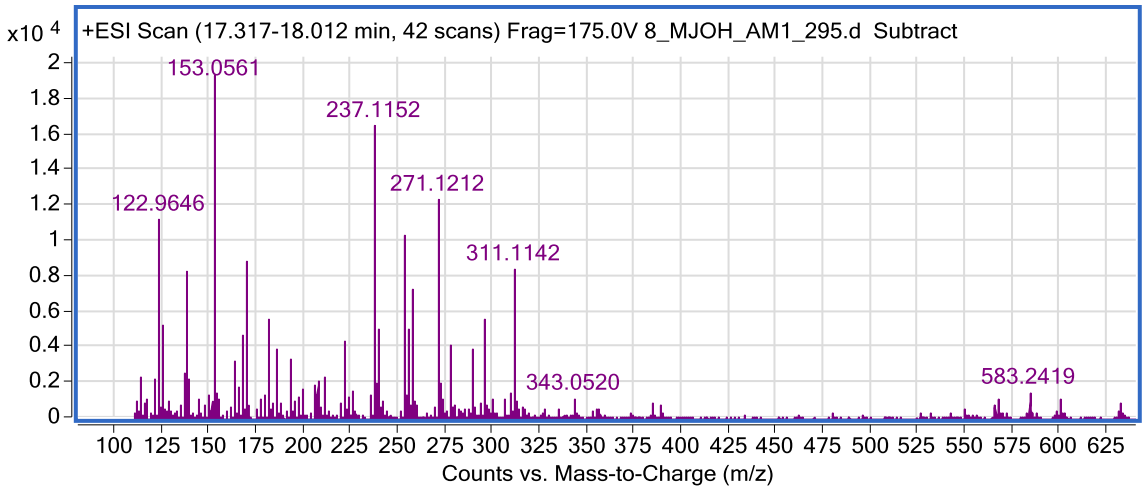

Figure A9.5. Peak D Mass Spectra

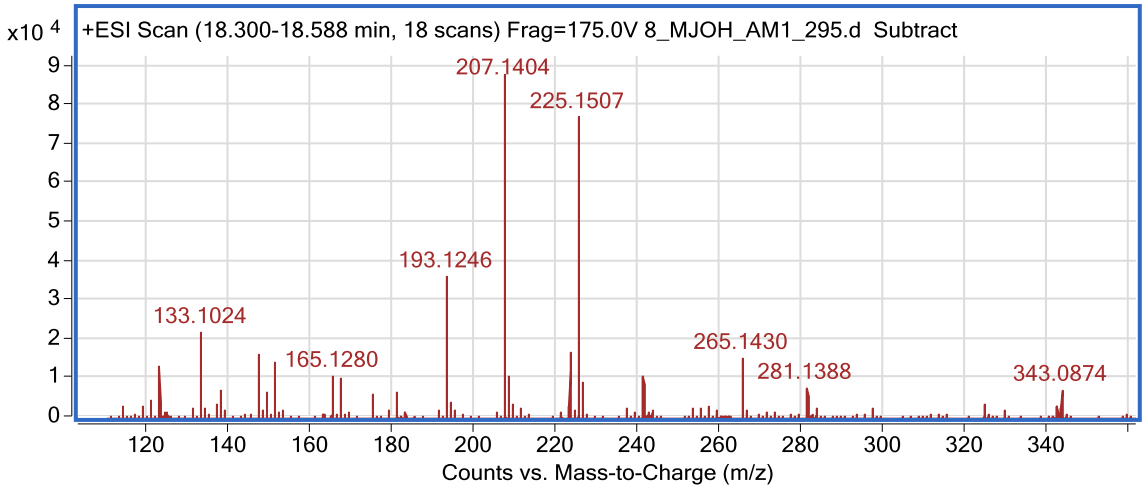

Figure A9.6. Peak E Mass Spectra

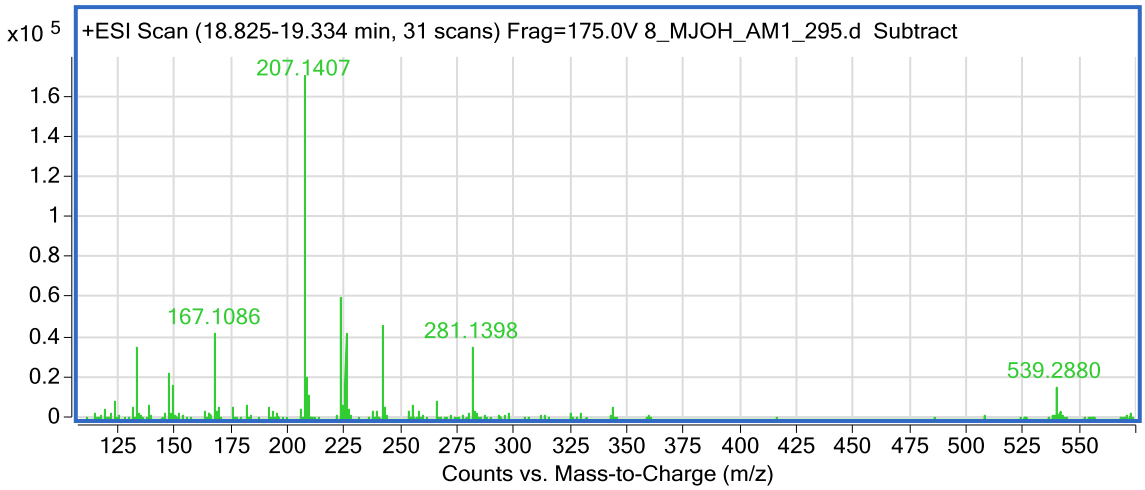

Figure A9.7. Peak F Mass Spectra

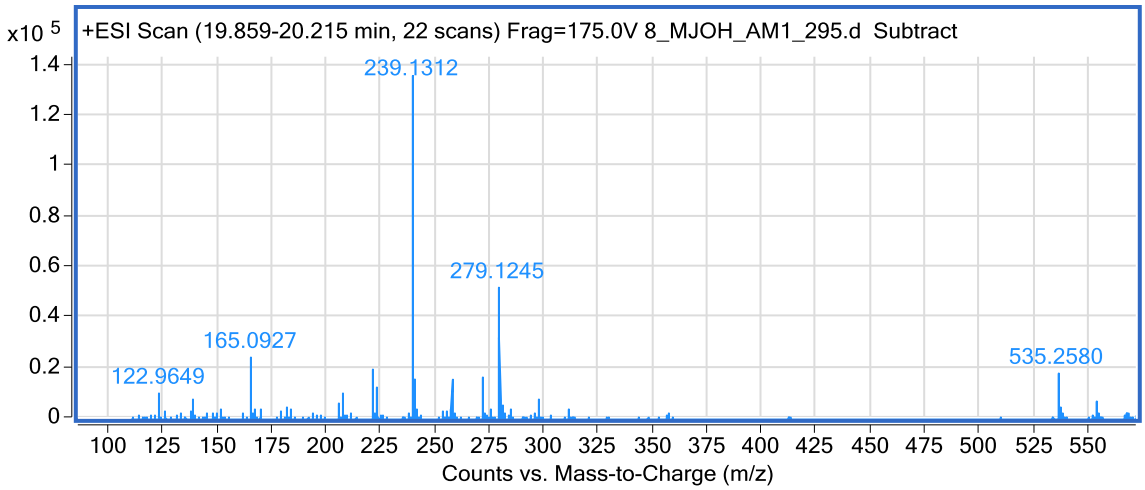

Figure A9.8. Peak G Mass Spectra

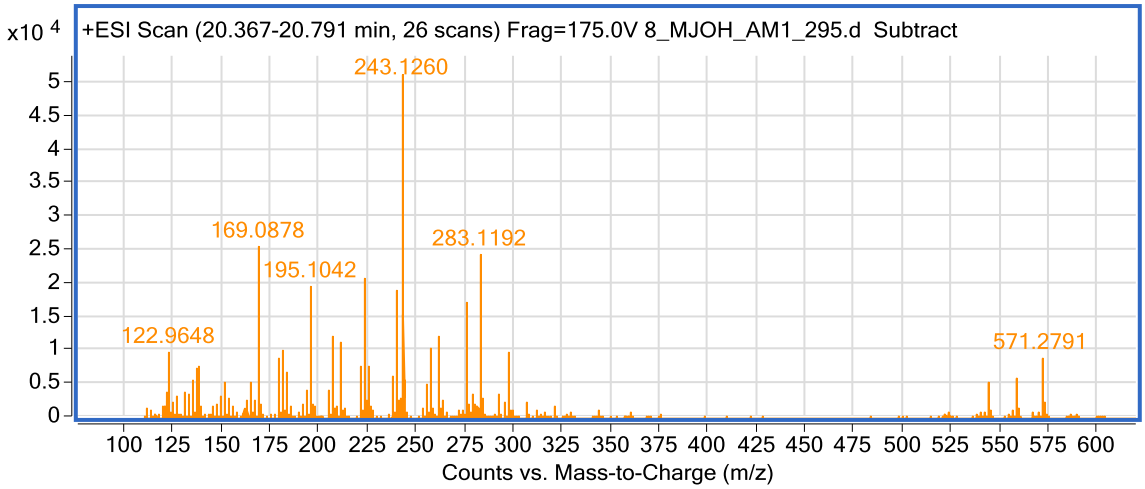

Figure A9.9. Peak H Mass Spectra

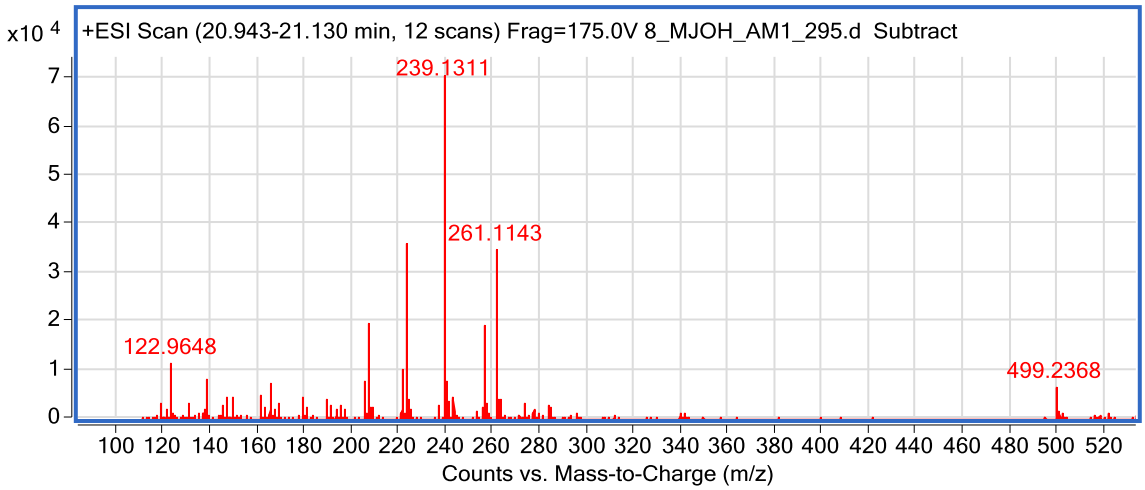

Figure A9.10. Peak I Mass Spectra

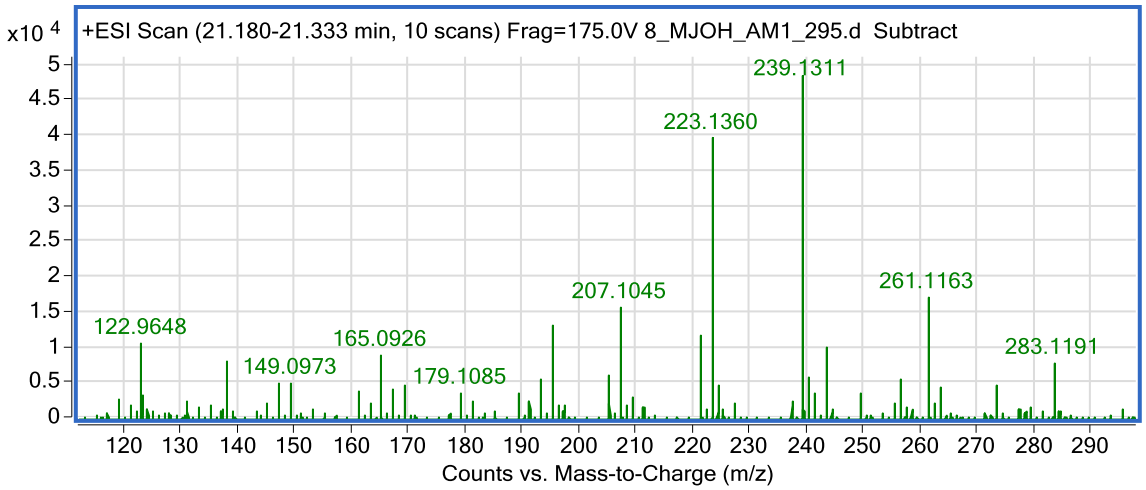

Figure A9.11. Peak J Mass Spectra

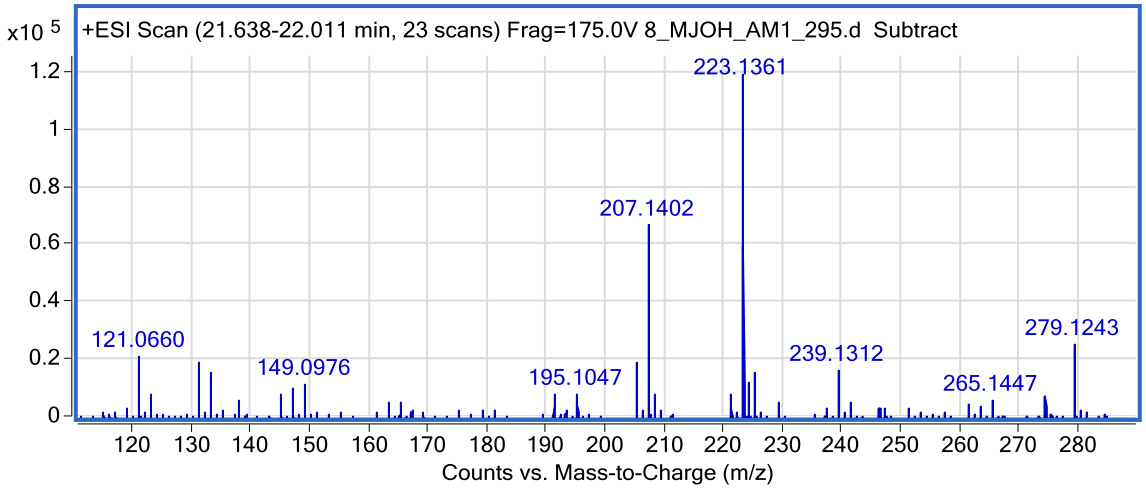

Figure A9.12. Peak K Mass Spectra

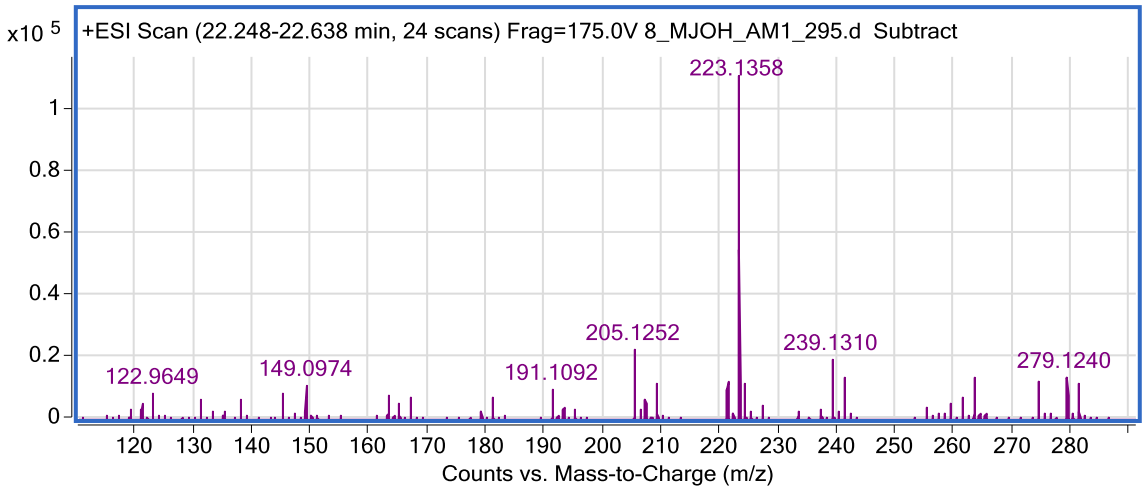

Figure A9.13. Peak L Mass Spectra

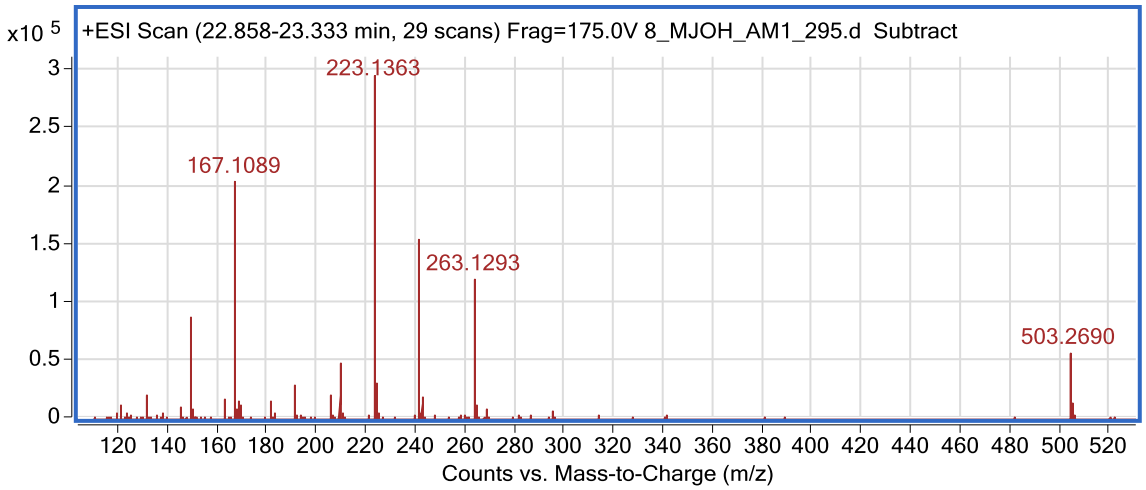

Figure A9.14. Peak M Mass Spectra

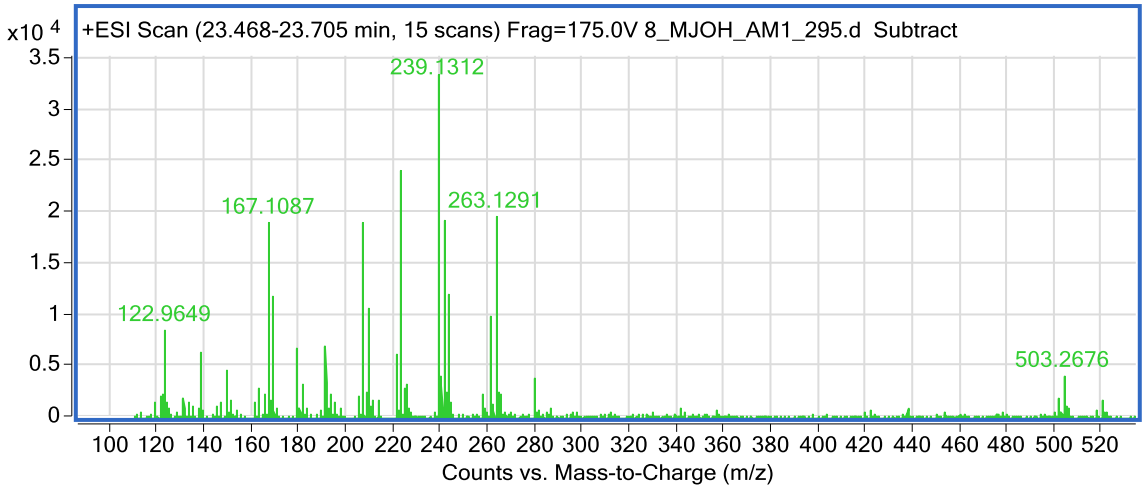

Figure A9.15. Peak N Mass Spectra

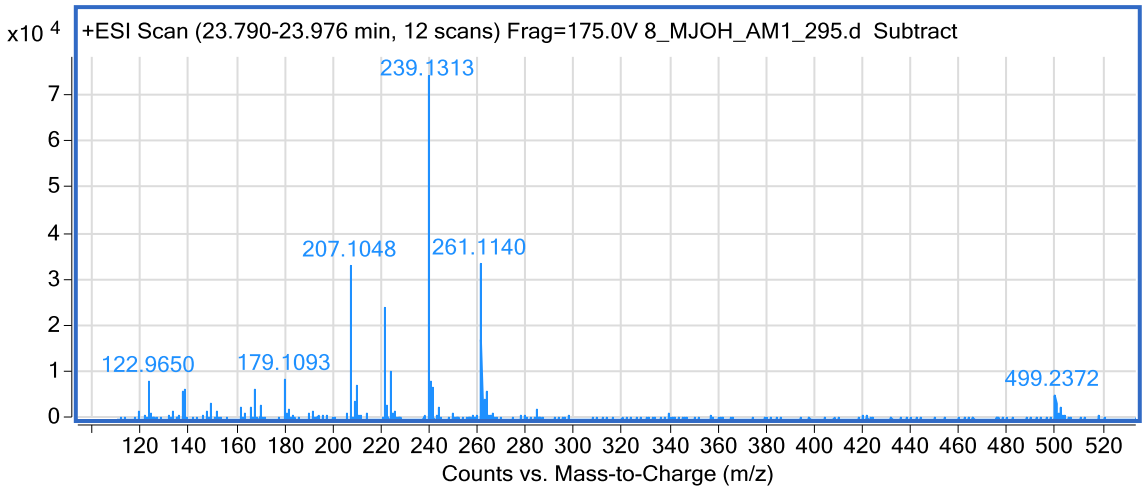

Figure A9.16. Peak O Mass Spectra

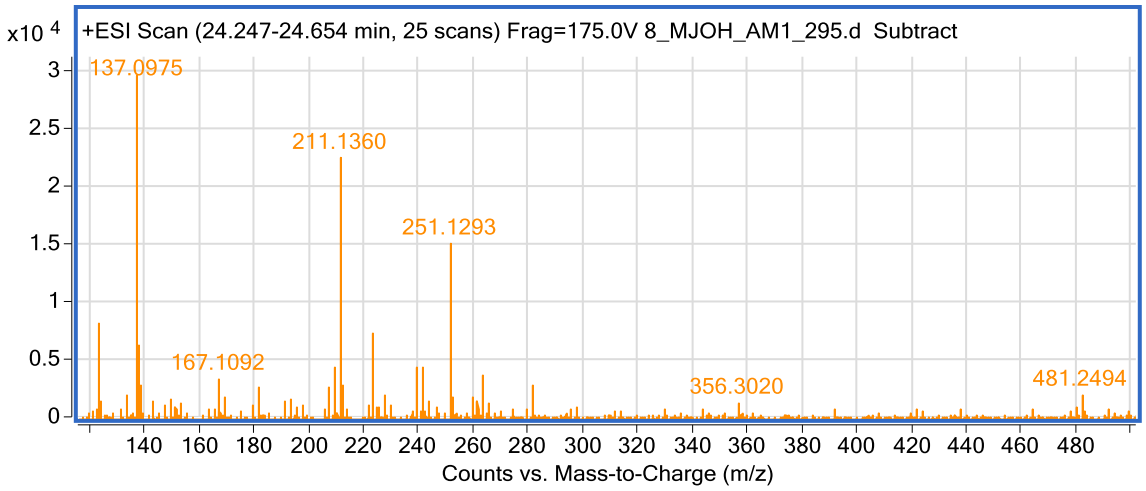

Figure A9.17. Peak P Mass Spectra

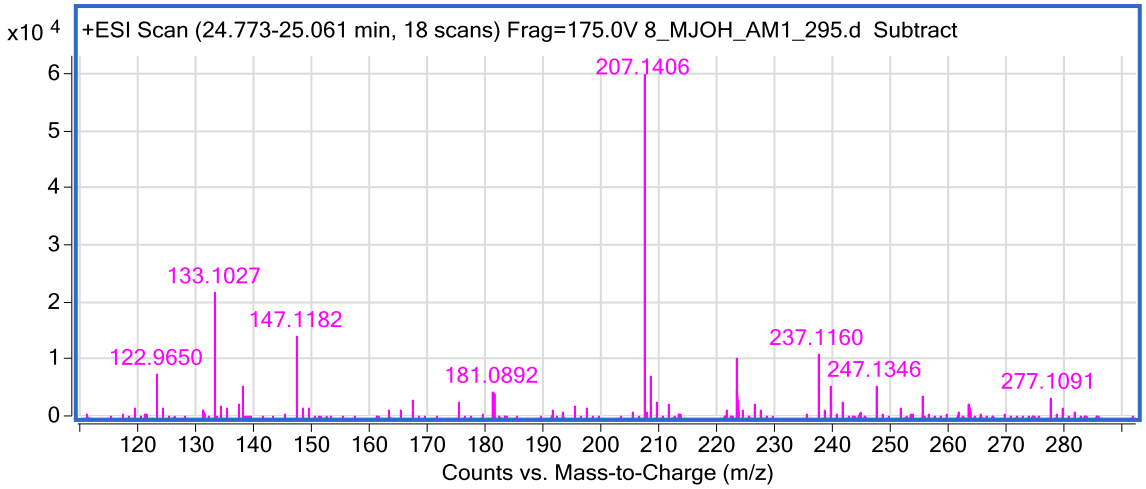

Figure A9.18. Peak Q Mass Spectra

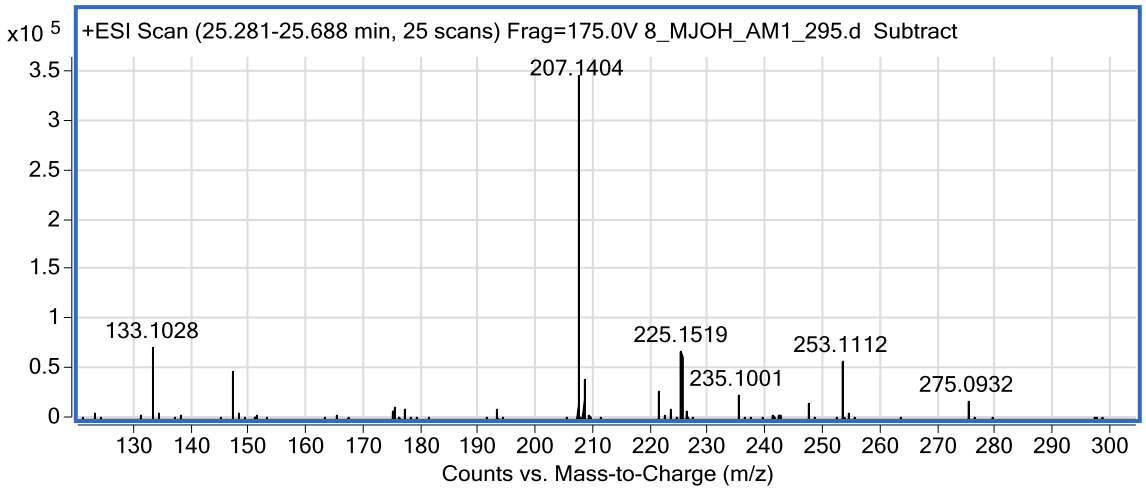

Figure A9.19. Peak R Mass Spectra

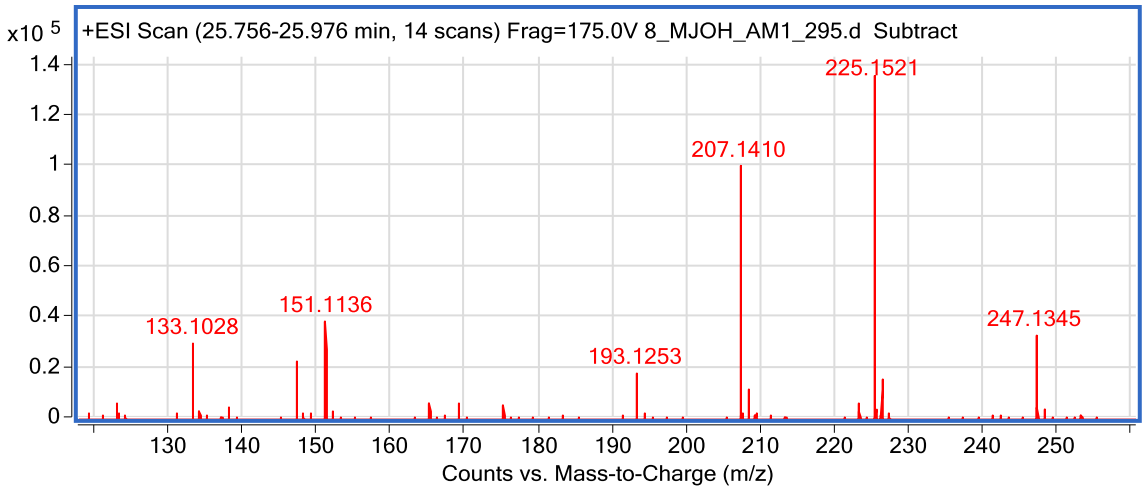

Figure A9.20. Peak S Mass Spectra

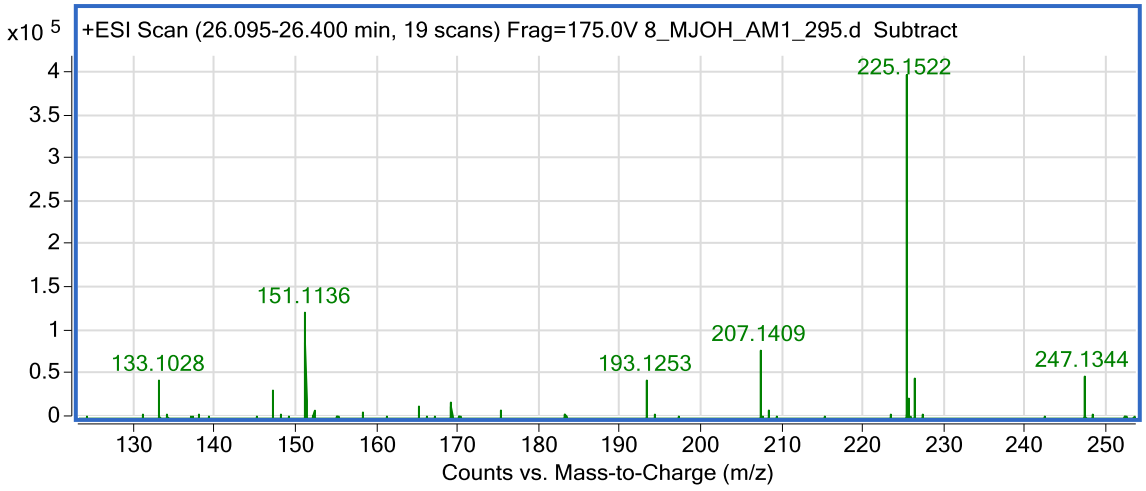

Figure A9.21. PeakT Mass Spectra

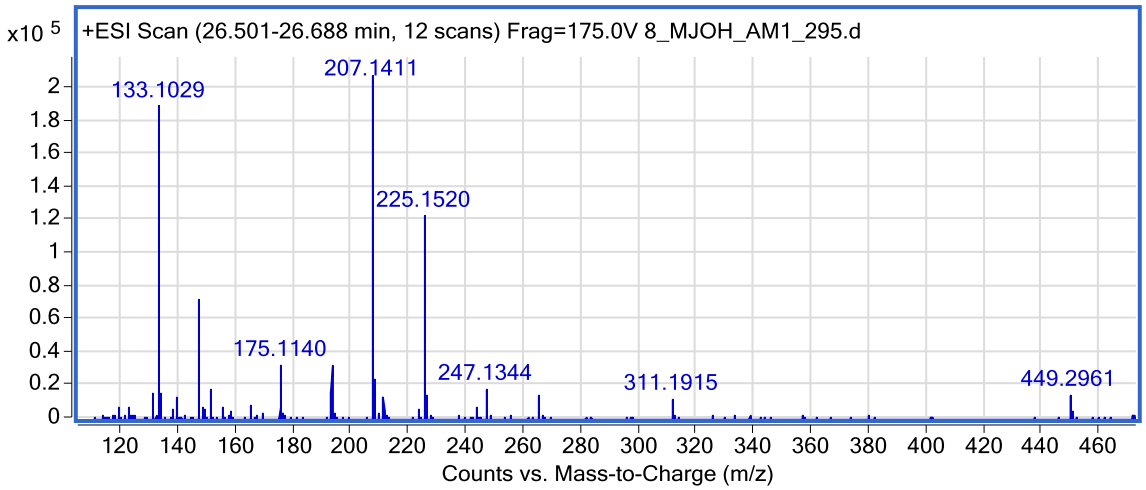

Figure A9.22. PeakU Mass Spectra

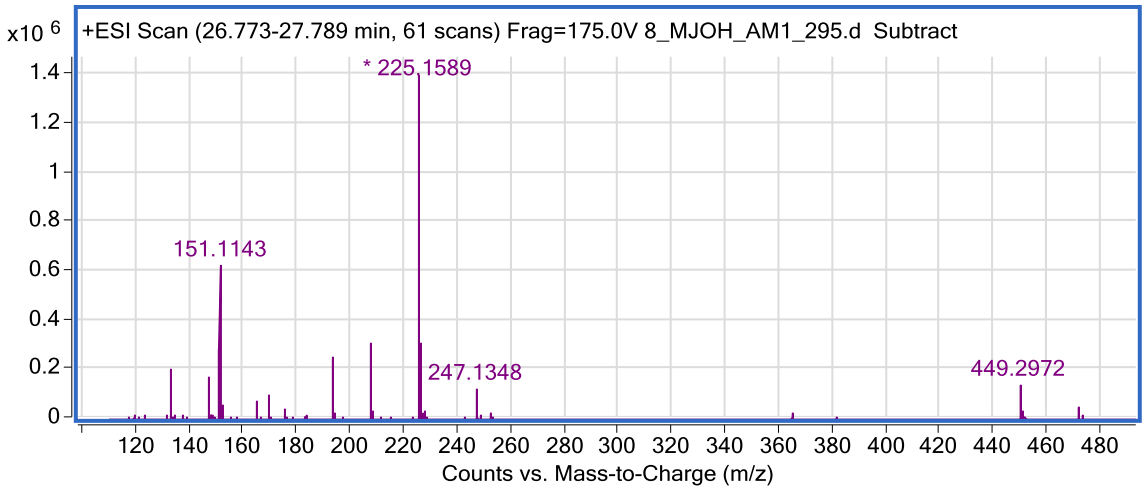

Figure A9.23. PeakV Mass Spectra

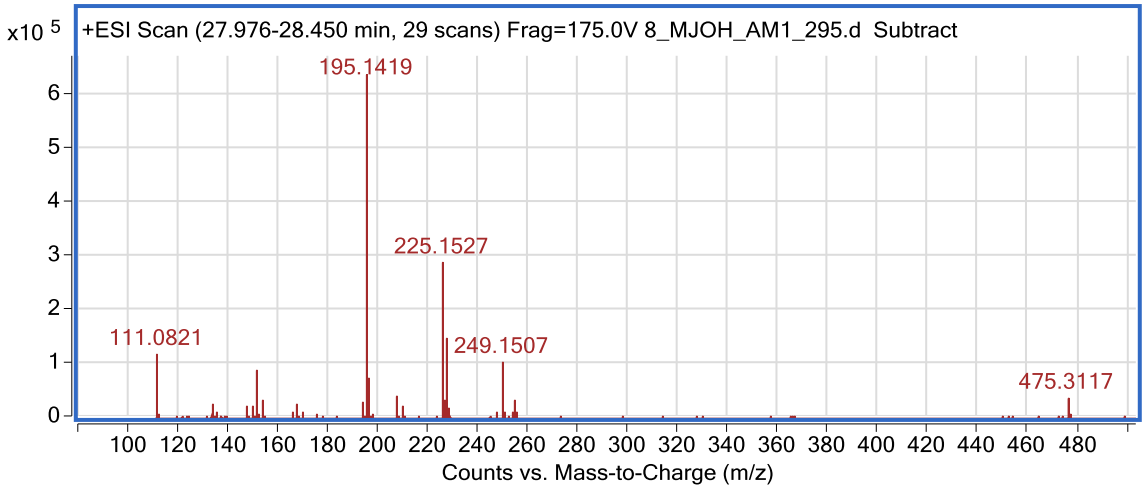

Figure A9.24. Peak X Mass Spectra

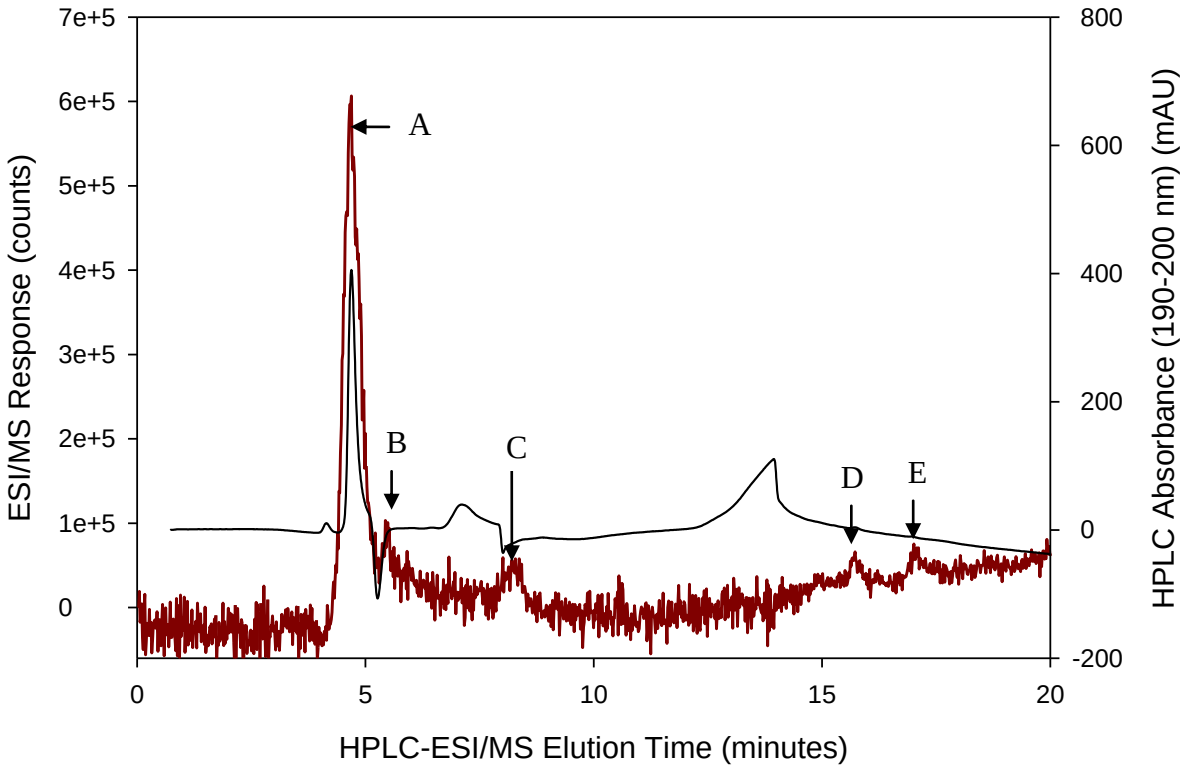

Figure A9.25. HPLC-ESI/MS TIC of 2mM MeJa with 2 mM H2O2 exposed to AM1.0 and 295 nm long pass filtered UV light for 8 hours with each peak labeled A-E

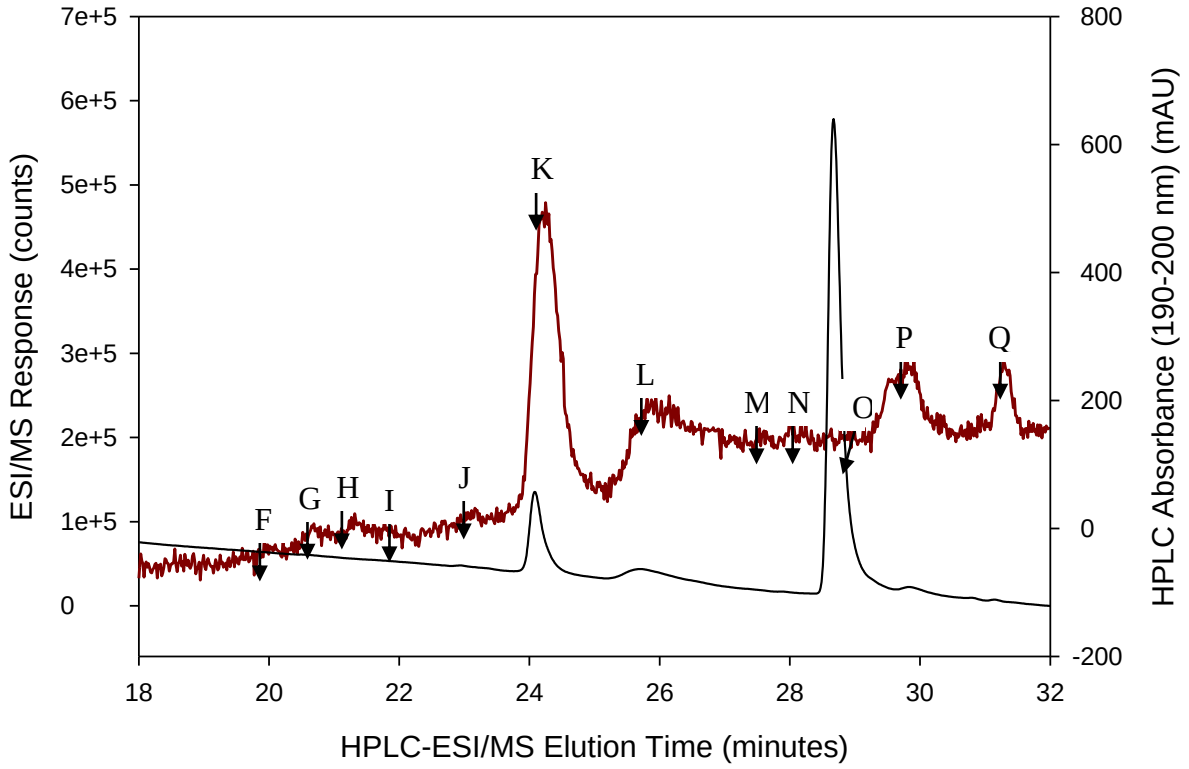

Figure A9.26. HPLC-ESI/MS TIC of 2mM MeJa with 2 mM H2O2 exposed to AM1.0 and 295 nm long pass filtered UV light for 8 hours with each peak labeled F-Q

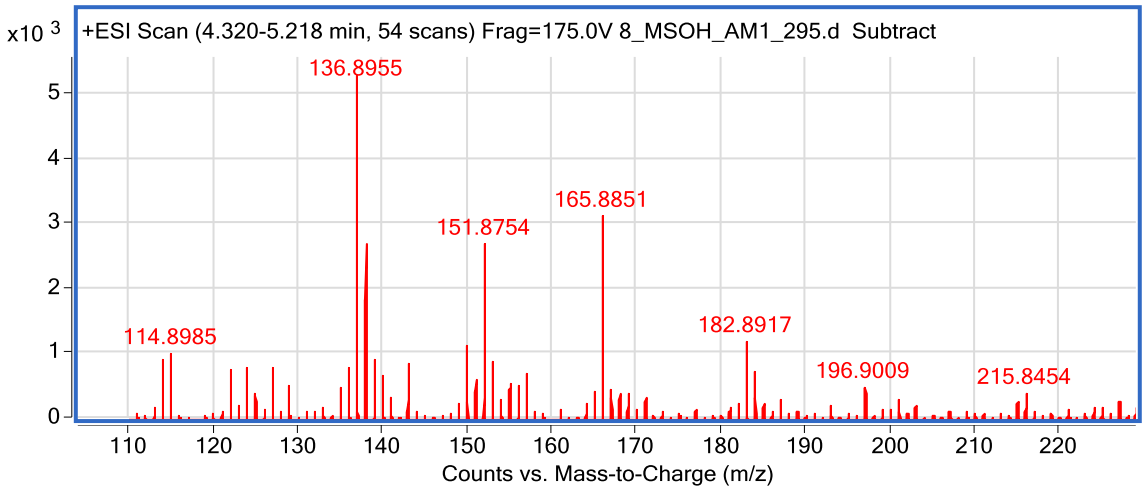

Figure A9.27. Peak A Mass Spectra

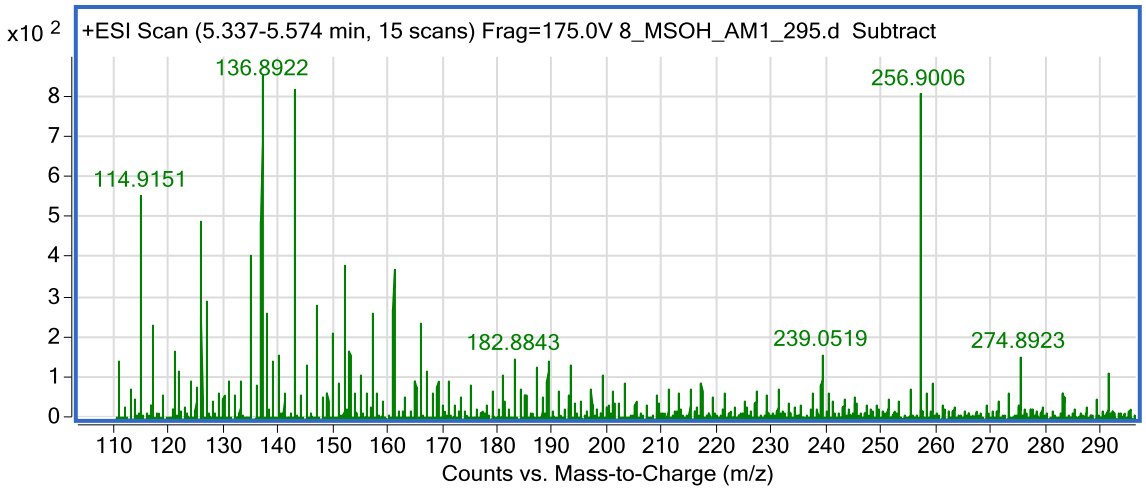

Figure A9.28. Peak B Mass Spectra

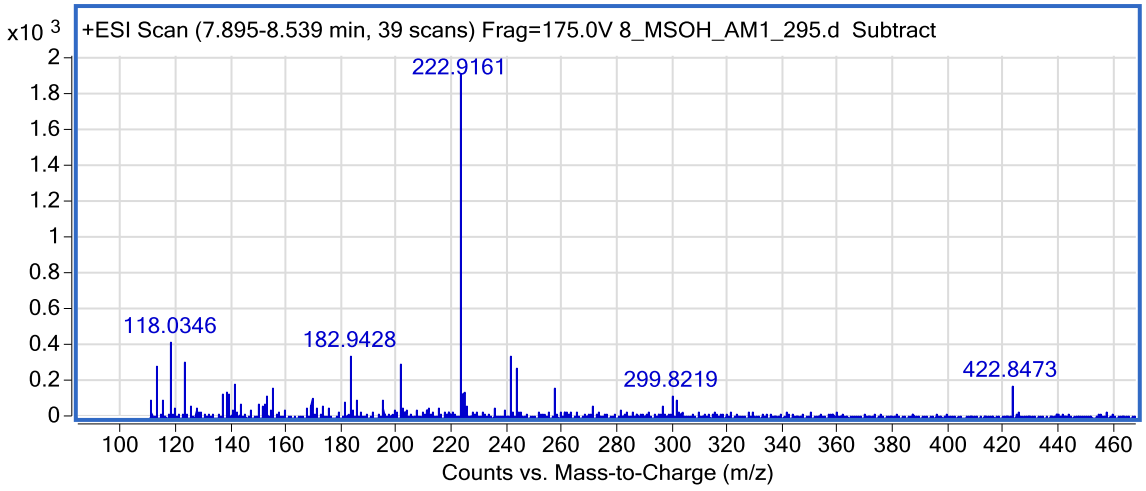

Figure A9.29. Peak C Mass Spectra

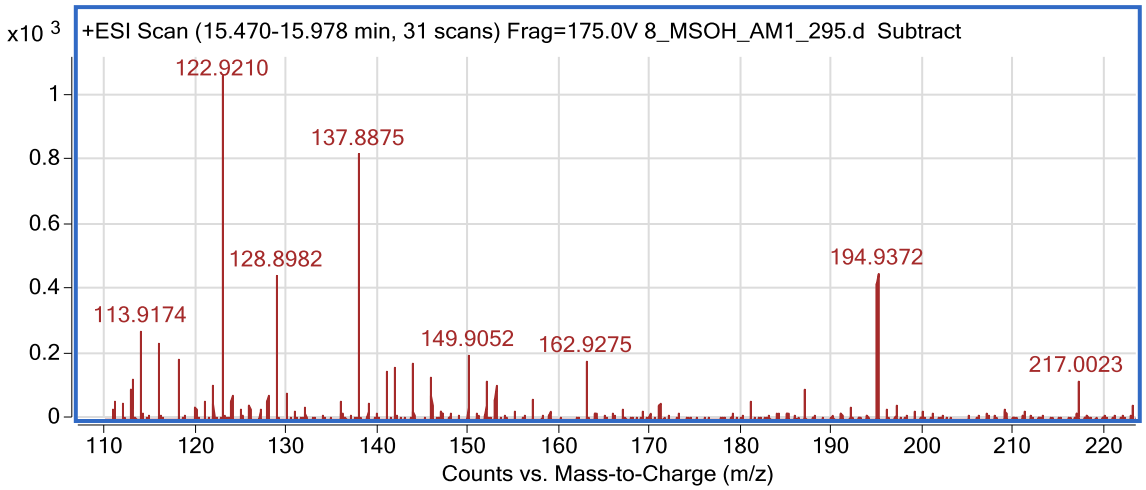

Figure A9.30. Peak D Mass Spectra

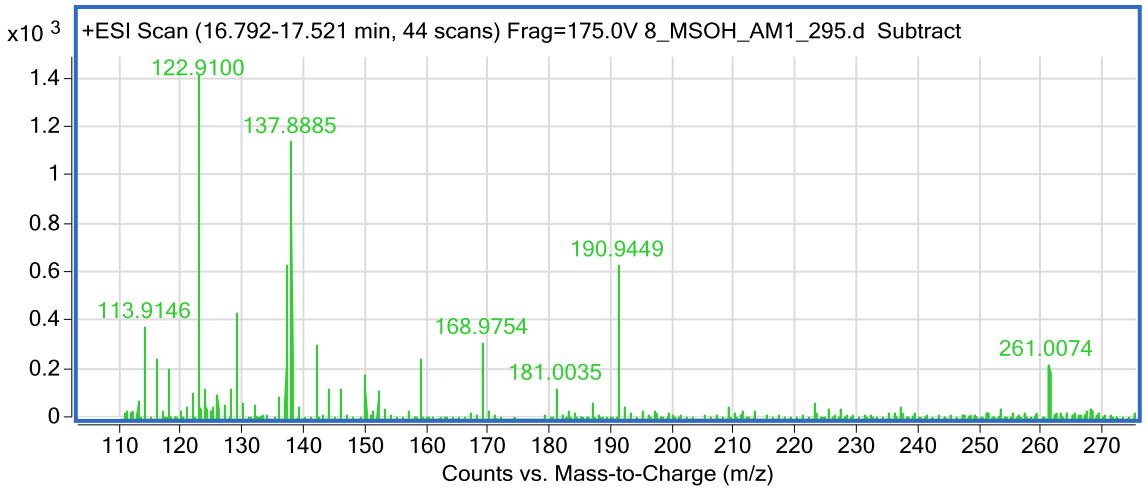

Figure A9.31. Peak E Mass Spectra

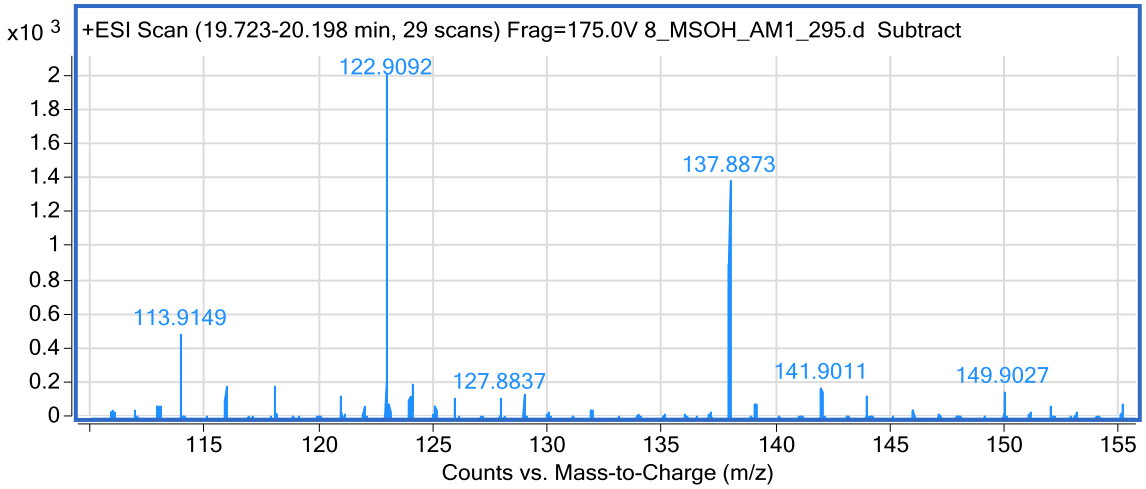

Figure A9.32. Peak F Mass Spectra

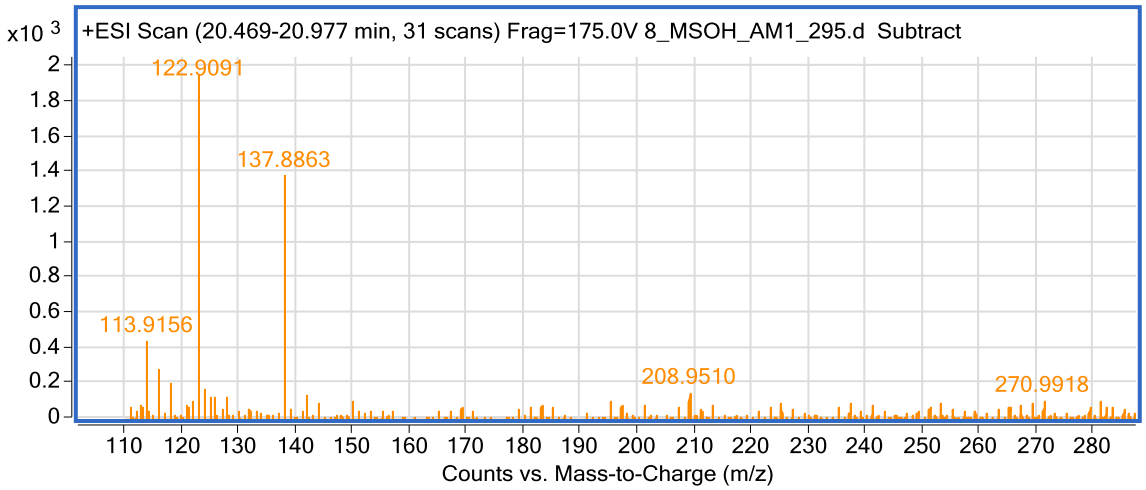

Figure A9.33. Peak G Mass Spectra

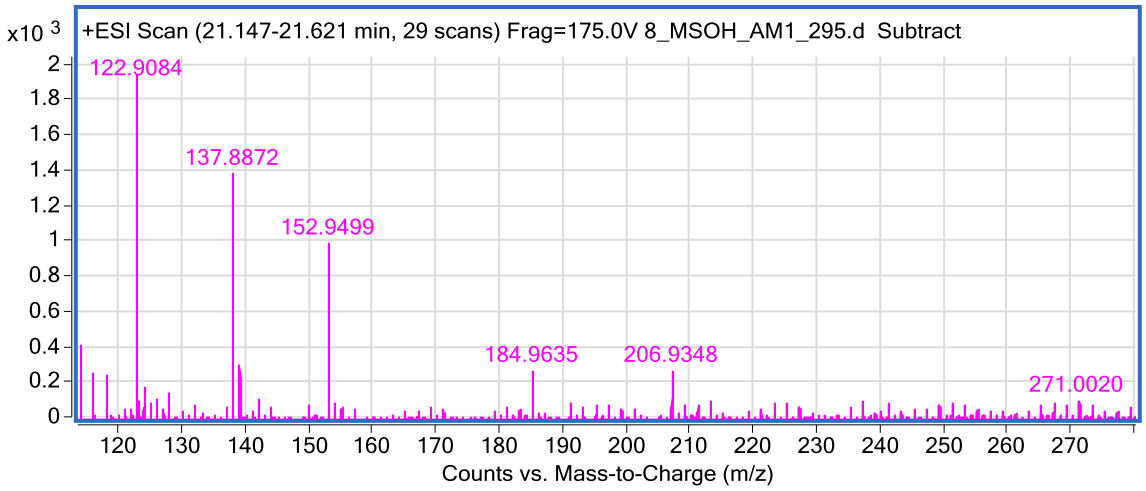

Figure A9.34. Peak H Mass Spectra

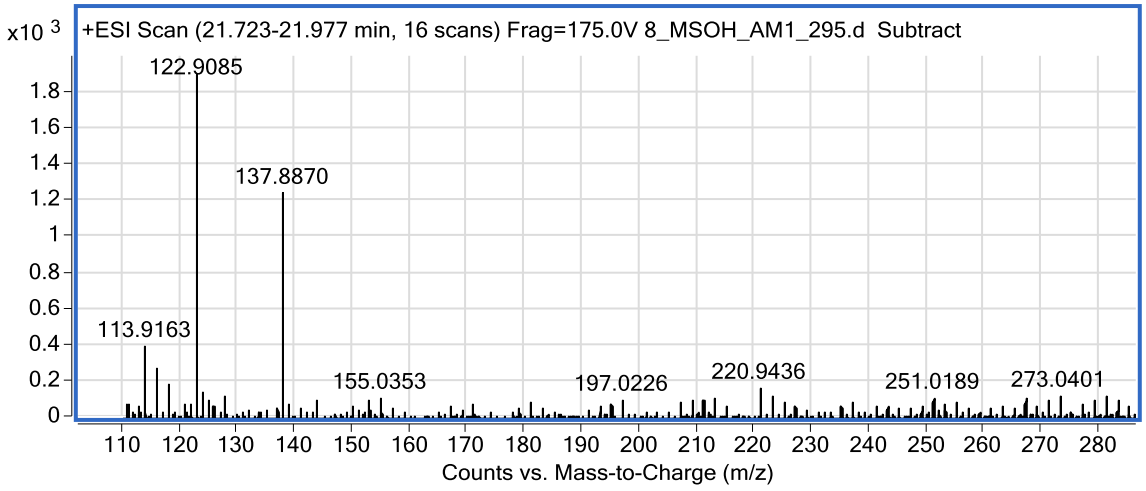

Figure A9.35. Peak I Mass Spectra

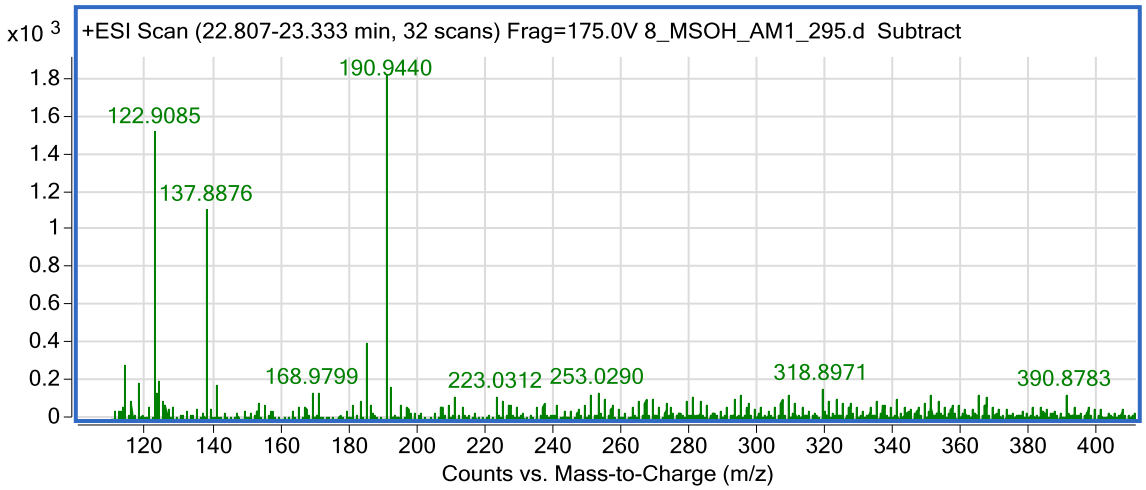

Figure A9.36. Peak J Mass Spectra

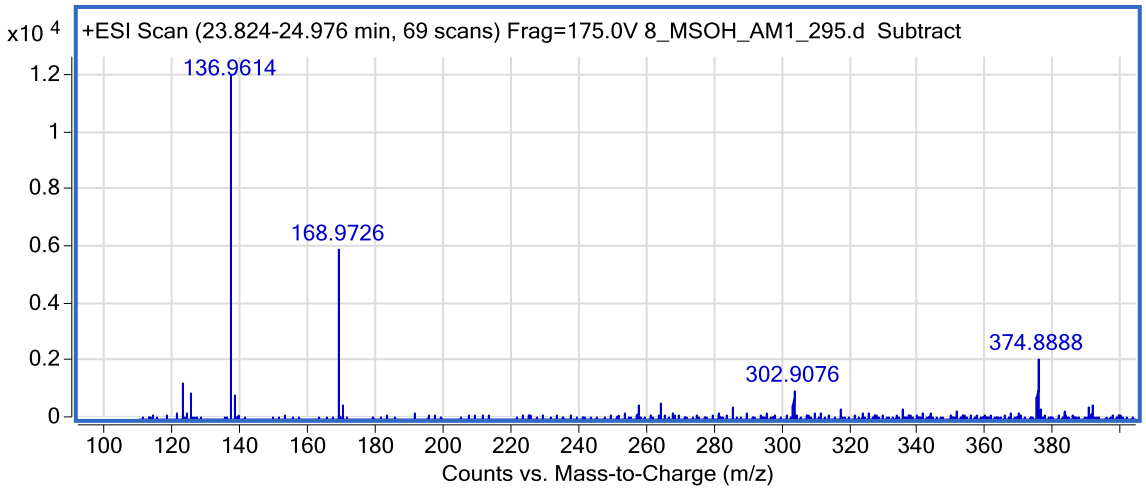

Figure A9.37. Peak K Mass Spectra

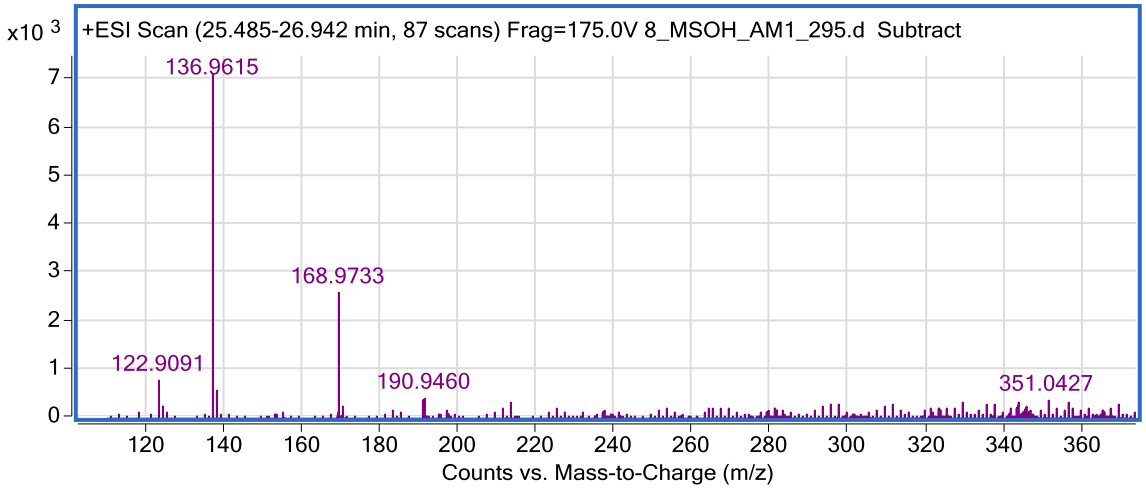

Figure A9.38. Peak L Mass Spectra

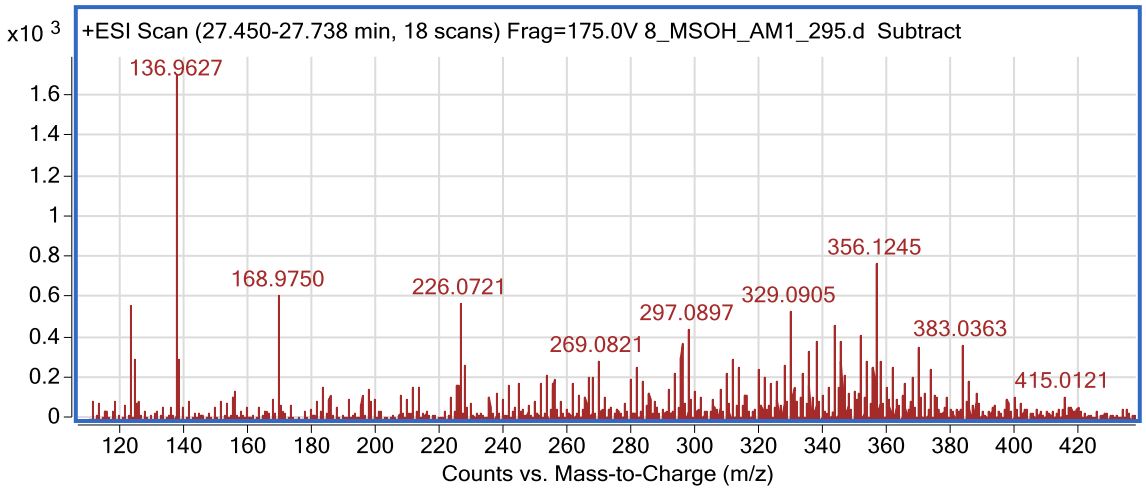

Figure A9.39. Peak MD Mass Spectra

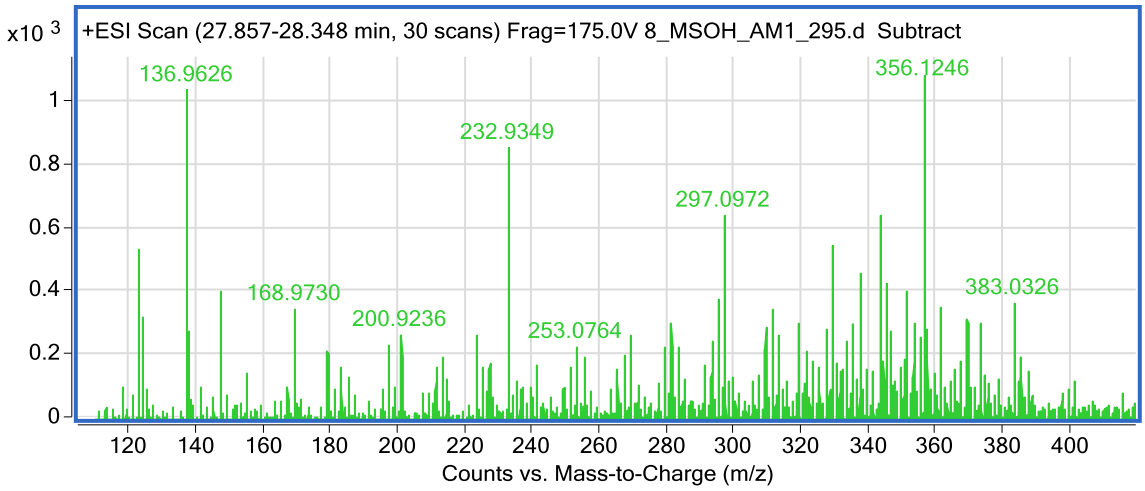

Figure A9.40. Peak N Mass Spectra

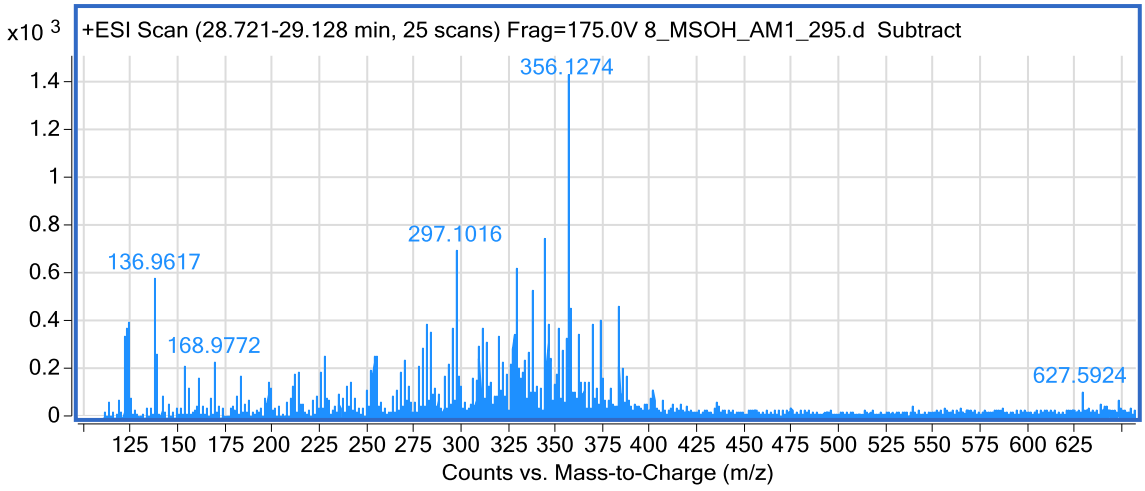

Figure A9.41. Peak O Mass Spectra

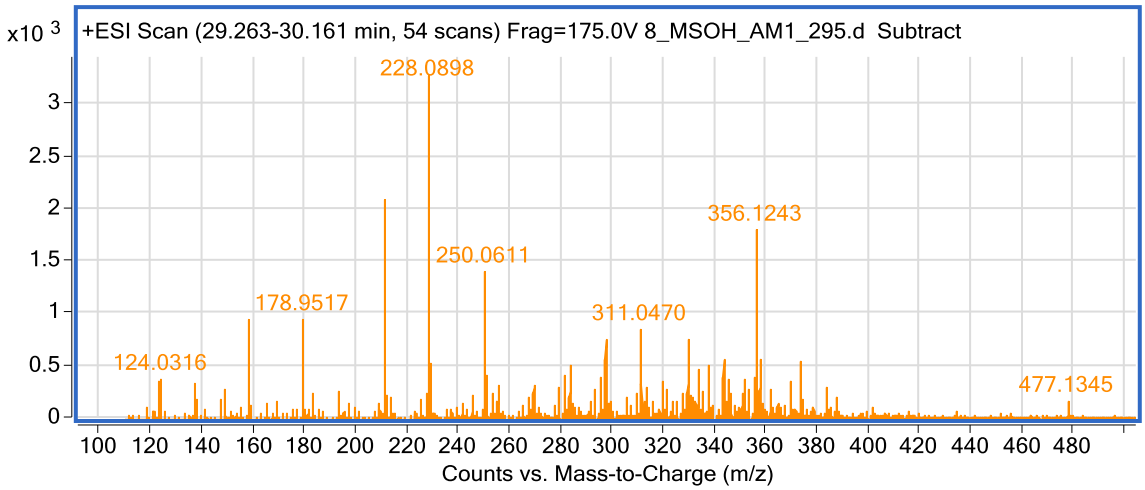

Figure A9.42. Peak P Mass Spectra

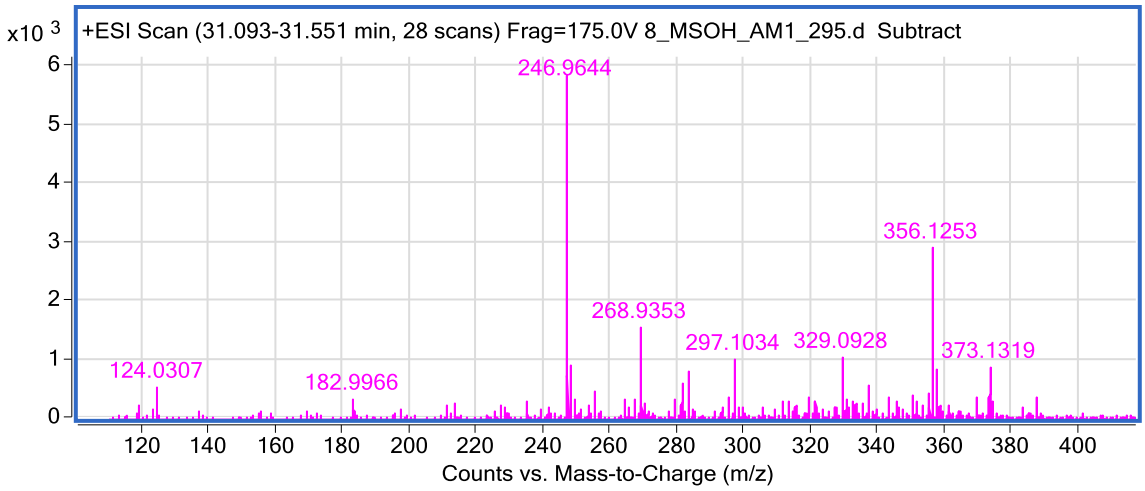

Figure A9.43. Peak Q Mass Spectra

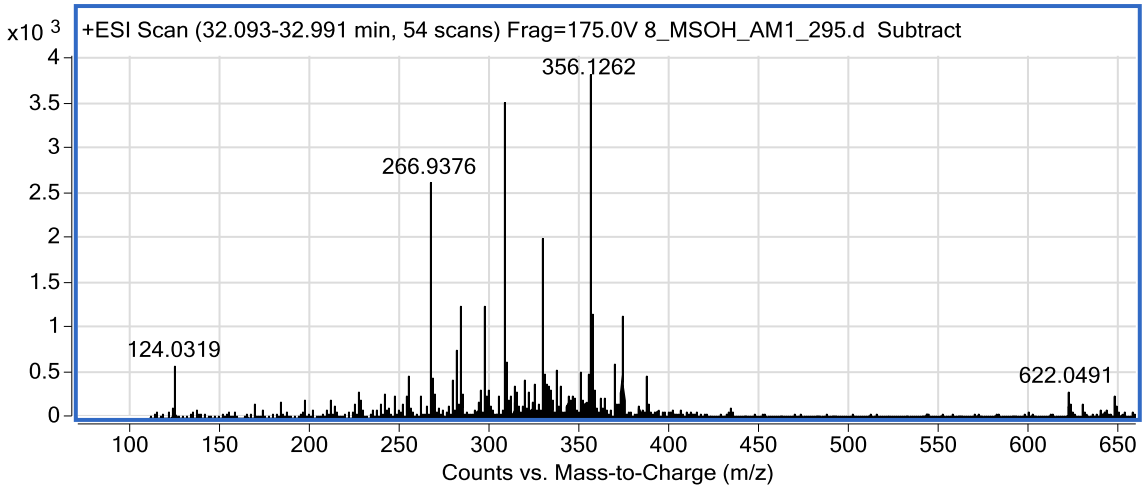

Figure A9.44. Peak R Mass Spectra

VITA

Amie Hansel was born and raised in New Orleans, Louisiana. She then moved with her family to Slidell, Louisiana where she attended Northshore High School and graduated in 2003. She then attended Louisiana State University to attain a Bachelor of Science in Biology in 2007. After deciding upon a career path change in 2009, she began taking undergraduate courses in the Louisiana State University Cain Department of Chemical Engineering. By August 2011 she was enrolled in the graduate program, and upon completion, she plans to begin a career as a Process Engineer in industry.